Analysis

Larch Round Wood
and its Applications

Appendices

Graduation project
Rogier Schuch
May 2006

Technische Universiteit Delft

Faculty of Civil Engineering and Geosciences

Larch Round Wood

and its Applications

Analysis

Author

Rogier Schuch
Giststraat 12
2611 PT
Delft
015-2137526
06-42105841
rogier@giststraat12.com

Graduation committee

Prof.ir. F.S.K. Bijlaard
section Structural and Building Engineering
faculty Civil engineering and Geosciences
TU Delft

Dr.ir. J-W.G. van de Kuilen
section Structural and Building Engineering
faculty Civil engineering and Geosciences
TU Delft

ir. P.A. de Vries
section Structural and Building Engineering
faculty Civil engineering and Geosciences
TU Delft

ing. Z. van Olst MBA
"Staatsbosbeheer" Services

Dr.ir. P.C.J. Hoogenboom
section Structural Mechanics
faculty Civil engineering and Geosciences
TU Delft

Preface

This report is written for the master graduation thesis on the faculty of Civil Engineering and Geosciences on the Technical University of Delft. The title of the thesis is "Larch Round Wood and its Applications". The report consists of two parts:

In the part "Analysis" the main topics for this project are discussed and explained.

In the part "Appendices" the background information and generated data is presented. A compact disc is added to this part with the excel sheets that are used for the project.

The author would like to thank all who have aided in writing this report and in assisting with the experiments.

Rogier Schuch, May 2006

Summary

In this project, a quality investigation is done on the influence of different parameters on the growth of homegrown Japanese larch. These parameters are expressed in a Site index, which is determined for some specimen that are analysed for density and strength characteristics (Chapter 2). An attempt is made to find a relation between this Site index and the strength of the specimen.
The result of this analysis is projected on a viewing platform that was designed for the CONIFERS project. This platform is analysed in a model for different situations that might occur, based on low stiffness values of one or more elements (Chapter 3).
Finally, the block shear joint that was used and designed for this viewing platform is tested for moment capacity (Chapter 4). The desrcibed connection system for round wood is patented. A copy is given in Appendix 9.

All appendices are shown in the part "Appendices" of this report. In this part "Analysis", only the "List Of Terms" and "Literature" are given.

Table Of Contents

1 Introduction

Small diameter round wood is no longer widely used in constructions in Europe. There are a number of reasons for this. The first is because round wood is not available in large numbers via the normal commercial routes. Secondly the strength of the material is not known with architects and engineers. Also the methods of connecting the material are, because of its roundness, not known with architects and carpenters. And finally there is a lack of standards and models. To do something about this situation a project was started in Finland, Austria, France, England and The Netherlands (project FAIR CT 95-0091 or project CONIFERS[1]) to investigate the use of small diameter larch round wood in constructions. This resulted in information about availability, dimensions and strength of round wood from thinning and potential constructions that can be made with round wood and its connections.

Figure 1.1 viewing platforms

In The Netherlands the project focused on the strength of Japanese larch round wood. The choice for Japanese larch was made because of the good mechanical properties and high durability of larch in general and the relative large amount of Japanese larch in The Netherlands specifically. For this, 180 trees from a small area in the "Veluwe" have been tested and analysed. The results from this project were quite surprising: it was found that larch round wood can be assigned to strength class C40, as set by EN 338 for sawn timber. Furthermore a new method of connecting round wood to other constructions or to itself has been developed. This connection method is easier to make than conventional methods of connecting and has the possibility to easily disconnect the round wood poles again when they need to be replaced. The Dutch governmental forestry maintenance organisation, "Staatsbosbeheer", had the wish to increase the use of round wood in constructions and therefore a new viewing platform with a height of 14m has been designed with the new information (figure 1.1, top). The platform is situated in Grollo in the province "Drenthe". This platform has the form of a cooling tower and thus consists of purely straight lines. This is fundamentally different to a similar, but more conventional viewing platform (figure 1.1, bottom) in a way that now only normal forces occur in the structure. Because of this, the developed method of connecting the round wood poles is only tested for normal forces.

This final project will deal with the use of homegrown round wood. The goal is to promote its use by determining the strength of round wood at different locations in The Netherlands, and to analyse the viewing platform and connection design with the new information obtained in this project. With this complete description of the use of homegrown larch round wood from mechanical properties to design and detailing of a viewing platform, this project could serve as an example of its possibilities for structural engineers, architects and carpenters.

This report will deal with three major questions:

- Are the results from the CONIFERS project concerning strength of larch round wood representative for all the larch forests in The Netherlands? (Chapter 2)
- What are the consequences of the timber strength variations for the round wood viewing platform? (Chapter 3)
- What is the moment capacity of the round wood connection developed for this viewing platform? (Chapter 4)

For this project, some Dutch studies have been used that use many dutch forestry terms. Some of these could not be translated and will be explained in the List Of Terms in the Appendix.

[1] **CONIFERS**: **CON**structive **I**deas **F**or **E**uropean **R**oundwood in **S**tructures

2 Quality investigation

For the CONIFERS project, 180 Japanese larch trees from " 's Herenberg" in the eastern part of The Netherlands were tested to determine the mechanical properties of small diameter larch round wood. The results from this test were quite surprising: the combination of density, bending strength and stiffness resulted in a classification in strength class C40 as set by EN384. Because at that time classes higher than C40 did not exist in the codes, this is even conservative. Now, these trees would be assigned to class C40/C45. This is much higher than the commonly assumed strength class C24 for Dutch construction wood. It must be noted, that these classes are determined for sawn construction timber. Strength classes for round wood are not available yet.

Table 2.1 result strenght tests [De Vries]

diameter [mm]	100	120	140	tapered	all
density$_{clearwood}$ [kg/m^3]	578	582	585	574	580
5% (normal)	497	520	519	496	509
MOE$_{local}$ [N/mm^2]					
mean	13,5	14,2	14,7	14,7	14,3
5% (ranked)	10,1	11,2	10,4	10,8	10,9
MOR$_{bending}$ [N/mm^2]					
5% (ranked)	62	63	63	71	63
MOR$_{compression}$ [N/mm^2]					
5% (ranked)					38
strength class	C40	C40	C40	C40	C40

Because of the small growth area of the tested trees, an investigation is necessary to determine whether this result can be used for all the small diameter larch round wood in The Netherlands. This is done by an analysis of the relation between strength of the wood and the soil it grows on and other aspects that influence the growth of larch. After this analysis, these aspects for the specimen from the CONIFERS project can be related to the average values for The Netherlands. The variation of these aspects with the average values determines the applicability of the test result from the CONIFERS project for homegrown larch round wood.

The investigation is based on a study on the "Instituut voor Bos- en Natuuronderzoek" or IBN [Van den Burg, 1997]. In this study a relation between growth height and growth area of Japanese larch is determined. The results from this study will be presented first, after this the further analysis will be discussed. More information about this study and more is presented in Appendix A2.

The study on the IBN is done for foresters, not for structural engineers, and the description for "wood quality" is different for both fields. For structural engineers, wood quality is based on strength. For foresters, wood quality is based on produced volume. For foresters wood has a high quality at fast growth rate, whereas for structural engineers a fast growth rate usually implies larger growth rings, lower density and lower strength values. Still, this study is used as a first indication for the relation between growth area and strength of Japanese larch in The Netherlands, although this study only gives results about growth volume, not strength.

After an analysis on the results from this study, an attempt is made to find a relation between the growth height and strength with the results from strength tests. This is explained in chapter 2.3: Experiment.

2.1 Growth and growth area of Japanese Larch

In The Netherlands there is 18020 ha of Japanese larch, which is about 5,6% of the total forest area. Japanese larch is primarily found in the North-Eastern forest area [Anonymous, 1984]. Figure 2.1 shows the locations of the different forest areas in the North-Eastern part of the Netherlands. Table 2.2 shows the distribution of Japanese larch on these forest areas.

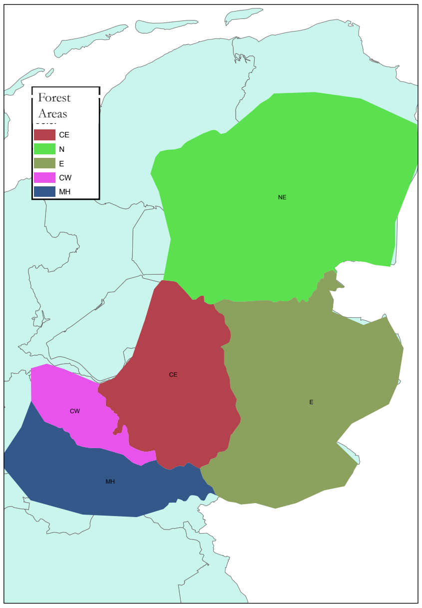

Figure 2.1 forest areas East Netherlands

Table 2.2 area (ha) of Japanese larch per forest area

forest area	ha
NE	6079
E	3426
CE	3877
CW	1390
rest	3249
total	18020

To be able to make any prediction, first a parameter needs to be found that best describes the growth height. It is most logical to use the average tree height per area, but this parameter is not suitable, because it is dependent on the treatment (thinning) of the plot. Two parameters that are independent on these aspects are the dominant height and the "opperhoogte" [Anonymous, 1996].
The dominant height of a plot is defined as the average height of the thickest tree per are.
The "opperhoogte" is the average height of the highest tree per are.
The difference between these two parameters per plot is small (some decimetres) and irrelevant for this study, in which the smallest difference in height is 1 decimetre. For this study the parameter "opperhoogte" (h_{top}) is used.
To make the parameter h_{top} independent of the age of a tree, it is converted to the Site-index or S-value. This is defined as the height of a tree with an infinite age

From previous studies in the '50's some conclusions can be made about growth of larch:

- Japanese larch is sensitive for low groundwater level. Dry grounds are not suitable.
- Japanese larch is sensitive for phosphor. A high phosphor level stimulates growth.
- Although differences in temperature between its country of origin, Japan, and The Netherlands are big, this does not seem to disturb growth on grounds with a good groundwater level.

Besides these aspects many other aspect have been investigated, such as humidity, wind, vegetation etc. These extra aspects turned out not to be of great influence on the growth of Japanese larch and will therefore not be discussed in this report.

To determine the influence of these aspects on the growth the following parameters were introduced:

• For the groundwater level a factor V_{gb} is used. This is a combination of a factor VL_{gr} for the water content of a soil type and the rainfall deficiency per forest area. The rainfall deficiency is determined as the rainfall in mm in a forest area, compared to the rainfall in mm per year in the reference forest area. The description of the forest areas is given in Appendix A2. The factor VL_{gr} is divided in 5 classes of 50 mm and is dependent of the soil type (table 2.4 and 2.5). The correction for rainfall deficiency is expressed in the class of VL_{gr}. So a rainfall deficiency of 30 mm is expressed in a substraction by 30/50 = 0,6 VL_{gr}. Generally, the factor V_{gb} can be calculated by:

$$V_{gb} = \mathrm{Class}_{VL_{gr}} + \frac{\mathrm{deficiency}}{50}$$

• For the phosphor content a factor P_{to} is determined per soil type. Also a factor N_{org} is determined to include the influence of the nitrogen content on the growth. These factors are shown in table 2.4.

Table 2.3 rainfall deficient per forest area

forest area	rainfall [mm/year]	rainfall deficiency [mm/year]
CW,L,MN,PL,PE,PS,R,SE,SW (reference)	230	0
CE	200	30
NE,E	170	60
MH,MS,PW	255	-25

Table 2.4 soil content

soil type	Code	VLgr	Norg	Pto
enkeerd	bEZ	2,2	2,4	23
kamppodzol	cHd	2,8	1,73	25
laarpodzol	cHn	3	*	15
akkereerd	cZd	2	2,32	32
haarpodzol	Hd	3,7	1,88	15
veldpodzol	Hn	3,2	1,97	14
moerpodzol	i,v,zWp	2	1,86	11
bruine beekeerd	pZg	2	*	*
gooreerd	pZn	2,1	2	22
holtpodzol	Y	3,3	2,23	25
duinvaag	Zd	2,5	2,24	15
zwarte enkeerd	zEZ	2	2,31	27
meerveen	zV	2,3	2,04	18

Table 2.5 watercontent classes

class	VLgr (mm)
5	0-50
4	50-100
3	100-150
2	150-200
1	200-250

• The influence of temperature is described with the mean values for May, June and July. These values were determined by interpolation of climate maps, because most of the forests that have been enumerated were not close to a weather station.

From this study a formula was derived for the S-value with these aspects:

$$S(m) = 16{,}45 - 0{,}6150\ Vgb^2 + 3{,}33\ \ln(N_{org}) + 2{,}048\ \ln(Pto) + 13{,}23\ T_{may} - 17{,}96\ T_{june} + 6{,}98\ T_{july}$$

This corresponds with previous studies in The Netherlands concerning the water- and soil content variables. But the value of the temperature variables requires some explanation. The positive values of the mean temperatures in May and July illustrates the effect of the temperature in the vegetation period on the growth. The negative value of the mean temperature in June can be explained by the connection with summer drought in this month, which is of greater influence on the growth than the temperature.

For the GIS-analysis this formula is divided in 4 sections to show the influence of the different aspects:
$C0 = 16{,}45$
$C1 = -0{,}6150\ Vgb^2$ (water content)
$C2 = 3{,}33\ \ln(N_{org}) + 2{,}048\ \ln(Pto)$ (soil type)
$C3 = 13{,}23\ T_{may} - 17{,}96\ T_{june} + 6{,}98\ T_{july}$ (temperature)

Thus $S = C0 + C1 + C2 + C3$

If you quantify these 4 sections by implementing some average values for the different parameters, the fractional portion of each section on the total S-value can be determined. In the next table, this is done for each parameter. Values can be found in the previous paragraphs about each section. Values for the temperature can be found in the next chapter about the GIS analysis.

Table 2.6 fractional values of S

Parameter	min value	max value	C	Min	Max	Average	Fraction
			C0	16,45	16,45	16,45	**1/2**
Vgb	1,5	5	**C1**	-1,4	-15,4	-8	**-1/4**
Norg	1,7	2,4	**C2**	6,7	10,0	8	**1/4**
Pto	11	32					
Tmay	11,75	12,75	**C3**	5,0	23,6	14	**1/2**
Tjune	14,25	15,25					
Tjuly	16,25	17,25					
				S = C0+C1+C2+C3		**30**	**1**

It can be seen that (apart from the constant C0) the value of C3, which is temperature-dependent, has the biggest influence on the total value for S.

2.2 GIS

The results from the study as described in paragraph 2.1 are combined in a GIS[2]-environment to visualise the relation between theory and reality.

2.2.1 Theory

The study showed that the most important aspects that influence the growth of Japanese Larch are:

1: water content
2: soil type
3: temperature

These aspects, with the information needed to derive the S-value, were put in the GIS-environment.
The parameter C1 is calculated by combining the forest area with the soil characteristics. The forest areas as described by the study of the IBN and the "Bosstatistiek" are inserted in the GIS-environment. From this, and with the information of the value VL_{gr} per soil type, the parameter V_{gb} can be calculated, which leads to the value C1. The distribution of this value shows high values in the northern and eastern part of the Netherlands and low values in the central part.

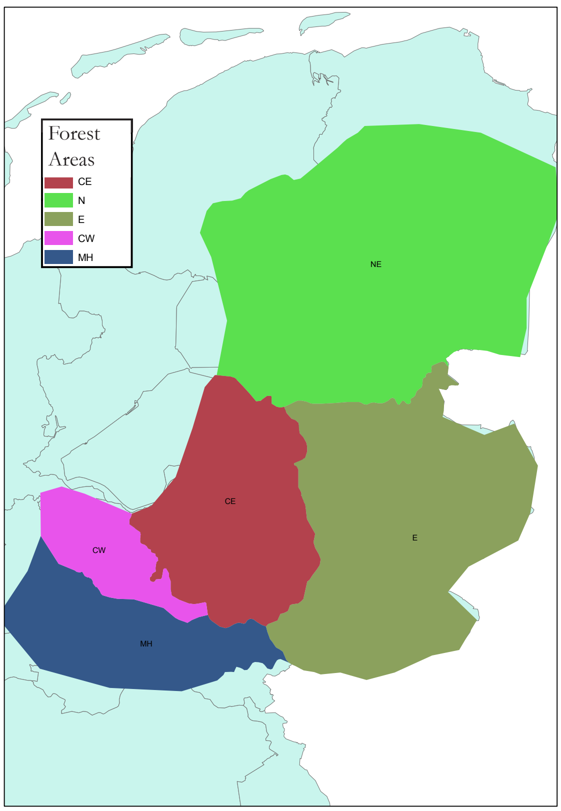

Figure 2.2 forest areas East Netherlands

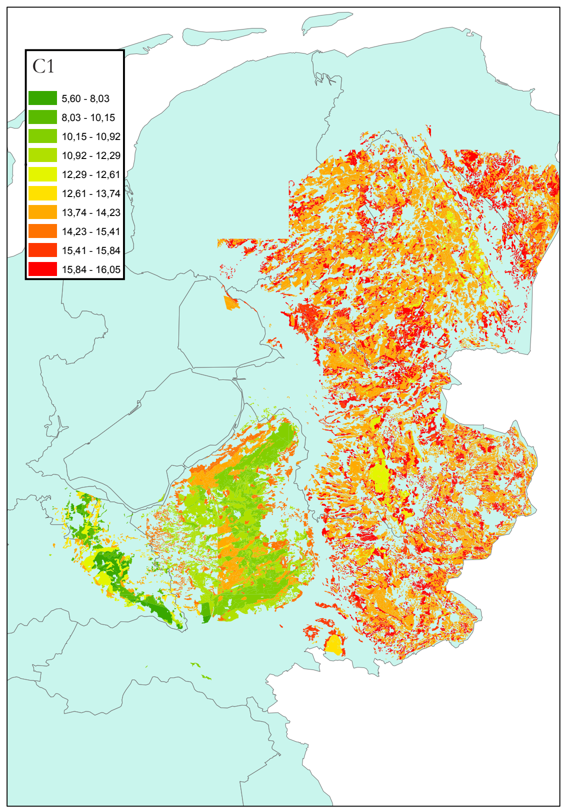

Figure 2.3 C1 Values

[2] **GIS**: **G**eographic **I**nformation **S**ystem

A digital soil map of the eastern part of The Netherlands was obtained from Alterra. Only the soil types that are discussed in the study from IBN are shown. With the information on the parameters N_{org} and P_{to} per soil type the parameter C2 is calculated. This parameter shows the influence of the soil type on the S-value. It shows that generally the soil in the south and eastern part is more suitable for larch forests than the northern part of The Netherlands. This is mostly attributed to the soil types “holtpodzol” and “zwarte enkeerd”. These soil types show high values for phosphor and nitrogen content and are mostly found in the central and eastern part of The Netherlands.

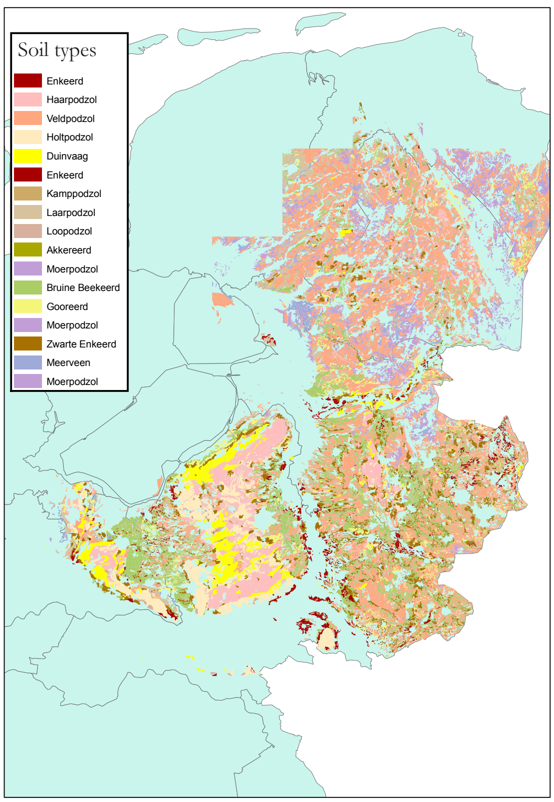

Figure 2.4 soil types Netherlands

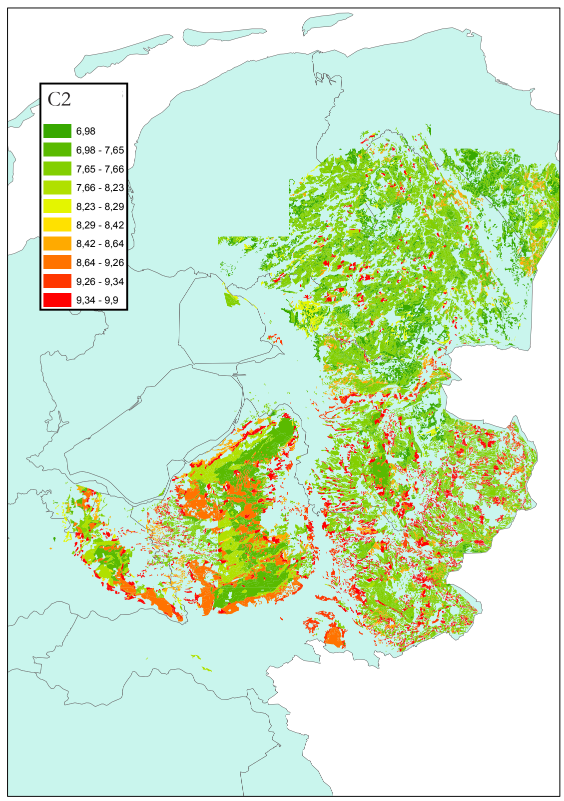

Figure 2.5 C2-values

For the temperatures, information was obtained from the website of the Royal Dutch Weather Institute, the KNMI[3]. From this the parameter C3 is calculated. This shows a high value in the central part and lower values in the northern and southern parts of The Netherlands.

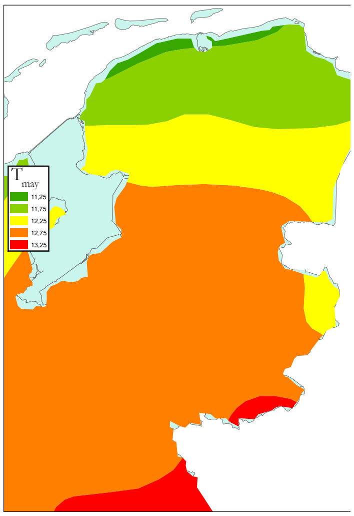

Figure 2.6 mean temperatures in May

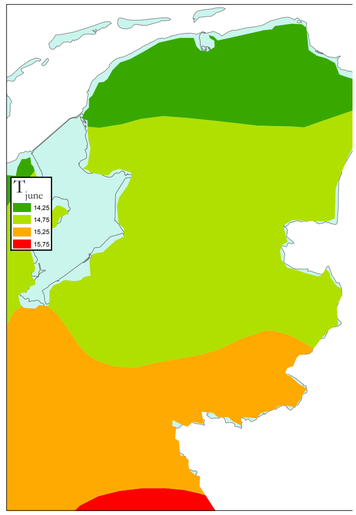

Figure 2.7 mean temperatures in June

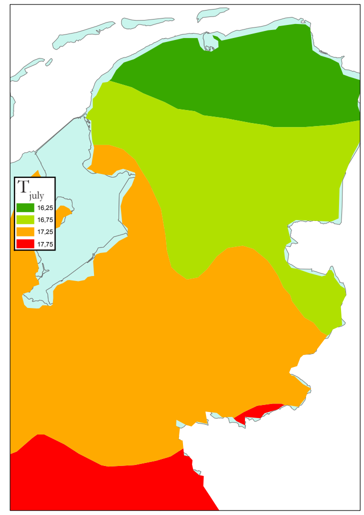

Figure 2.8 mean temperatures in July

Finally, the S-value is calculated by adding C1, C2 and C3.
This shows the high influence of the temperature on the S-value. The influence of the soil types is still visible, but not so strong. The influence of the water level does not show at all.

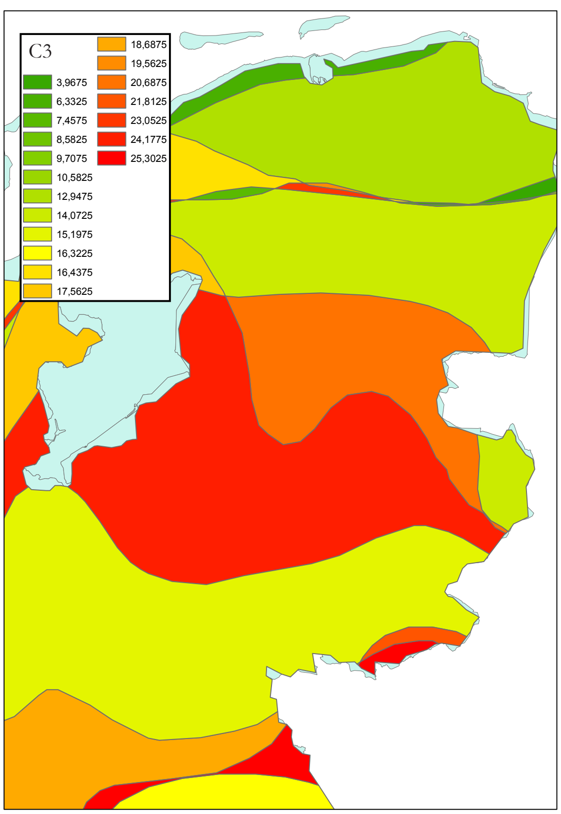

Figure 2.9 C3 values

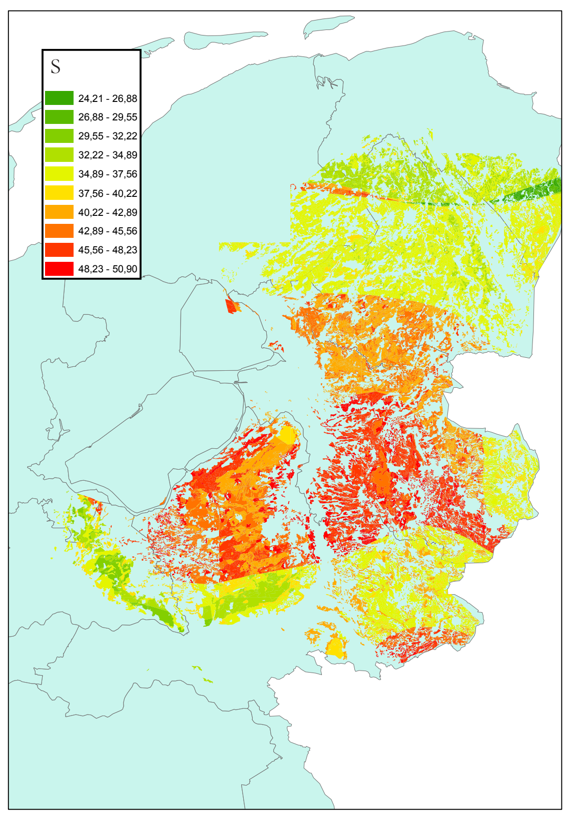

Figure 2.10 S-values

[3] **KNMI**: **K**oninklijk **N**ederlands **M**eteorologisch **I**nstituut

2.2.2 *Reality*

This theoretical value of S, referred to as S_{theory}, has to be compared to the measured S-value, referred to as $S_{reality}$, obtained by the information from the Larch plots in The Netherlands. This value is calculated by the expression:

$S_{reality} = h_{top} * (1-e^{-C7*t})^{-C8}$

For Japanese Larch, the factors C7 and C8 are 0,0405 and 1,2277 respectively [Van den Burg, 1997]. These factors are determined for a thinning-regime of once every 5 years, which coincides with the regime of "Staatsbosbeheer" [Anonymous, 1996].

To calculate this value, the GIS data with the locations of larch plots owned by "Staatsbobeheer" is combined with data about height, volume etc of these plots (table 2.7). This data was obtained from "Staatsbosbeheer", the owner of more than half of the total forest area in The Netherlands.

Table 2.7 forest data from "Staatsbosbeheer"

object [-]	**year [-]**	**plot [-]**	**germ year [-]**	**dch [mm]**	**h [m]**	**v [m³]**	**quality [-]**	**stemnr. [-/ha]**	**tree area [m²/ha]**	**tree volume [m³/ha]**	**plot area [ha]**
Bakkevee	2.003	BA54	1.942	297	16	522,66	7	198,94	12,15	112,28	3,14
Gieten	2.003	L24	1.936	357	24	1.108,89	7	245,07	17,95	180,52	4,38
Kootwmf	1.997	AX26	0	368	21	1.026,11	7	273,55	20,26	160,89	0,00
Kuinderb	1.998	AD7	1.952	314	20	726,02	3	324,81	15,60	143,56	6,66
Nunspeet	2.003	AB13	1.960	288	24	741,98	7	700,28	31,52	322,15	2,65
Odoorban	2.000	Q12	1.934	473	30	2.349,58	7	0,00	0,00	0,00	3,61
Speulban	2.000	K13	1.944	341	24	1.017,73	7	190,45	20,10	244,94	0,80
Springen	2.000	AV11	1.940	350	21	934,22	7	477,46	29,75	287,53	1,55
Westerwo	2.002	O2	1.959	301	18	603,33	7	0,00	0,00	0,00	0,55
Zwolsebo	1.997	O18	1.945	238	16	345,37	7	382,88	16,14	136,33	0,55

A description of the used data is given in table 2.8 to 2.9.

The quality levels A,B and C are forestry qualities and are determined by combining flaws, straightness and branch-ness.

Table 2.8 field description of forest data

Field	Desctiption	Unit
object	inventarisation unit (forest range etc.)	
year	year of inventarisation	
plot	section within the inventarisation unit	
germ year	year of germination	
dch	diameter at chest height of the dominant tree	mm
h	height of the dominant tree	m
v	volume of the dominant tree	dm^3
quality	quality of the dominant tree (see table)	
stem nr.	number of trees on the plot	number per ha
tree area	tree area on the plot	m^2/ha
tree volume	standing living forest on the plot	m^3/ha
plot area	area of the plot	ha

Table 2.9 quality definitions

Code	Flaws?	Straight\Bent	Branch-ness	Quality
99	yes	Bent	Very branched	C
1	no	Bent	Very branched	C
2	yes	Straight	Very branched	C
3	no	Straight	Very branched	C
4	yes	Bent	Not branched	C
5	no	Bent	Not branched	B
6	yes	Straight	Not branched	C
7	no	Straight	Not branched	A
8	yes	Bent	Branched	C
9	no	Bent	Branched	C
10	yes	Straight	Branched	C
11	no	Straight	Branched	B
102	not defined, because dch < 20 mm			

The calculated S-value from this data is shown below.

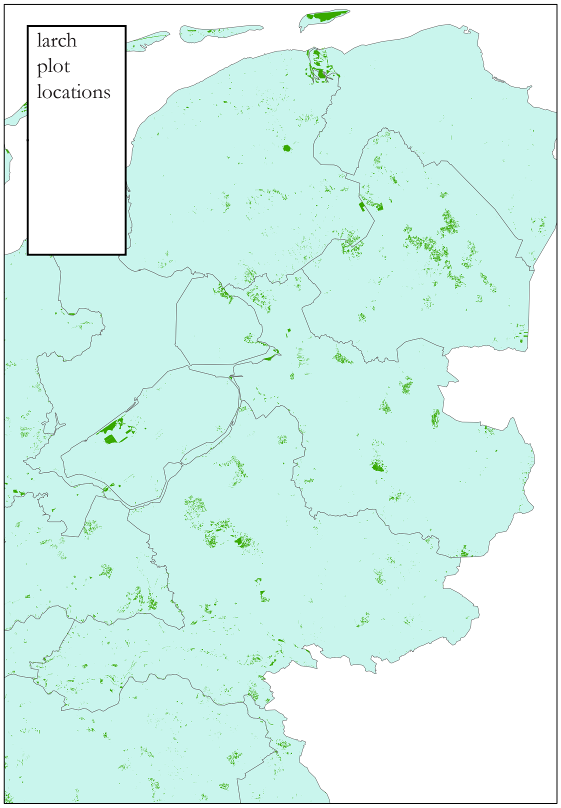

Figure 2.11 location larch forests of Staatsbosbeheer

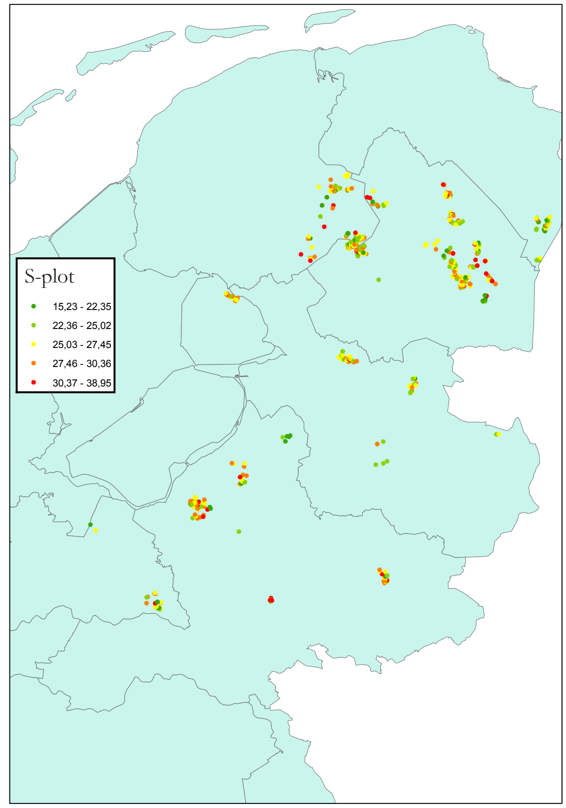

Figure 2.12 S-values from forest data

Finally, a comparison can be made between the theoretical value of S and the value obtained by information from the forests. First, the theoretical S-value is combined with the locations of larch plots. Figure 2.14 shows that larch is almost exclusively found on “podzol” soils. These are soils with a very high value for VL_{gr}, which corresponds with the assumption that larch is sensitive for dry soils.

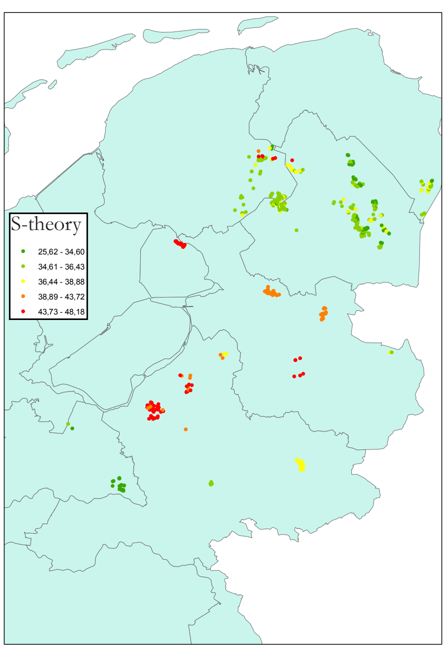

Figure 2.13 S-value from theory

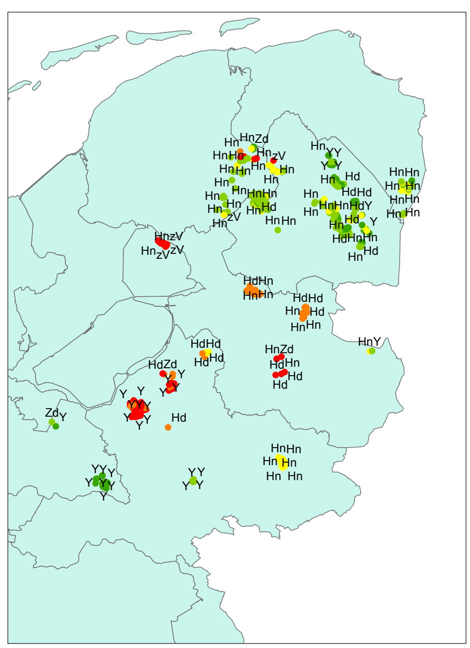

Figure 2.14 Larch plots with soil types

Next, the theoretical value of S is compared with the real value of S by substraction, which gives the value S_{diff}. To limit the influence of erroneous data some extreme values for S_{diff} have been excluded. With each figure for values of S_{diff} , a table is presented with statistical data. The value for "count" shows how many plots have been used from the forest data. The total number of plots is 587, so for this first calculation of S_{diff} 27 records have been excluded. The value for "exclusion" shows the boundaries of the exclusion.
It shows that the difference between the theoretical and the "real" value of S is quite big, especially in the central area of The Netherlands. If you compare this with the distribution of the parameter C3 it shows that the influence of this parameter is too big. In areas where the value of C3 is high, the error value is also high. Therefore, the theoretical S-value is recalculated with a new expression for C3. For each new expression for C3, a scatter diagram with the theory- and reality- values for S was made, to show the influence of the adaptation. The diagram of the current expression shows an R-squared value of almost zero and thus no relation between the theoretical and real S-values.

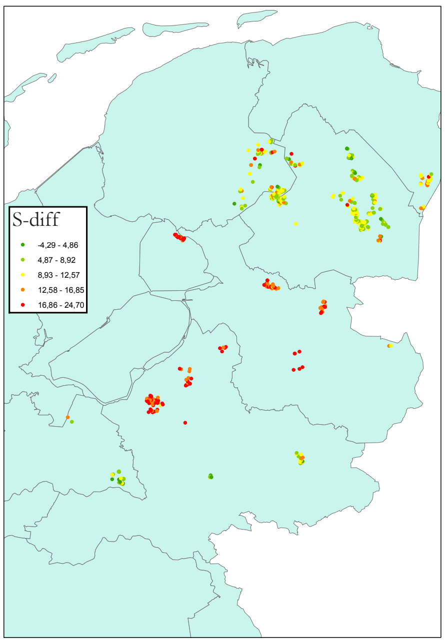

Figure 2.15 difference between S-values from theory and forest data

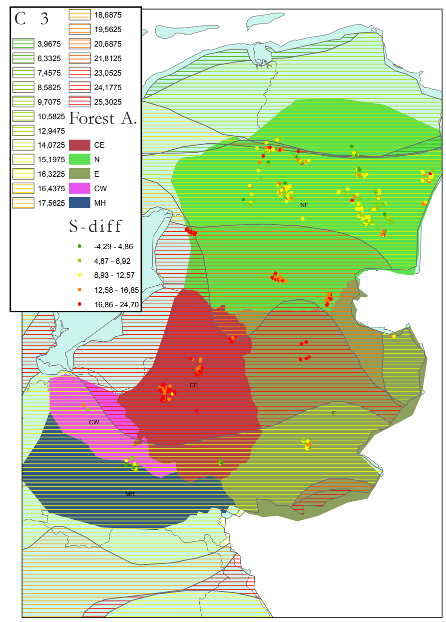

Figure 2.16 combination S_{diff}, C3 and forest areas

Table 2.10 statistical data S-diff, C3 original

	factors		S-diff
totaal		count	587
original:	A=1	count:	560
	B=1	minimum:	-4,29
	C=1	maximum:	24,7
	D=1	mean:	11,07
	E=0	st.dev.	4,85
		exclusion	-5<S<25

Table 2.11 scatter diagram S-theory and S-reality, C3 original

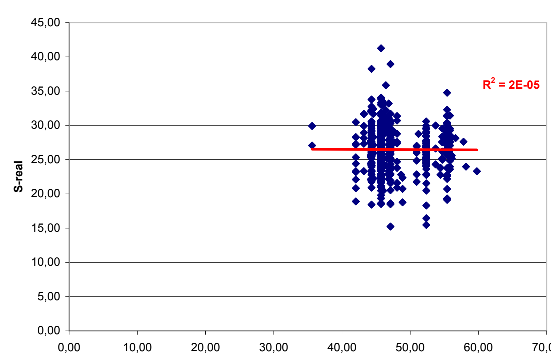

Some different expressions were tested, with the mean value and standard deviation of S-diff as indicators. The table below shows the original expression for C3 and the factors A to E that have been adapted.

Table 2.12 adapted expression for C3

	C3						
0	*(	13,23	* Tmay -	17,96	* Tjune +	6,98	* Tjuly) +	5
A		0,80		0,90		1		E
		B		C		D		

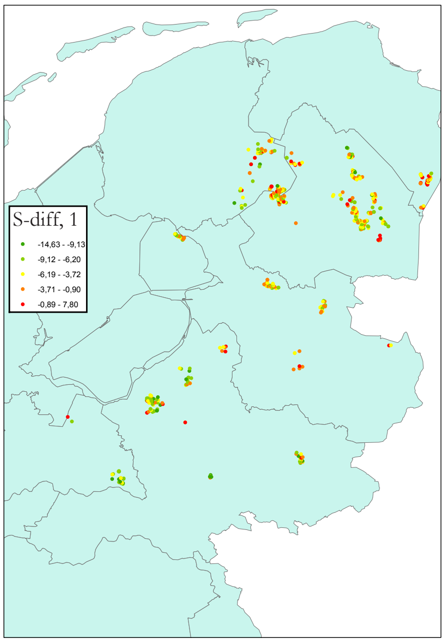

	factors		S-diff
1:	A=0	count:	563
	E=0	minimum:	-14,63
		maximum:	7,8
		mean:	-5,02
		st.dev.	3,2
		exclusion	-15<S<15

Figure 2.17 $S_{diff,1}$

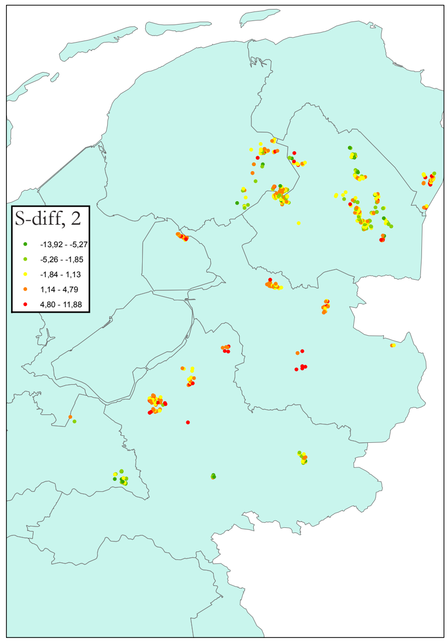

	factors		S-diff
2:	A=0,5	count:	565
	B=0,8	minimum:	-13,92
	C=0,9	maximum:	11,88
	D=1	mean:	-0,06
	E=0	st.dev.	3,64
		exclusion	-15<S<15

Figure 2.18 $S_{diff,\ 2}$

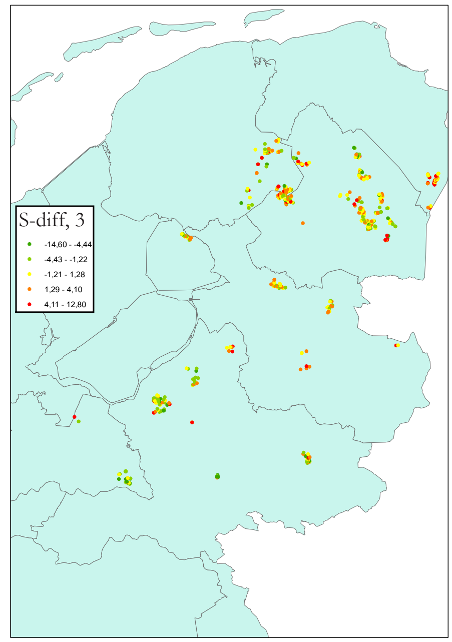

	factors		S-diff
3:	A=0	count:	566
	E=5	minimum:	-14,6
		maximum:	12,8
		mean:	-0,09
		st.dev.	3,32
		exclusion	-15<S<15

Figure 2.19 $S_{diff,\ 3}$

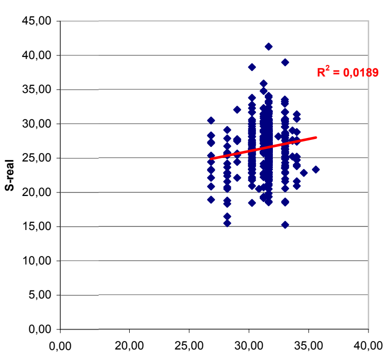

Figure 2.20 scatter diagram S-theory and S-reality, C3 1

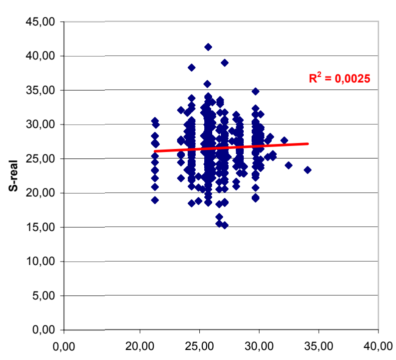

Figure 2.21 scatter diagram S-theory and S-reality, C3 2

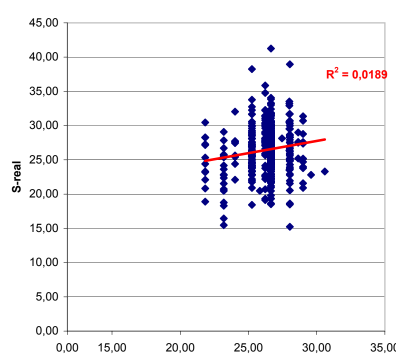

Figure 2.22 scatter diagram S-theory and S-reality, C3 3

If the factor A, and thus the value for C3, is set to zero (figure 2.19), the scatter diagram shows a large spread in real S-values for constant theoretical S-values. Further inspection of the Excel sheet in which these values were determined shows that for constant parameters for S-theory (constant temperatures, water content parameters and soil types) a large spread in values for S-reality is found. From this it can be concluded that in order to make a more accurate prediction of the S-value for Japanese larch in the Netherlands, more parameters need to be included in the formula. A suggestion was made by ing. Z. van Olst MBA from "Staatsbosbeheer" to include the parameter for area per tree, since this influences the growth direction of Japanese larch. When this area is small, the tree will grow higher. A first test with this extra parameter did not show an increase in accuracy of the S_{theory} value, but further study on this is needed to come to a more definitive conclusion.

Also the results show that the difference between the theoretical and real value of S is much bigger than the accurateness of the theoretical value suggests (0,1m).

Finally it can be concluded that it's doubtful whether the theoretical calculation of S is useful as a predictor for the growth of Japanese Larch in The Netherlands. Because the real value for the Site index is known for a large amount of plots from "Staatsbosbeheer", this parameter can still be checked for a relation with the strength parameters of Japanese larch round wood

Table 2.13 part of Excel sheet for calculation of S-values

Forest	Soil Type	VLgr	Vgb	Tmay	Tjune	Tjuly	S-theory	S-reality
NO	zV	2,30	1,10	12,25	14,75	16,75	34,00	31,36
NO	zV	2,30	1,10	12,25	14,75	16,75	34,00	30,71
NO	zV	2,30	1,10	12,25	14,75	16,75	34,00	28,78
NO	zV	2,30	1,10	12,75	14,75	16,75	34,00	27,58
NO	zV	2,30	1,10	12,75	14,75	16,75	34,00	27,58
NO	zV	2,30	1,10	12,25	14,75	16,75	34,00	27,58
NO	zV	2,30	1,10	12,25	14,75	16,75	34,00	27,37
NO	zV	2,30	1,10	12,75	14,75	16,75	34,00	25,18
NO	zV	2,30	1,10	12,25	14,75	16,75	34,00	24,70
NO	zV	2,30	1,10	12,75	14,75	17,25	34,00	23,98
NO	zV	2,30	1,10	12,25	14,75	16,75	34,00	23,80
NO	zV	2,30	1,10	12,25	14,75	16,75	34,00	21,58
NO	zV	2,30	1,10	12,25	14,75	16,75	34,00	20,90

2.3 Experiment

To be able to find a relation between the S-value and strength, tests have to be done on trees from a variety of locations in The Netherlands.

From the theoretical S-value that was calculated initially, it showed that there are roughly three different areas:

- the area around the "Veluwe" with the highest values
- the northern part with the lowest values
- the southern part with average values

To be able to make a good prediction, a request was made to "Staatsbosbeheer" for three times twenty trees from these areas. Because "Staatsbosbeheer" only goes to each plot once every 5 years, this request could not be fulfilled at once. At the time of writing, one series of twenty trees was felled and tested for visual aspects. The other two series are planned for a later stadium and could well fall beyond the time frame of this project. Because there is a good relation between density and strength of wood, this is the parameter that will be measured first. Also, this is an easy aspect to determine.

2.3.1 Density

The first series of twenty trees are from "Smilde" in the the province of "Drenthe". From these 4m long stems, a small slice is cut to count the year rings and measure the clearwood density. This is the density of knot-free wood. Secondly, 25 slices are used from stems that were used for the viewing platform that was built for "Staatsbosbeheer". And finally 20 slices are used from new stems as replacement for the viewing platform. These stems are from " 's Herenberg" in the southern area.

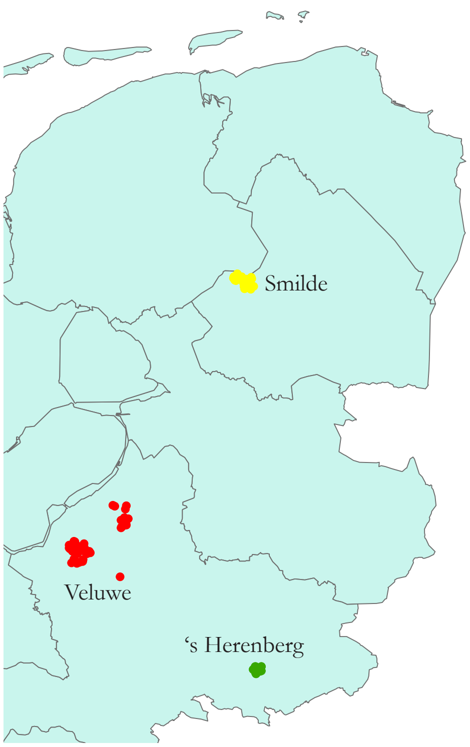

Figure 2.23 plot locations

In the next tables, the mean and characteristic values of $\rho_{12\ \text{clearwood}}$ are determined for the three different series. The determination of these values is described in Appendix A4, the total data sheet is shown in Appendix A5.

From the first series of 's Herenberg, the data is aquired twice. First, the results are shown from the data collection that was done when this series first arrived at the Technical University in Delft (denoted with "Original"). From each specimen, four slices were cut at different locations. Two of these slices were tested.
Then, for this report the same specimen were tested again, but the used slices from these specimen were not always identical. This is because at the time of the data collection for this report, the initial data was not known by the author. Results from this new data collection are denoted with "New".
Also the total data collection is shown (denoted with "Total").
The mean and characteristic values of $\rho_{12\ \text{clearwood}}$ of the original and new data series show a small diference, which can be explained by the difference in used slices.

Goriginal [gram]	Gdry [gram]	MC [%]	Gunderwater [gram]	Gwet [gram]	Gwater [gram]	Volume [mm^3]	ρmc cw [kg/m^3]	βv [%%]	ρ0 cw [kg/m^3]	ρ12 cw [kg/m^3]	
64,36	59,86	3,36	-56,78	61,84	-118,62	118860	523,03	0,52	515,03	542,63	mean (New)
										35,13	stdev
										455,81	characteristic
										6,5%	covariance

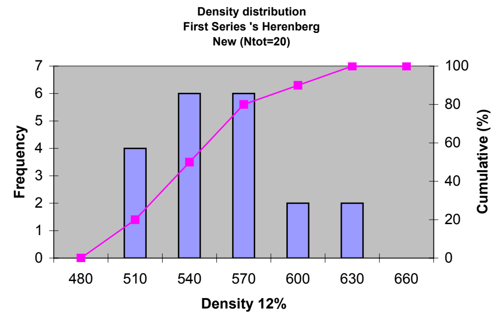

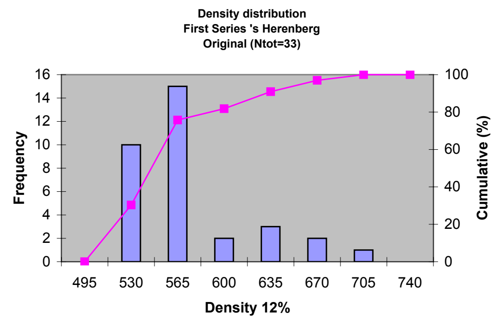

ρ0 cw [kg/m^3]	ρ12 cw [kg/m^3]	
528,33	557,64	mean (Original)
	47,17	stdev
	468,41	characteristic
	8,5%	covariance

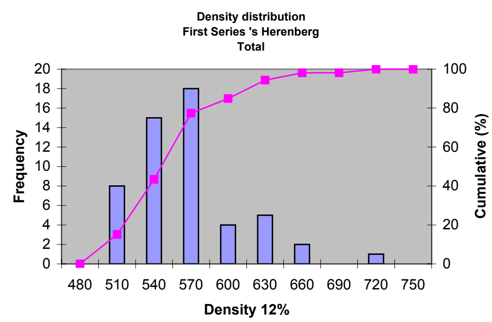

ρ0 cw [kg/m^3]	ρ12 cw [kg/m^3]	
523,31	551,97	mean (Total)
	43,64	stdev
	463,66	characteristic
	7,9%	covariance

Figure 2.24 ‘s Herenberg, first series, diameter = 11,3 cm

Goriginal [gram]	Gdry [gram]	MC [%]	Gunderwater [gram]	Gwet [gram]	Gwater [gram]	Volume [mm^3]	ρmc cw [kg/m^3]	βv [%%]	ρ0 cw [kg/m^3]	ρ12 cw [kg/m^3]	
158,18	134,38	4,12	-149,25	139,31	-288,56	289138	481,58	0,48	471,89	499,29	mean
										56,08	stdev
										419,40	characteristic
										11,2%	covariance

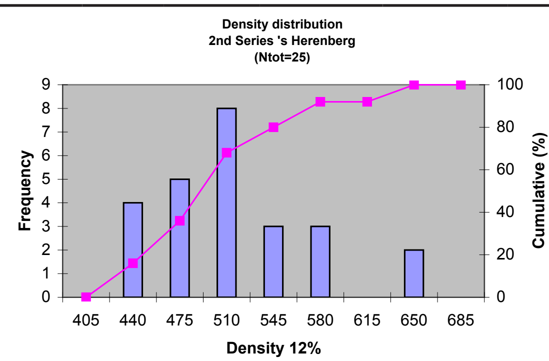

Figure 2.25 ‘s Herenberg, second series, diameter = 13,8 cm

Goriginal [gram]	Gdry [gram]	MC [%]	Gunderwater [gram]	Gwet [gram]	Gwater [gram]	Volume [mm^3]	ρmc cw [kg/m^3]	βv [%%]	ρ0 cw [kg/m^3]	ρ12 cw [kg/m^3]	
207,90	177,29	3,52	-152,51	182,85	-335,36	336029	537,34	0,54	528,97	556,37	mean
										41,84	stdev
										476,35	characteristic
										7,5%	covariance

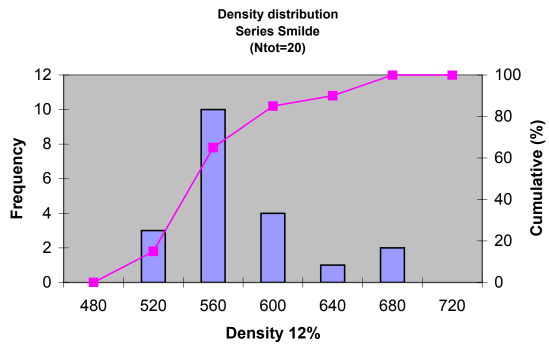

Figure 2.26 Smilde, diameter = 13,8 cm

The distribution graphs show a generally large amount of low density values. This causes lower characteristic values and relatively large standard deviations and covariances.
Also, the characteristic values for ρ_{12} are not as expected. The first series from 's Herenberg, that was used as construction wood for the viewing platform, shows a high value, but the second series is of a much lower density.
And the series from Smilde, which was not selected by any criterium, even shows the highest density values.
Also it must be noted, that the first and second series from 's Herenberg have been visually graded to meet the mechanical properties needed for the construction of the viewing platform. The series from Smilde have not been selected via any standard, to get an as natural selection from the forest as possible.

The used densities for the determination of any relation with the S-values are the (average) mean clearwood density values:
's Herenberg : $\rho_{12\ cw} = (551{,}97 + 499{,}29)/2 = 525{,}63$ kg/m^3
Smilde : $\rho_{12\ cw} = 556{,}37$ kg/m^3

Also, information was gathered about growth rings. This is primarily done to get the same information as was obtained in the CONIFERS project to be able to compare the data. Also, growth ring data is an important parameter in the quality characterisation for round wood.

The following aspects were recorded (figure 2.27):
• The minimum distance of pith to edge (P-E)
• The maximum number of growth rings and the accompanying width (N_{max}, R_{max} [mm])
• The number of complete (not cut through) rings and the accompanying minimum and maximum width ($N_{complete}$, $R_{complete,min}$, $R_{complete,max}$ [mm])
• The number of rings in the first 20 mm from the pith (N_{20})

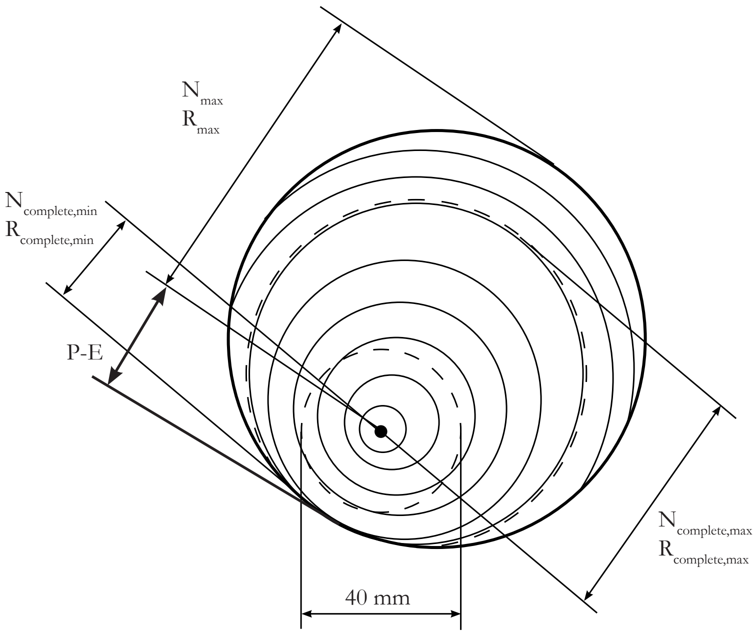

From this data the following characteristics were calculated:
• The average complete ring width:
$RW_{complete} = (R_{c,min}+R_{c,max})/(2*N_{complete})$
• The average maximum ring width:
$RW_{max} = R_{max}/N_{max}$
• The average maximum ring width outside the first 20 mm from the pith:
$RW_{max\text{-}N20} = (R_{max}-20)/(N_{max}-N_{20})$
• The Pith excentricity:
Pith = Diameter/2 - (P-E)

Figure 2.27 growth ring characteristics

In the next figures, the results are shown for the different series. The complete data set is shown in Appendix A5. Also, the characteristic values for each series are shown. In the scatter diagrams the recorded average maximum ring width outside the first 20 mm from the pith ($RW_{max\text{-}N20}$) is drawn in relation to the density of the slice. These show R-squared values in the range of 0,35 - 0,5. This is an acceptable, but not very strong relation. The low value for the series from Smilde is explained by the small number of slices from this series. Because the relation between the ring width and the density is not very strong and the determination of this value is quite time consuming, this parameter is rejected as a predictor for the density and thus the strength of larch round wood. Therefore, the ring width from slices has not been determined for the other 14 trees from the series from Smilde.
In the diagrams the limits for the classes according to NEN 5466 (table 2.14) are drawn to show the quality of the different series. What can clearly be seen is that, in accordance wtih the results from the density experiments, the first series from ‘s Herenberg and from Smilde are of a much higher quality than the second series from ‘s Herenberg. According to the NEN 5466, wood with a quality class of A and B can be put in strength class C24 and class C can be put in strength class C18. This is for sawn timber, classes for round wood have yet to be determined.

Table 2.14 quality classes NEN 5466

	Quality Class			
	A	B	C	D
year ring width [mm]	4	5	6	-

	Ntot [-]	P-E [mm]	Pith [mm]	Nc [-]	Nmax [-]	Rc min [mm]	Rc max [mm]	Rmax [mm]	N20 [-]	RWc [mm]	RW max [mm]	RW max-N20 [mm]	ρ12,ch. [kg/m³]
New	20	39,15	29,85	12,10	26,65	34,76	43,17	76,64	5,35	3,60	2,99	2,81	455,81
Original	35	40,71	28,29	12,76	25,97	40,18	43,24	76,76	5,32	4,18	3,47	3,00	468,41
Total	55	40,13	28,87	12,52	26,22	38,17	43,21	76,72	5,33	3,96	3,29	2,93	463,66

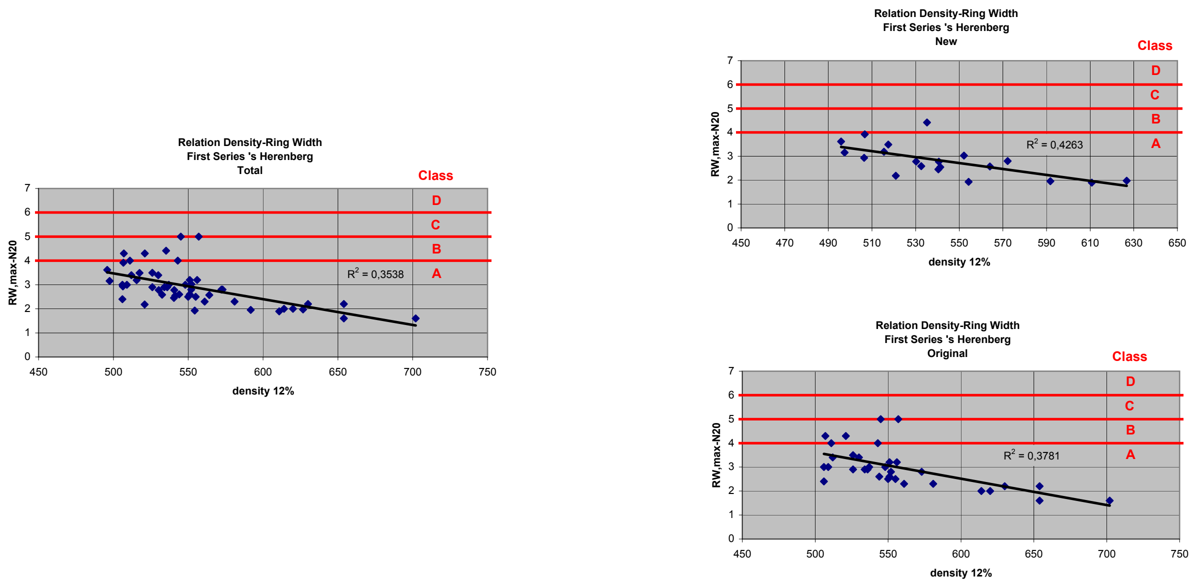

Figure 2.28 ‘s Herenberg, first series, diameter = 11,3 cm

Ntot [-]	P-E [mm]	Pith [mm]	Nc [-]	Nmax [-]	Rc min [mm]	Rc max [mm]	Rmax [mm]	N20 [-]	RWc [mm]	RW max [mm]	RW max-N20 [mm]	ρ12,ch. [kg/m³]
25	49,91	19,09	10,00	18,88	43,88	54,58	87,06	3,32	5,55	5,21	4,97	419,40

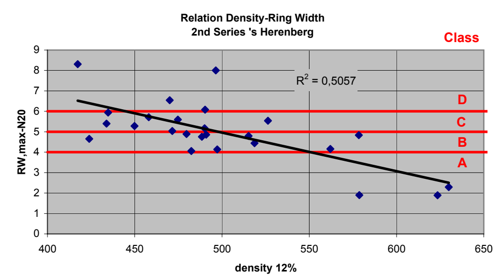

Figure 2.29 ‘s Herenberg, second series, diameter = 13,8 cm

Ntot [-]	P-E [mm]	Pith [mm]	Nc [-]	Nmax [-]	Rc min [mm]	Rc max [mm]	Rmax [mm]	N20 [-]	RWc [mm]	RW max [mm]	RW max-N20 [mm]	ρ12,ch. [kg/m³]
8	56,60	12,40	18,25	29,88	46,66	58,26	80,33	7,13	3,02	2,94	2,93	450,26

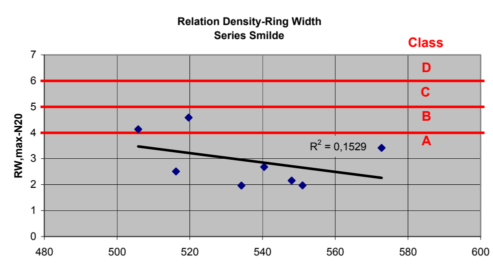

Figure 2.30 Smilde, diameter = 13,8 cm

2.3.2 *Bending Strength*

In this paragraph the setup and results from the bending tests are described. To be able to find a relation between the characteristics of the timber and it's bending strength, before doing the bending and compression tests, the beams were first visually graded. The beams were checked for knot sizes, ring width, pith excentricity, slope of grain, sweep and discoloured streaks. The procedure is descibed more in detail in Appendix A4, results are presented here.

Table 2.15 visual grading classes

	Density			Load Area	Total Area				
Nr	weighed density (12%)	clearwood density (12%) from slice	difference	Class by knot ratio DIN	Class by knot ratio DIN	Class by Slope of grain DIN	Class by Ring Width DIN	Class Bow DIN	Class Color Ratio DIN
[-]	[kg/m3]	[kg/m3]	[%]	[-]	[-]	[-]	[-]	[-]	[-]
E1	550	535	3	S10	S10	S10	S10	S13	S13
E2	558	541	3	S10	S10	S10	S13	S13	S13
E3	567	535	6	S7	S10	S13	S13	S13	S13
E4	592	568	4	S10	S10	S13	S13	S13	S13
E5	588	564	4	S7	S10	S13	S13	S13	S13
E6	522	548	-5	S13	S10	S13	S13	S13	S13
E7	582	553	5	S13	S10	S10	S13	S13	S7
E8	545	526	4	S10	S10	S13	S13	S13	S13
E9	684	643	6	S10	S10	S13	S13	S13	S13
E10	605	578	4	S13	S10	S13	S13	S7	S7
E11	638	612	4	S10	S10	S13	S10	S13	S13
E12	571	582	-2	S10	S10	S13	S13	S13	S13
E13	544	499	8	S10	S10	S13	S13	S13	S13
E14	523	487	7	S10	S10	S10	S13	S13	Reject
E15	566	551	2	S10	S7	S10	S13	S13	S13
E16	552	515	7	S10	S10	S10	S13	S13	S13
E17	540	547	-1	S13	S13	S13	S13	S13	S13
E18	555	528	5	S10	S10	S13	S13	S13	S13
E19	591	558	6	S10	S10	S13	S13	S13	S13
E20	720	656	9	S10	S10	S13	S13	S13	S13

The density was obtained by dividing the weight of the specimen by its volume and correcting for the moisture content. If this value is compared to the clearwood density obtained by weighing a slice from the specimen, the difference can be significant. Lower values for the clearwood density can be explained by the very high density of the knots, and thus a large difference can indicate a specimen has many knots. But higher values for the clearwood density are harder to explain. An explanation could be that in cases where the clearwood density is higher, a slice was taken from a part of the specimen with a higher density compared to the rest of the specimen.

In the next evaluation of the results, the clearwood density is taken as the indicator for the density of the specimen, because this value is independent of other parameters of timber.

As described in the appendix, tests were also done with a timber grader, called "Specht" and a frequency meter to determine the Modulus of Elasticity of the specimen and compare these with values obtained from the bending tests.

Table 2.16 results timber grader and frequency meter

	Timber Grader			Frequency Meter				
Nr	density at 12%	MOE static at 12% mc	Class	frequence	MOE dynamic at current mc	MOE dynamic at 12% mc	MOE static at 12% mc	Difference Frequence Meter - Timber Grader
[-]	[kg/m3]	[N/mm2]	[-]	[Hz]	[N/mm2]	[N/mm2]	[N/mm2]	[%]
E1	546	8170	C18	496	9092	9092	8546	4
E2	559	9456	C24	537	10145	10145	9536	1
E3	560	9825	C24	541	10749	10789	10141	3
E4	585	11617	C30	581	12522	12480	11732	1
E5	592	10590	C30	559	11551	11551	10858	2
E6	524	8242	C18	508	8787	8752	8227	0
E7	584	11034	C30	546	11702	11662	10962	-1
E8	539	10112	C24	544	10803	10762	10116	0
E9	688	12599	C35	538	13322	13287	12490	-1
E10	598	10536	C30	543	11342	11305	10627	1
E11	640	11855	C35	537	12162	12126	11398	-4
E12	571	10473	C24	548	10803	10728	10084	-4
E13	540	9238	C24	527	9687	9650	9071	-2
E14	519	9599	C24	556	10242	10202	9589	0
E15	559	10289	C24	530	10819	10781	10134	-2
E16	547	10252	C24	565	11002	11002	10341	1
E17	536	12622	C30	608	13507	13507	12696	1
E18	549	10316	C24	543	10968	11009	10349	0
E19	586	11317	C30	559	11994	11954	11237	-1
E20	714	14001	C35	567	14749	14716	13833	-1

The values obtained by the frequency meter with the equation $E_{m,dyn} = 4l^2 f^2 \rho$ are dynamic values for the Modulus of Elasticity. To compare these with the values given by the timber grader, they need to be converted to the static Modulus of Elasticity. According to W.F. Gard from the section Structural and Building Engineering, the global static value is 6% lower than the dynamic value for Larch. If these values are compared, it shows that the timber grader mostly gives conservative values, which is what would be expected from any grading machine. For some specimen, the timber grader gives higher values. The reason for this is not yet found, for this the theoretical calculations behind the determination of the static value of the timber grader need to be examined.

To show the relations between the different characteristics, table 2.17 shows the r-squared values.

This shows high relations between MOE_{dyn} and MOE_{stat}, as well as between the density and the two MOE-values. All the other relations are very weak.

Table 2.17 correlation factors

	ring width	density	MOE_{dyn}	MOE_{stat}	slope of grain	knot ratio
ring width	1,00					
density	0,01	1,00				
MOE_{dyn}	0,04	0,50	1,00			
MOE_{stat}	0,05	0,54	0,98	1,00		
slope of grain	0,01	0,13	0,09	0,08	1,00	
knot ratio*Kknot	0,00	0,07	0,11	0,13	0,22	1,00

To determine the bending strength, 4-point bending tests were done in accordance with NEN-EN 408 (figure 2.31). The detailed description of these tests can be found in Appendix A4.

Each beam was tested twice: once elastically with a set deformation of 2 mm/min untill 0,4 times the expected maximum load and once with a set deformation of 20 mm/min until rupture (figure 2.34).

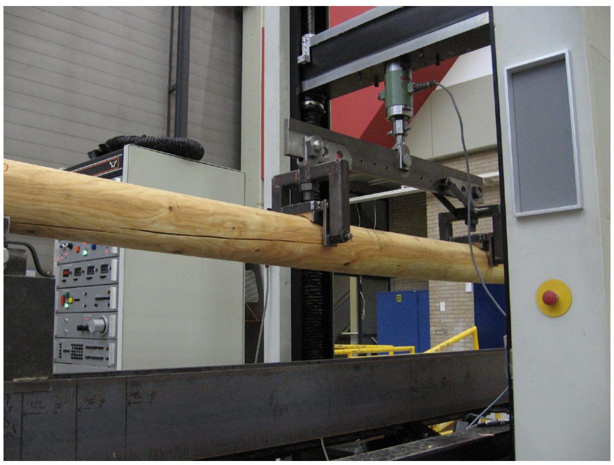

Figure 2.31 4-point bending test

From the elastical tests the local and global modulus of elasticity were determined (MOE_{local} and MOE_{global}). From the rupture tests the rupture modulus of elasticity ($MOE_{rupture}$) and the bending strength or modulus of rupture (MOR) were determined. The results from one specimen (E3) are presented below. Results of the whole series are shown in Appendix A5.

First, the beam is loaded untill 5 kN, then unloaded to almost 0 kN and loaded again untill around 15 kN, which is 0,4 times the expected maximum load (figure 2.33).

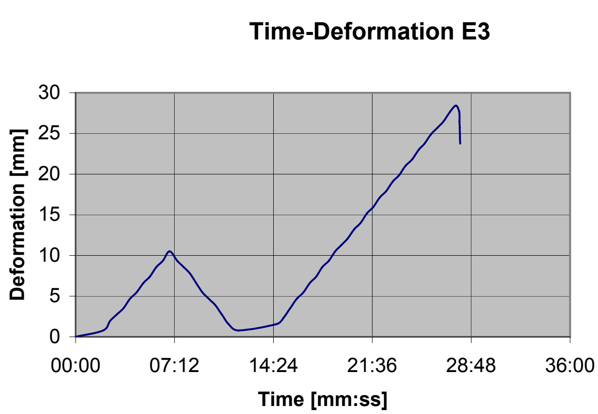

Figure 2.32 elastic time-deformation load graph of specimen E3

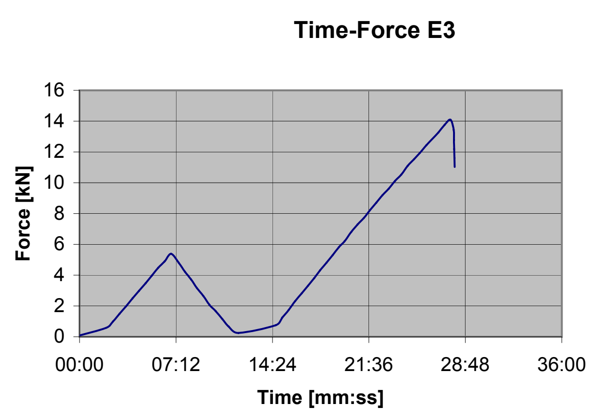

Figure 2.33 elastic time-force load graph of specimen E3

On the beam, 2 LVDT's (LVDT 3 and 4, figure 2.36) are used to determine the local bending over 5 times the diameter of the beam (figure 2.34). From these two readings the local deflection of the center of the beam can be determined (Wcl total, figure 2.37). A linear regression over 0,1 to 0,4 times the maximum load is used to determine the local modulus of elasticity. This maximum load is determined later during the tests untill rupture.

From LVDT 1 and 2 the global deflection of the center of the beam (Wcg total) is calculated. Also, here a linear regression over 0,1 to 0,4 times the maximum load is used to determine the global modulus of elasticity (figure 2.38).

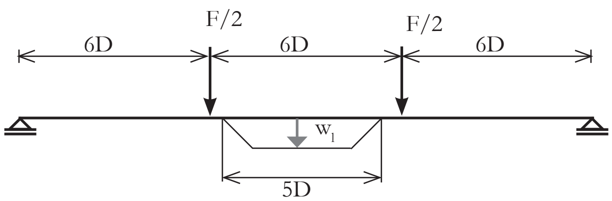

Figure 2.34 local deformation

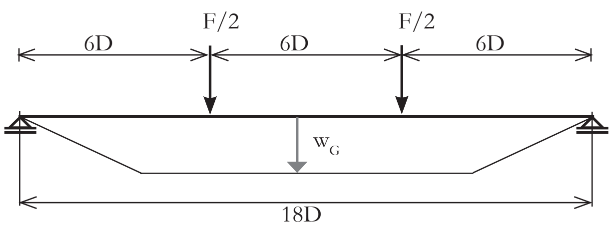

Figure 2.35 global deformation

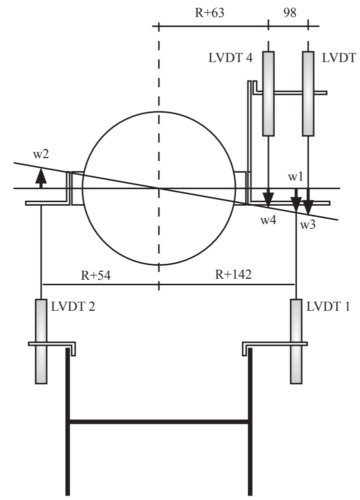

Figure 2.36 location of LVDT's

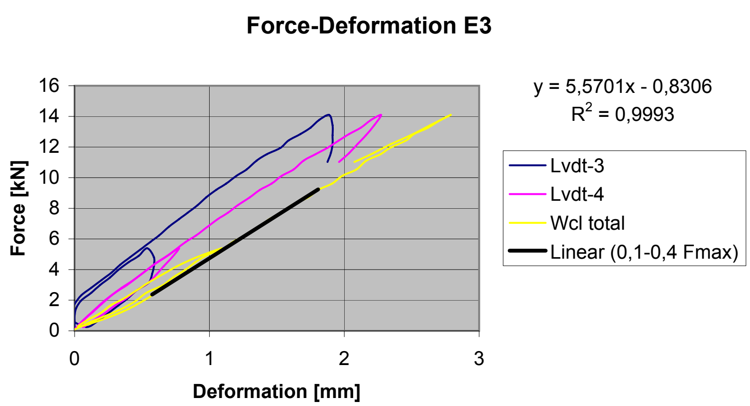

Figure 2.37 force-deformation load graph of specimen E3

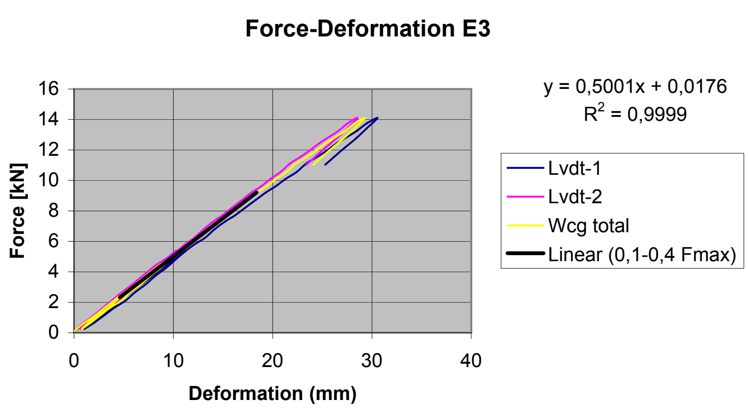

Figure 2.38 force-deformation load graph of specimen E3

From the regression lines ΔF can be calculated over Δw. Then, MOE_{local} and MOE_{global} are calculated via (Appendix A4):

$$MOE_{local} = \frac{600 F D^3_{test}}{\pi w_{cl} D^4_{original}}$$

$$MOE_{global} = \frac{6624 F D^3_{test}}{\pi w_{cl} D^4_{original}}$$

After the elastic bending test, all the LVDT's are removed and only a potmeter is used to determine the central deflection of the beam (figure 2.41). This is done because of large and very sudden deformations which could damage the LVDT's.

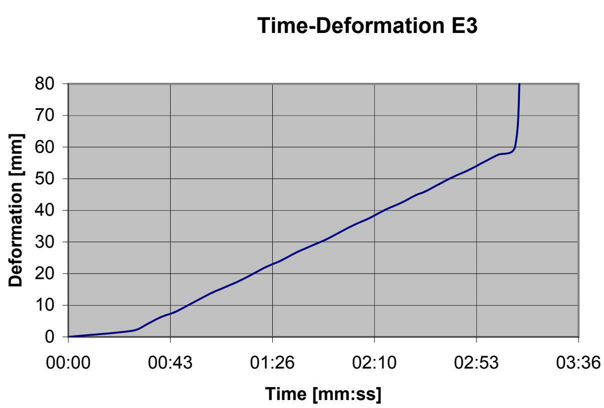

Figure 2.39 rupture time-deformation load graph of specimen E3

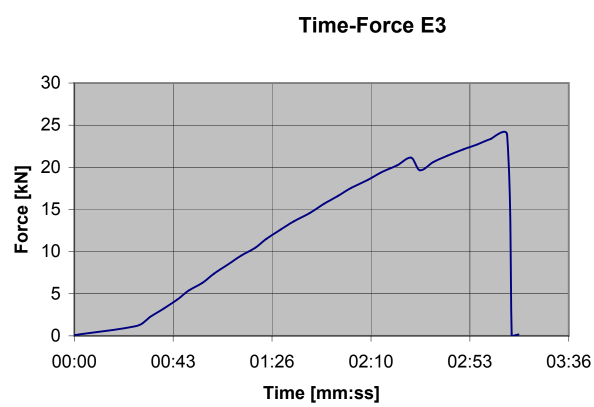

Figure 2.40 rupture time-force load graph of specimen E3

Figure 2.41 rupture force-deformation load graph of specimen E3

From the deformation curve of the potmeter, a regression line is made on the elastical part starting from 0,1 times the maximum force.
Then MOR is calculated via the same formula as for MOE_{global}. The bending strength is calculated via:

$$f_m = \frac{96 F_{max} D_{test}}{\pi D^3_{original}}$$

The results from the 20 trees from the series from the Elspeterbos are presented in table 2.18. The two values in red are obtained from a regression line with an r-squared value of less than 0,99 and are therefore unreliable.

Table 2.18 results MOE and MOR from bending tests

Nr	MOE local	MOE global	MOE rupture	MOR
[-]	[N/mm2]	[N/mm2]	[N/mm2]	[N/mm2]
E1	7402	7249	7340	37,36
E2	7781	7870	7898	36,41
E3	8533	8458	8446	40,61
E4	9630	9408	9474	48,92
E5	9041	8616	8861	55,48
E6	6481	7074	7105	41,75
E7	9477	8557	8048	43,85
E8	9265	8679	8551	43,71
E9	9804	9706	10056	64,41
E10	9322	8556	8806	36,66
E11	8470	9306	9378	43,72
E12	8773	8258	8434	47,45
E13	8774	8126	8260	41,59
E14	8232	8498	8919	31,58
E15	8281	8018	8152	37,93
E16	8453	9209	9677	38,21
E17	11029	10069	10455	34,15
E18	8799	8187	8654	54,42
E19	9473	8525	8879	62,74
E20	11364	10765	11235	66,83

These scatter diagram show the relation between the determined characteristics and the density.

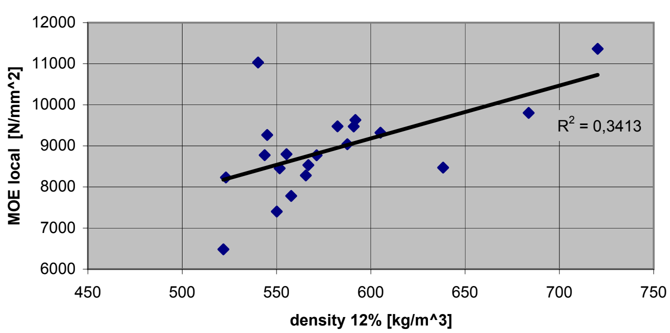

Figure 2.42 correlation MOE_{local} and density

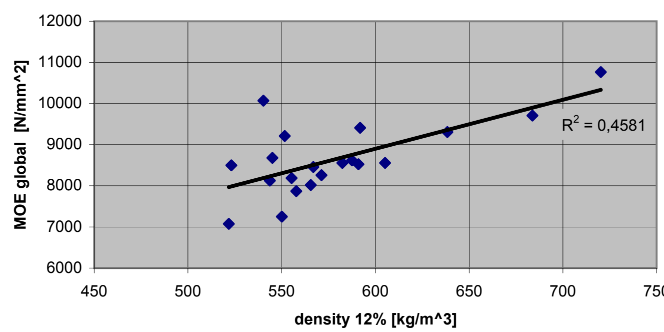

Figure 2.43 correlation MOE_{global} and density

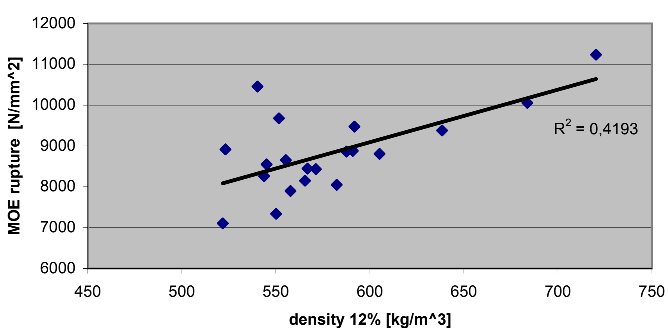

Figure 2.44 correlation $MOE_{rupture}$ and density

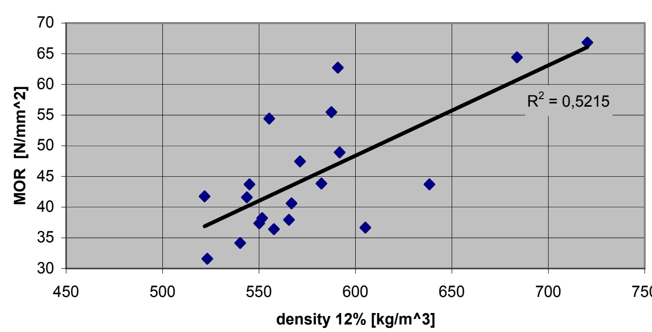

Figure 2.45 correlation MOR and density

This data was compared with previous results from the CONIFERS project. The scatter diagrams below show the relations between MOE_{local} and MOR and the density of the different series.

From these graphs it can be clearly seen that, although the densities are in the same range, the values for MOE_{local} and MOR are much lower from the series from Smilde than from the previously tested series

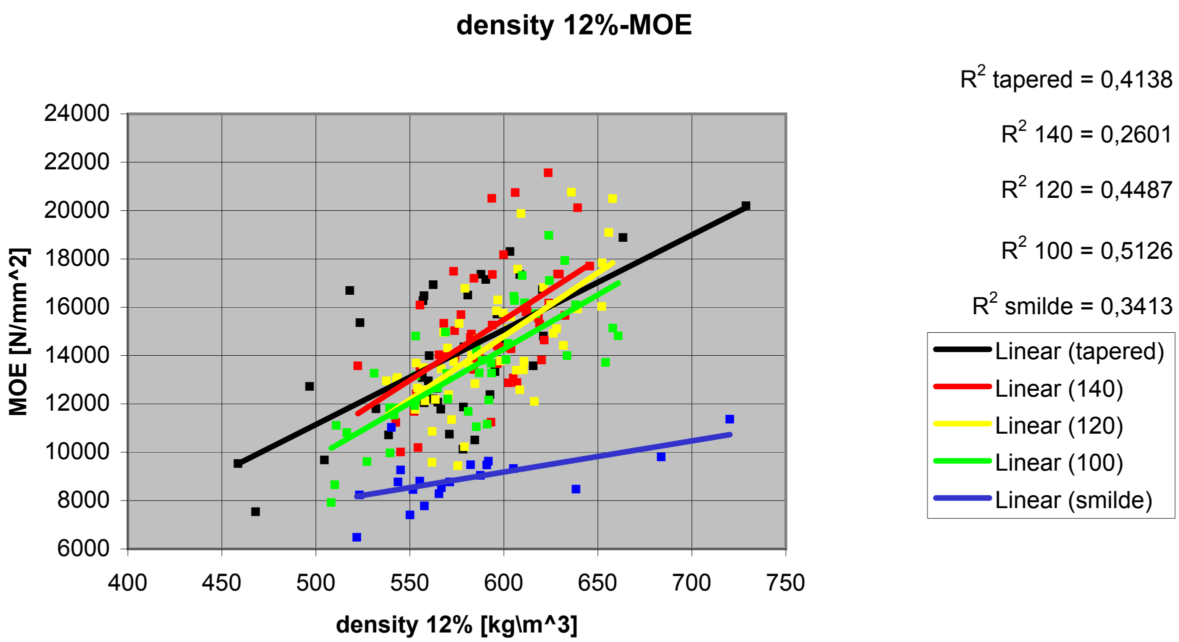

Figure 2.46 correlation MOE_{local} and density all series

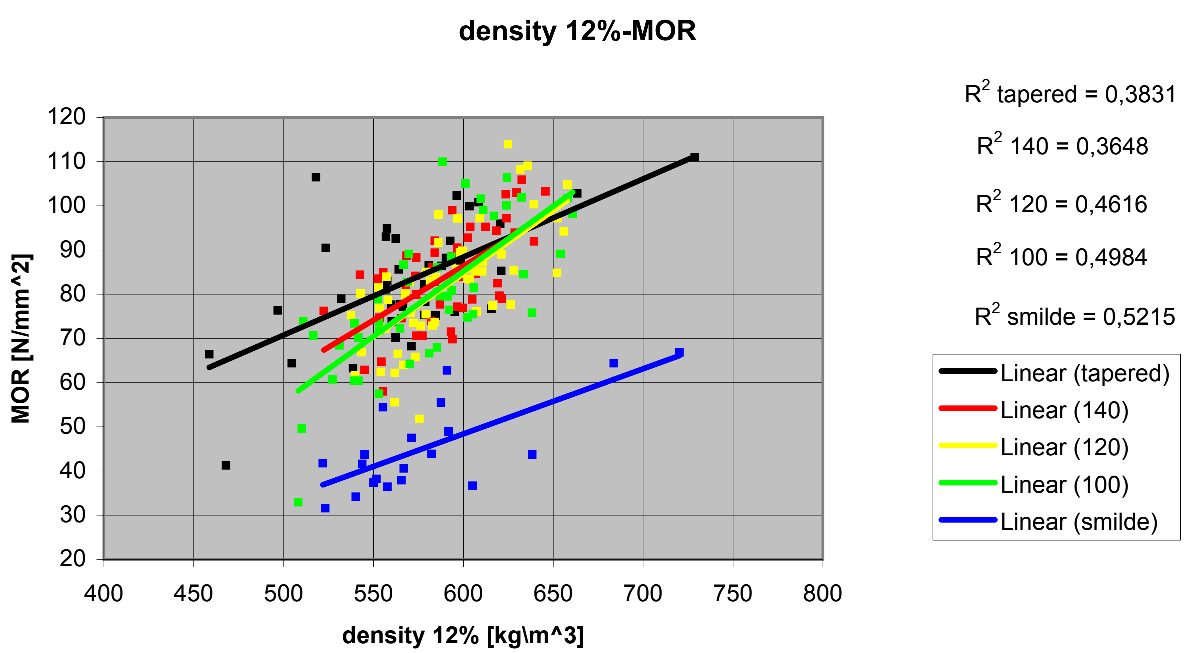

Figure 2.47 correlation MOR and density all series

2.3.3 *Compression*

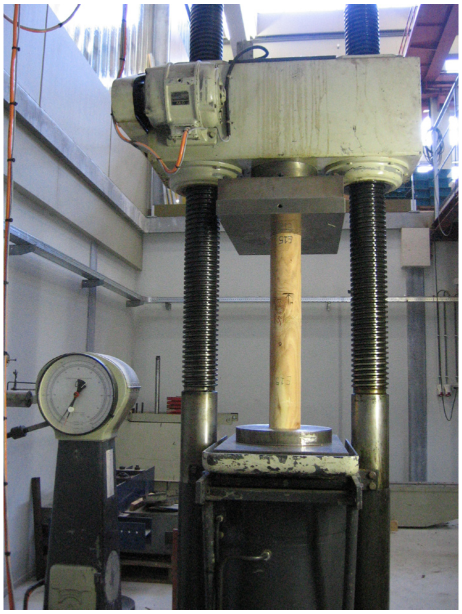

Figure 2.48 compression test

To see if the same relation between bending strength and compression strength applies for round wood as for sawn timber, also compression tests were done in accordance with NEN-EN 408 (figure 2.48). Of the specimen that have been tested in bending, sections of 1m length were cut from those parts that had not been damaged. The load was applied at such a speed that compression failure would occur at 300 ± 120 sec. The maximum force until failure was divided by the area of the specimen to obtain the maximum compression stress.

Table 2.19 shows the results, figure 2.49 shows a scatter diagram of the relation with the density at 12% moisture content.

The scatter diagram shows a slightly higher value for the correlation factor for the relation between density and compression strength than found at the bending tests.

Specimen E19 was loaded far beyond its failure point to show the failure mechanism more clearly (figure 2.50). From this it can be seen that, as with most specimen, the compression failure starts below a knot. The density of the knot is much higher than of the clear wood, causing this knot to push into the clear wood.

Table 2.19 compression strength

Nr [-]	fc0 [N/mm2]
E1	28,91
E2	30,39
E3	30,98
E4	36,07
E5	30,80
E6	28,76
E7	34,19
E8	32,35
E9	38,80
E10	31,80
E11	32,29
E12	32,56
E13	30,15
E14	29,39
E15	29,60
E16	31,39
E17	37,04
E18	29,33
E19	34,01
E20	37,17

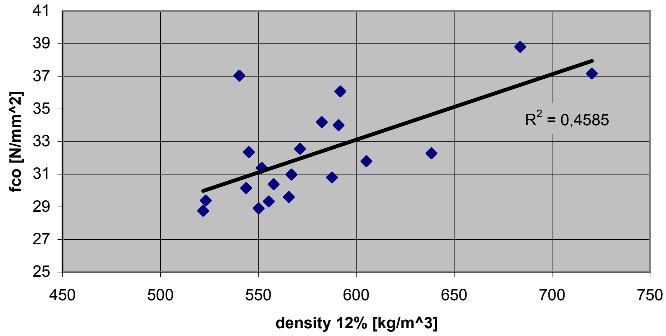

Figure 2.49 correlation f_{co} and density

Figure 2.50 compression failure specimen E19

2.3.4 *Analysis*

Table 2.20 shows all the relations between the characteristics and strength parameters of the specimen. What can be seen, is that the MOE obtained by the timber grader has a very good correlation with almost all of the other parameters. Only on the relation with the bending strength or modulus of rupture (MOR), the density shows a better value. From these results it can be concluded, that ring width shows almost no relation with any of the other parameters, the knot ratio only shows some relation with the $MOE_{stat\ global}$ and the timber grader is a very good device to predict the strength of timber.

Table 2.20 correlation factors strength parameters Smilde

Series Smilde	fco	fm	density	MOE_{dyn}	$MOE_{stat\ global}$	$MOE_{stat\ local}$	$MOE_{stat\ timber\ grader}$	knot ratio	ring width
fco	1,00								
MOR	0,29	1,00							
density	0,46	0,52	1,00						
MOE_{dyn}	0,79	0,33	0,50	1,00					
$MOE_{stat\ global}$	0,70	0,18	0,33	0,88	1,00				
$MOE_{stat\ local}$	0,70	0,23	0,23	0,82	0,77	1,00			
$MOE_{stat\ timber\ grader}$	0,78	0,34	0,54	0,98	0,87	0,79	1,00		
knot ratio*Kknot	0,20	0,12	0,07	0,11	0,31	0,08	0,13	1,00	
ring width	0,07	0,06	0,01	0,04	0,04	0,05	0,05	0,00	1,00

Compared to data obtained by previous tests done for the CONIFERS-project these correlation coefficients show big differences.
Especially the relations between the bending strength MOR and the different MOE-values is much lower

Table 2.21 correlation factors strengt parameters CONIFERS

Series CONIFERS	fm	density	MOE_{dyn}	$MOE_{stat\ global}$	$MOE_{stat\ local}$	knot ratio	ring width
MOR	1						
density	0,65	1					
MOE_{dyn}	0,76	0,75	1				
$MOE_{stat\ global}$	0,76	0,66	0,85	1			
$MOE_{stat\ local}$	0,72	0,64	0,82	0,91	1		
knot ratio	0,64	0,45	0,61	0,56	0,53	1	
ring width	0,56	0,34	0,52	0,52	0,43	0,55	1

for this series from Smilde than from the previous series. And in general, the other parameters show much higher correlation coefficients. An explanation could be that, although specified differently, for the series from Smilde topwood was used, which is much more branched. This results in many more knots and might also have an effect on other characteristics. An other explanation could be that, as suggested by ing. Z. van Olst MBA from "Staatsbosbeheer", the Smilde series came from a plot that was planted after the storm of 1979. These trees grew very fast and had a relatively high knot ratio. Although the specified plot and the area around it was not planted after 1979, some plots which were planted after 1979 can be found in the Smilde area (Appendix A3), so this possibility has to be considered.
To be able to make more definitive conclusions from the next series that are to be tested, these series will not consist of any topwood.

Table 2.22 results bending tests and Timber Grader

	Bending tests		Timber Grader	
Nr [-]	MOE local [N/mm2]	Class [-]	MOE static at 12% mc [N/mm2]	Class [-]
E1	7402	C24	8170	C18
E2	7781	C24	9456	C24
E3	8533	C30	9825	C24
E4	9630	C40	11617	C30
E5	9041	C35	10590	C30
E6	6481	C22	8242	C18
E7	9477	C40	11034	C30
E8	9265	C35	10112	C24
E9	9804	C40	12599	C35
E10	9322	C35	10536	C30
E11	8470	C30	11855	C35
E12	8773	C35	10473	C24
E13	8774	C35	9238	C24
E14	8232	C30	9599	C24
E15	8281	C30	10289	C24
E16	8453	C30	10252	C24
E17	11029	C30	12622	C30
E18	8799	C35	10316	C24
E19	9473	C40	11317	C30
E20	11364	C40	14001	C35

Table 2.22 shows the results from the bending tests and the Timber Grader to see to what extend the predicted values by the Timber Grader correspond to the “real” values from the bending tests. It can be seen that, although the MOE-values from the Timber Grader are all higher than the values from the bending tests, the predicted classes are all but one lower or equal to those calculated from the bending tests. As was shown before, the correlation between the MOE values of the Timber Grader and the bending tests is very high. The higher values are probably caused by other relations between density and dynamic or static MOE of round wood compared to sawn timber, for which the Timber Grader was originally developed. This makes the Timber Grader easily adaptable for round wood and thus quite a good device to determine the strength class of a piece of wood.

In EN 338, the three parameters that are used for the class definitions MOR, MOE and density (table 2.23), are also used to determine other parameters for sawn timber such as compression strength, tension strength etc.

Table 2.23 strength classes by EN 338 for sawn timber

Class	**C14**	**C16**	**C18**	**C22**	**C24**	**C27**	**C30**	**C35**	**C40**
MOR_k [N/mm²]	14	16	18	22	24	27	30	35	40
$MOE_{0,05}$ [N/mm²]	4700	5400	6000	6700	7400	8000	8000	8700	9400
r_k [kg/m³]	290	310	320	340	350	370	380	400	420

For the Smilde series, the compression strength has also been determined. To see if the same relation applies for round wood as the one set for sawn timber, figure 2.51 shows the relation between the compression and bending strength

The orange lines represent the relation as set in EN 338, the yellow squares are the values found in the tests. For the relation between compression and bending strength, an exact formula is known from EN 338:

$$f_{c,o} = 5(f_m)^{0,45}$$

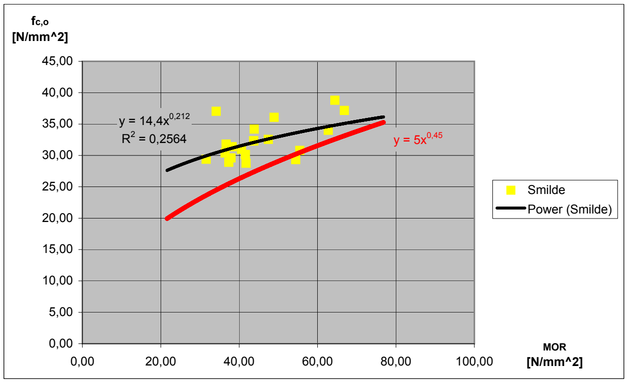

Figure 2.51 relation MOR - $f_{c,0}$ Smilde

For the Smilde series, the compression strength appears to be higher than predicted by the relation for sawn timber. When a regression line is drawn through the data from the Smilde series, higher compression strengths are predicted for low bending strength values. It must be noted however, that the number of available data is limited and thus the correlation coefficient for this regression line is low.

2.4 Visual Grading

In the CONIFERS-project, a visual grading system was developed to be able to predict to a certain extent the strength characteristics of a round wood specimen. The selection criteria consist of the knot ratio and the average ring width. If the combination of ring width (RW) and knot ratio (KR) of a series of specimen is below the line RW=0,8/KR, with a maximum ring width of 4mm and a maximum knot ratio of 0,35, the series can be put into strength class C40 (figure 2.52).

To confirm its validity, this grading system was also applied to the 20 specimen from "Smilde". Figure 2.52 and table 2.25 show the results from all the data from the CONIFERS-project and of the 20 specimen from "Smilde".

The procedure is as follows: first, a selection is made from each series of specimen as described by the criterion. So for example for the series with a specimen diameter of 120 mm, 2 specimen are excluded. In Figure 2.52, this shows by the two yellow squares that fall outside the red line, which is the criterion. In table 2.25, this is shown by the count in\count out column. For the 120 series, 52 comply with the criterion and 2 are excluded.
Secondly, of each series, the ranked 5% values for bending strength (MOR) and MOE,the mean values for MOE and the 5% values for density of those specimen that comply with the criterion is determined. These values are checked for the strength classes according to EN 338 (table 2.24). The minimum value of these classes determines the final class definition of the series.

Table 2.24 strength classes by EN 338 for sawn timber

	C14	C16	C18	C22	C24	C27	C30	C35	C40
in N/mm²									
MOR_{05}	14	16	18	22	24	27	30	35	40
in kN/mm²									
$MOE_{0,mean}$	7	8	9	10	11	12	12	13	14
$MOE_{0,05}$	4,7	5,4	6,0	6,7	7,4	8,0	8,0	8,7	9,4
in kg/m³									
r_k	290	310	320	340	350	370	380	400	420

Also, according to EN 384 some reduction parameters were used to correct for sample size. The MOE value per series is calculated by:

$$\overline{MOE} = \left[\frac{\sum MOE_i}{n} \right]$$

in which MOE_i is the value for MOE of the individual specimen and n is the sample size in the criterion.
In table 2.25, this value is 13602 N/mm² for series 100.
From this, the mean value for all the series is calculated by:

$$MOE_{0,mean} = \frac{\sum \overline{MOE}_j n_j}{\sum n_j}$$

in which $\overline{MOE}_j$ is the mean MOE value per series and n_j is the sample size per series.
In table 2.25, this value is 14089 N/mm² for the total series.

The MOR value for all the series is determined by:

$$MOR_k = \overline{MOR_{05}} k_s$$

$$\overline{MOR_{05}} = \frac{\sum MOR_{05} n}{\sum n}$$

in which n is the sample size in the criterion and MOR_{05} is the ranked value of MOR per series. The factor k_s is dependent on the sample size and determined by a graph in EN 338. The value for $\overline{MOR}_{05}$ has a lower limit of the minimum value of MOR_{05} times 1,2. Since no influence of specimen diameter on strength characteristics was found in the CONIFERS project, the factor k_v is set to unity.
In table 2.25, the value for $\overline{MOR}_{05}$ is 61 N/mm², the minimum is 47 N/mm², k_s is 0,95 and MOR_k is 45 N/mm². This value is checked for the 5% value in the strength class table from EN 338.

The density value is determined by:

$$\rho_{05} = \left(\overline{\rho} - 1,65 s\right)$$

$$\rho_k = \frac{\sum \rho_{05,j} n_j}{\sum n_j}$$

in which $\overline{\rho}$ is the average density value for the specimen that comply with the criterion and s is the standard deviation of these specimen. The value for ρ_k is the weighed value of ρ_{05} for all series. In table 2.25, the value for ρ_{05} for the 100-series is 584 kg/m³, the value for ρ_k is 585 kg/m³.

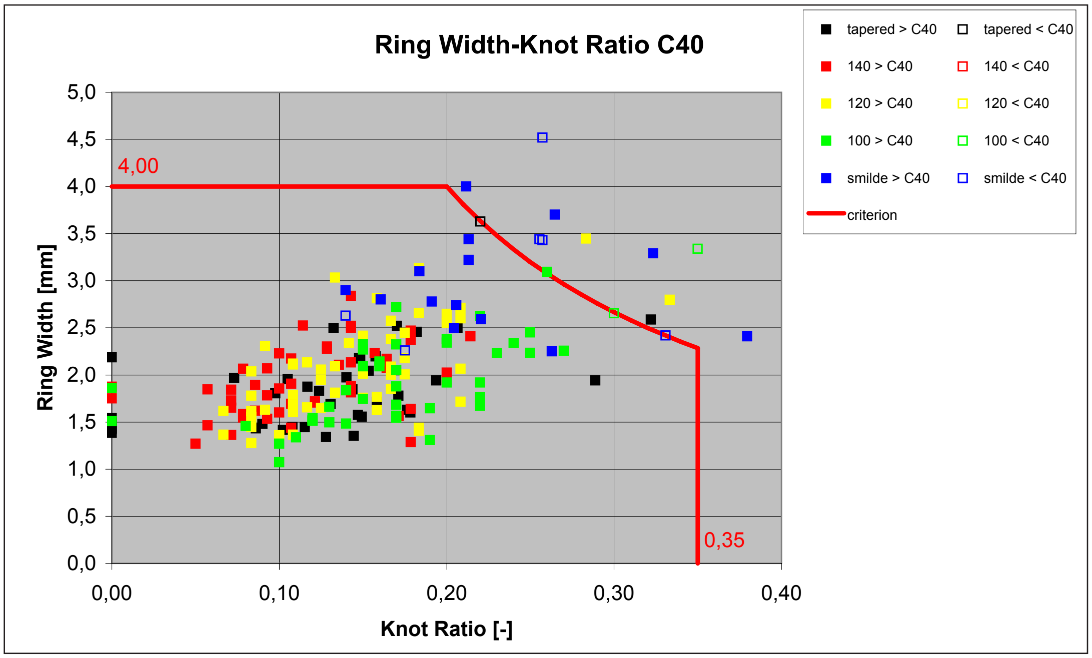

Figure 2.52 selection criterion CONIFERS

In figure 2.52, the individual specimen that have strength characteristics below C40 are shown with open squares, those equal to or higher than C40 are shown with closed squares. The figure shows that most of the specimen that have strength and elasticity values below C40 are outside the selection criteria. Only two specimen are inside the criteria and have values below C40. This is why the 5%-value of this series is low. It must be noted, that the results of one of these specimen are questionable (as was shown in chapter 2.3.1), because of startup- irregularities and thus low R-squared values during testing. But even when this value is ignored, still the 5%-value is much lower than C40.

Because this original criterion does not hold for the Smilde series and because the relation of growth ring width and strenght properties was found to be very weak, it is decided to look for an additional selection criterion.

Table 2.25 parameter values data series

series	MOE_{05}	$\overline{MOE}$	MOR_{05}	ρ_{05}	Class	count in / count out
100	9617	13602	60	584		42
class	**40**	**35**	**40**	**40**	**35**	**2**
120	11350	14478	62	591		52
class	**40**	**40**	**40**	**40**	**40**	**2**
140	10191	15042	63	591		48
class	**40**	**40**	**40**	**40**	**40**	**0**
tapered	9533	14076	63	574		21
class	**40**	**40**	**40**	**40**	**40**	**1**
smilde	6679	10321	39	560		12
class	**18**	**22**	**35**	**40**	**18**	**8**
all	9980	14088	57	584		192
class	**40**	**40**	**40**	**40**	**40**	**13**
$\overline{MOR}_{05}$			61			
$\min(MOR_{05})*1,2$			47			
$\overline{MOR}_{05}$			47			
k_s			0,95			
		$MOE_{0,mean}$	**MOR_k**	**ρ_k**	**Class**	
combination		14089	45	585		
class		**40**	**40**	**40**	**40**	

Before a new crtiterion is determined, first the original criterium must be analysed to see why it does not hold for all specimen.

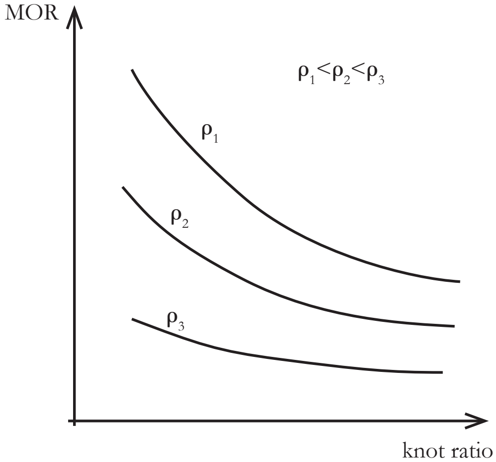

Figure 2.53 influence knot ratio on bending strength

First, as was shown in the regression analysis, the ring width showed a very low relationship with any strength parameter. Secondly, as is known from sawn timber, the influence of the knot ratio on the characteristic bending strength gets higher with lower density values (figure 2.53). Since the knot ratios of the CONIFERS specimen were very low, this effect was not shown, but this does apply for the Smilde series.
From this it is decided to look for a selection criterion with the knot ratio and the density as parameters. Also, these parameters are both relatively easy to determine, as opposed to the average ring width.
For several strength classes, a criterion is determined by the same procedure as described for the CONIFERS criterion. The limits of the knot ratio and density values are stretched to the point where one of the values of MOE, MOR or density no longer correspond to the desired strength class.

Both the knot size and the knot ratio are tested as a characterisation parameter to see if there is a certain relationship with the dimensions of the specimen.

First, a criterium is determined for strength class C40.
Data from the determination of the strength values can be found in Appendix A7.
As shown in figure 2.54, the maximum values for density and knot ratio can be set to 570 kg/m^3 and 0,15, respectively. With these limits, all of the specimen from the "Smilde" series would be rejected. The individual specimen close to the limits that would be put in strength class C40 individually based on the characteristic value, would as a group fall out of this strength class based on the mean value.
For the maximum knot size, the limit is 40 mm (figure 2.55).

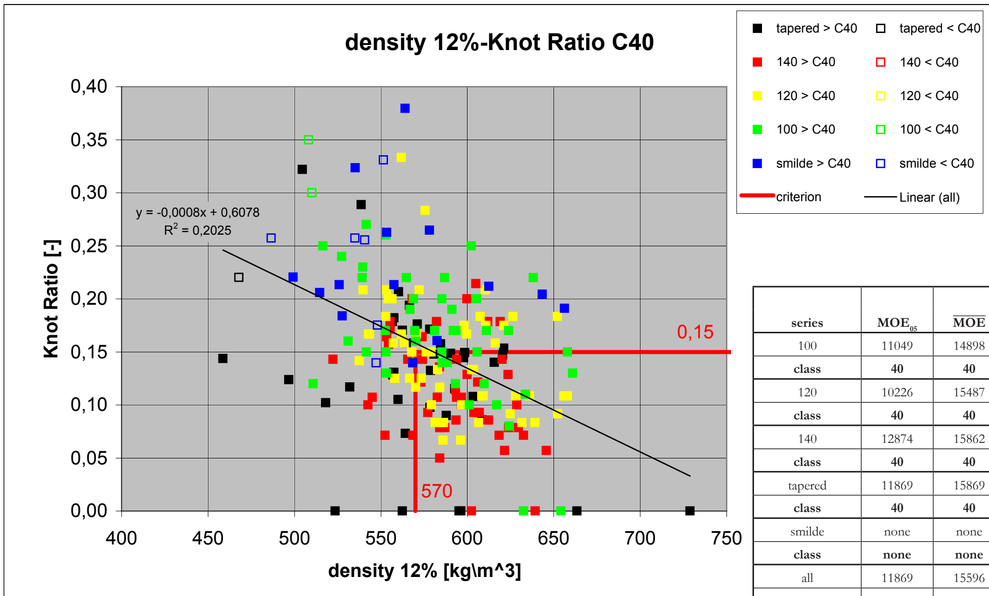

series	MOE_{05}	$\overline{MOE}$	MOR_{05}	ρ_{05}	Class	count in / count out
100	11049	14898	68	574		14
class	**40**	**40**	**40**	**40**	**40**	**30**
120	10226	15487	66	560		26
class	**40**	**40**	**40**	**40**	**40**	**28**
140	12874	15862	71	569		31
class	**40**	**40**	**40**	**40**	**40**	**17**
tapered	11869	15869	76	546		16
class	**40**	**40**	**40**	**40**	**40**	**23**
smilde	none	none	none	0		0
class	**none**	**none**	**none**	**none**	**none**	**20**
all	11869	15596	71	562		87
class	**40**	**40**	**40**	**40**	**40**	**118**
$\overline{MOR}_{05}$			70			
$\min(MOR_{05})*1,2$			79			
$\overline{MOR}_{05}$			70			
k_s			0,95			
		$MOE_{0,mean}$	**MOR_k**	ρ_k	**Class**	
combination		15596	66	563		
class		**40**	**40**	**40**	**40**	

Figure 2.54 selection criterion C40 density-knot ratio

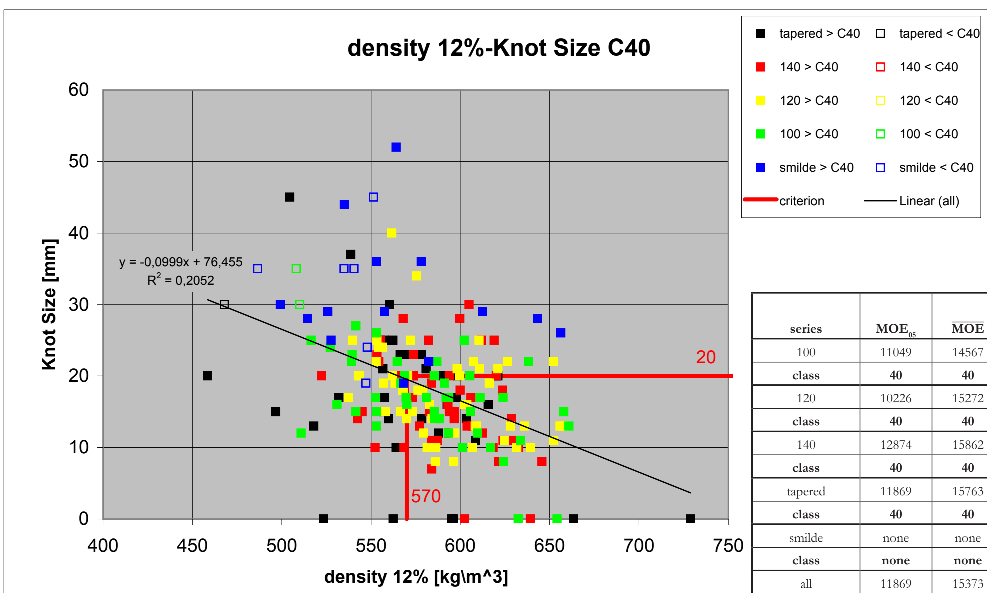

series	MOE_{05}	$\overline{MOE}$	MOR_{05}	ρ_{05}	Class	count in / count out
100	11049	14567	64	567		23
class	**40**	**40**	**40**	**40**	**40**	**21**
120	10226	15272	66	560		29
class	**40**	**40**	**40**	**40**	**40**	**25**
140	12874	15862	71	569		31
class	**40**	**40**	**40**	**40**	**40**	**17**
tapered	11869	15763	76	549		16
class	**40**	**40**	**40**	**40**	**40**	**23**
smilde	none	none	none	0		0
class	**none**	**none**	**none**	**none**	**none**	**20**
all	11869	15373	70	562		99
class	**40**	**40**	**40**	**40**	**40**	**106**
$\overline{MOR}_{05}$			69			
$\min(MOR_{05})*1,2$			77			
$\overline{MOR}_{05}$			69			
k_s			0,95			
		$MOE_{0,mean}$	**MOR_k**	ρ_k	**Class**	
combination		15373	65	563		
class		**40**	**40**	**40**	**40**	

Figure 2.55 selection criterion C40 density-knot size

Next, a criterium is determined for strength class C35

For this strength class, the density and knot limits can not be stretched further than for class C40. When the limits are stretched any further, the “Smilde” series would cause the strength class to fall back to a maximum of C24 (figures 2.55 and 2.56).

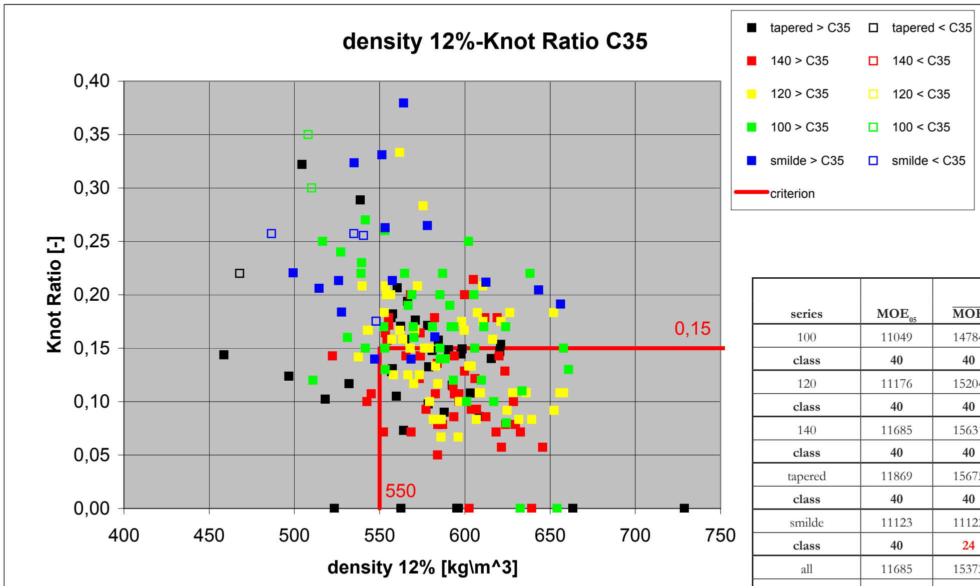

series	MOE_{05}	$\overline{MOE}$	MOR_{05}	ρ_{05}	Class	count in / count out
100	11049	14784	68	555		16
class	**40**	**40**	**40**	**40**	**40**	**28**
120	11176	15204	65	552		30
class	**40**	**40**	**40**	**40**	**40**	**24**
140	11685	15631	71	562		34
class	**40**	**40**	**40**	**40**	**40**	**14**
tapered	11869	15675	76	532		21
class	**40**	**40**	**40**	**40**	**40**	**18**
smilde	11123	11123	57	568		1
class	**40**	**24**	**40**	**40**	**24**	**19**
all	11685	15373	70	551		102
class	**40**	**40**	**40**	**40**	**40**	**103**
$\overline{MOR}_{05}$			88			
$\min(MOR_{05})*1,2$			68			
$\overline{MOR}_{05}$			68			
k_s			0,95			
		$MOE_{0,mean}$	MOR_k	ρ_k	Class	
combination		15373	64	552		
class		**40**	**40**	**40**	**40**	

Figure 2.56 selection criterion C35 density-knot ratio

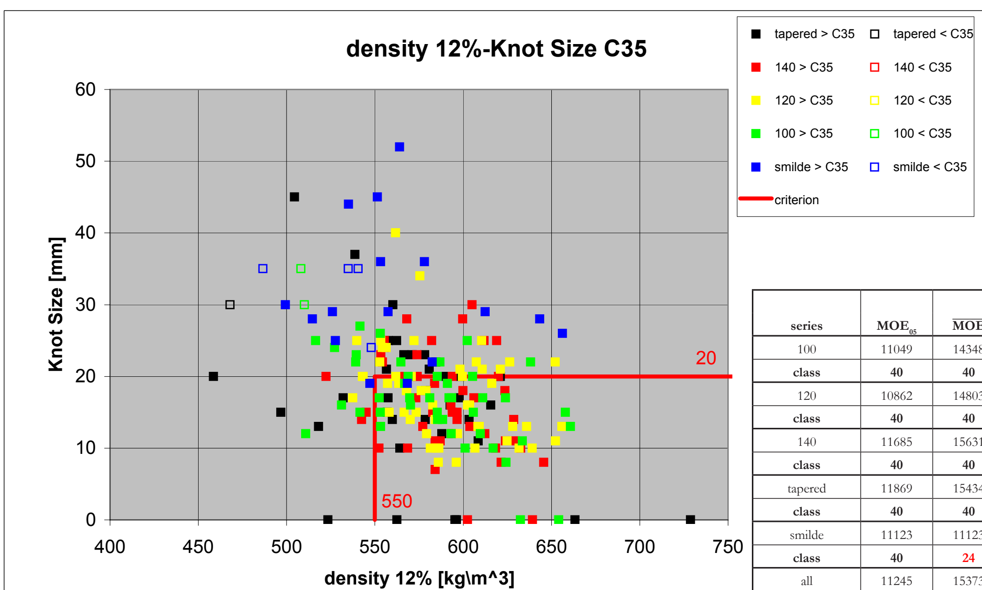

series	MOE_{05}	$\overline{MOE}$	MOR_{05}	ρ_{05}	Class	count in / count out
100	11049	14348	64	549		29
class	**40**	**40**	**40**	**40**	**40**	**15**
120	10862	14803	64	548		36
class	**40**	**40**	**40**	**40**	**40**	**18**
140	11685	15631	71	562		34
class	**40**	**40**	**40**	**40**	**40**	**14**
tapered	11869	15434	76	533		22
class	**40**	**40**	**40**	**40**	**40**	**17**
smilde	11123	11123	57	568		1
class	**40**	**24**	**40**	**40**	**24**	**19**
all	11245	15373	66	549		122
class	**40**	**40**	**40**	**40**	**40**	**83**
$\overline{MOR}_{05}$			68			
$\min(MOR_{05})*1,2$			68			
$\overline{MOR}_{05}$			68			
k_s			0,95			
		$MOE_{0,mean}$	MOR_k	ρ_k	Class	
combination		14918	64	550		
class		**40**	**40**	**40**	**40**	

Figure 2.57 selection criterion C35 density-knot size

As was seen in the criterion selection for strength class C35, including any of the specimen from the Smilde series would cause the dataset to fall back to strength class C24. Therefore, the criteria for C35 and C30 are not determined, and only a citerion for strength class C24 is presented. Here, the limits can be stretched to 550 kg/m³ for density and 0.20 for knot ratio. The knot size can not be stretched any further.

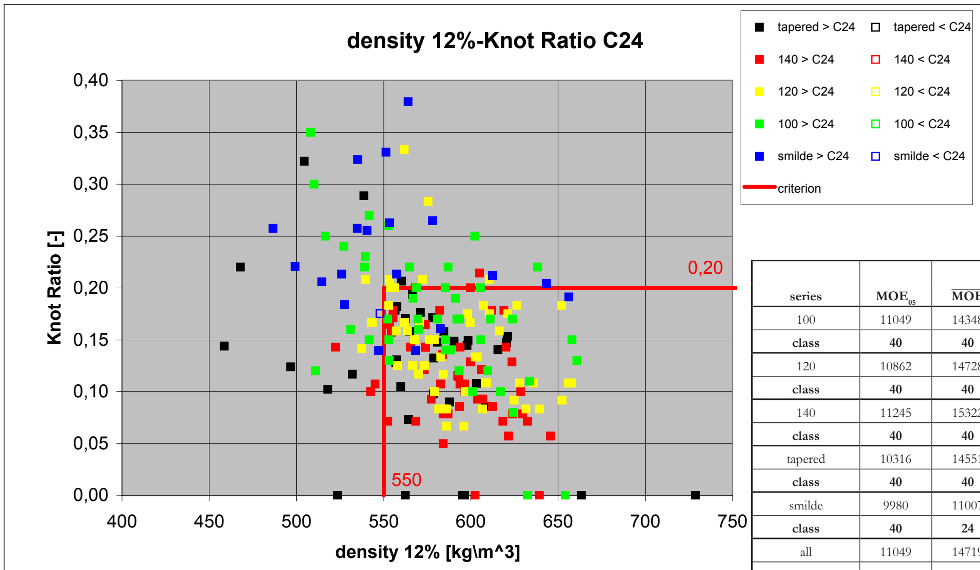

						count in
series	MOE_{05}	$\overline{MOE}$	MOR_{05}	ρ_{05}	Class	count out
100	11049	14348	64	549		29
class	**40**	**40**	**40**	**40**	**40**	**15**
120	10862	14728	62	547		45
class	**40**	**40**	**40**	**40**	**40**	**9**
140	11245	15322	65	553		44
class	**40**	**40**	**40**	**40**	**40**	**4**
tapered	10316	14551	69	531		30
class	**40**	**40**	**40**	**40**	**40**	**9**
smilde	9980	11007	54	525		3
class	**40**	**24**	**40**	**40**	**24**	**17**
all	11049	14719	65	546		151
class	**40**	**40**	**40**	**40**	**40**	**54**
$\overline{MOR}_{05}$			77			
$\min(MOR_{05})*1,2$			65			
$\overline{MOR}_{05}$			65			
k_s			0,95			
		$MOE_{0,mean}$	MOR_k	ρ_k	Class	
combination		14501	62	546		
class		**40**	**40**	**40**	**40**	

Figure 2.58 selection criterion C24 density-knot ratio

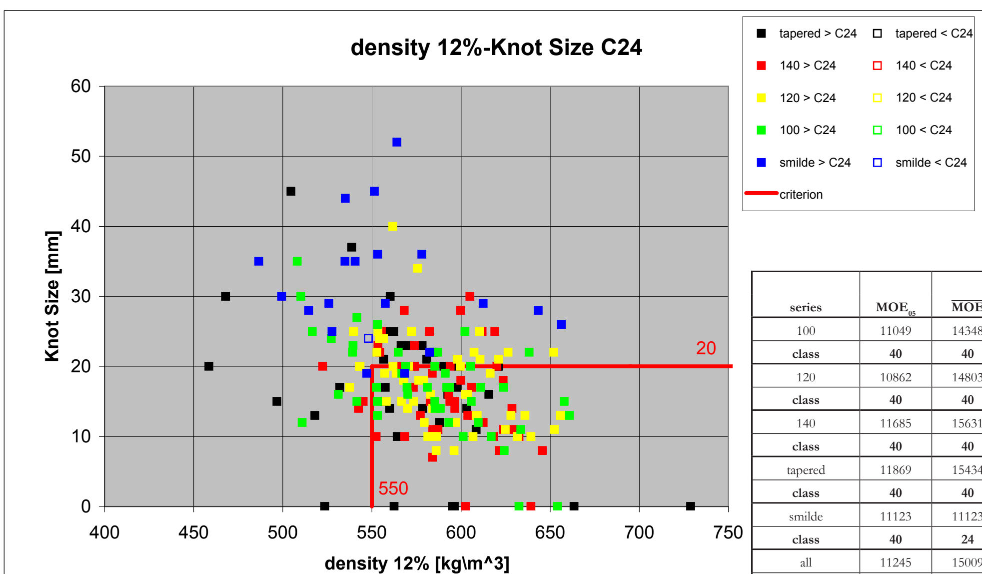

						count in
series	MOE_{05}	$\overline{MOE}$	MOR_{05}	ρ_{05}	Class	count out
100	11049	14348	64	549		29
class	**40**	**40**	**40**	**40**	**40**	**15**
120	10862	14803	64	548		36
class	**40**	**40**	**40**	**40**	**40**	**18**
140	11685	15631	71	562		34
class	**40**	**40**	**40**	**40**	**40**	**14**
tapered	11869	15434	76	533		22
class	**40**	**40**	**40**	**40**	**40**	**17**
smilde	11123	11123	57	568		1
class	**40**	**24**	**40**	**40**	**24**	**19**
all	11245	15009	66	549		122
class	**40**	**40**	**40**	**40**	**40**	**83**
$\overline{MOR}_{05}$			68			
$\min(MOR_{05})*1,2$			68			
$\overline{MOR}_{05}$			68			
k_s			0,95			
		$MOE_{0,mean}$	MOR_k	ρ_k	Class	
combination		14918	64	550		
class		**40**	**40**	**40**	**40**	

Figure 2.59 selection criterion C24 density-knot size

When the density limit is stretched further to 500kg/m^3, the strength class characteristics for class C24 can only be met when the maximum knot size is set to 30 mm and a curve is fitted between these limits as defined in figure 2.60. This is because of the single value for the smilde series just on the edge of this line that would cause the dataset to fall out of class C24 when included. Since this is not a practical selection criterion to use, this criterion will be disregarded. For the knot ratio, no solution can be found for density values lower than 550 kg/m^3.

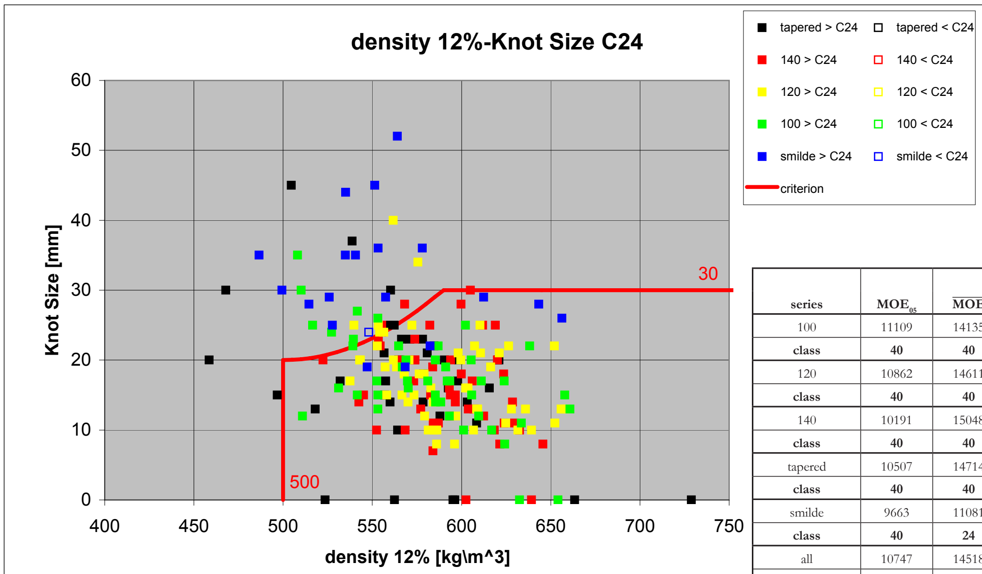

Figure 2.60 selection criterion C24 density-knot size

series	MOE_{05}	$\overline{MOE}$	MOR_{05}	ρ_{05}	Class	count in / count out
100	11109	14135	67	535		36
class	**40**	**40**	**40**	**40**	**40**	**8**
120	10862	14611	64	543		48
class	**40**	**40**	**40**	**40**	**40**	**6**
140	10191	15048	65	548		45
class	**40**	**40**	**40**	**40**	**40**	**3**
tapered	10507	14714	75	520		31
class	**40**	**40**	**40**	**40**	**40**	**8**
smilde	9663	11081	39	531		6
class	**40**	**24**	**35**	**40**	**24**	**14**
all	10747	14518	64	538		166
class	**40**	**40**	**40**	**40**	**40**	**39**
$\overline{MOR}_{05}$			65			
$\min(MOR_{05})*1,2$			47			
$\overline{MOR}_{05}$			47			
k_s			0,95			
		$MOE_{0,mean}$	**MOR_k**	**ρ_k**	**Class**	
combination		14117	45	538		
class		**40**	**40**	**40**	**40**	

The selection criteria for strength class C40 shows no sample size difference between knot ratio and knot size. Since the knot size is easier to determine than the knot ratio, this criterium is used. For strength class C40, the limits can be set to 570 kg/m^3 for density and 20 mm for knot size. For C35 and C30, no other limit values can be found, because changing of any of the limits would cause the Smilde series to fall back to strength class C24. For this strength class, the limits are 550 kg/m^3 for density and 0,20 for knot ratio. The knot size can not be stretched further than the value found for strength class C40 (20 mm).

During investigation of the classification limits it was found, that the critical values for the strength classes were the $\overline{MOE}_{mean}$ values for the "Smilde" series. The values for bending and compression strength would place the series in a much higher strength class. In table 2.26, the class definition for the whole Smilde series is shown. The high variation in strength class between the different parameters suggests a different strength class definition for round wood.

Table 2.26 class definitions Smilde series

series	**MOE_{05}**	**$\overline{MOE}$**	**MOR_{05}**	**ρ_{05}**	**Class**
100	6679	9914	34,8	486	
class	**18**	**18**	**30**	**40**	**18**

2.5 Conclusion

The goal of this quality investigation was to find a relation between the location of larch forests and the expected mechanical properties of the wood. For this, the aspects that influence the growth of larch were translated in a Site-index or S-value, that describes the expected height of the thickest tree per are, independent of age. Also, the mechanical properties of larch wood from different locations in The Netherlands have been investigated. Figure 2.61 shows the results for the GIS-analysis and density tests for the three different areas.

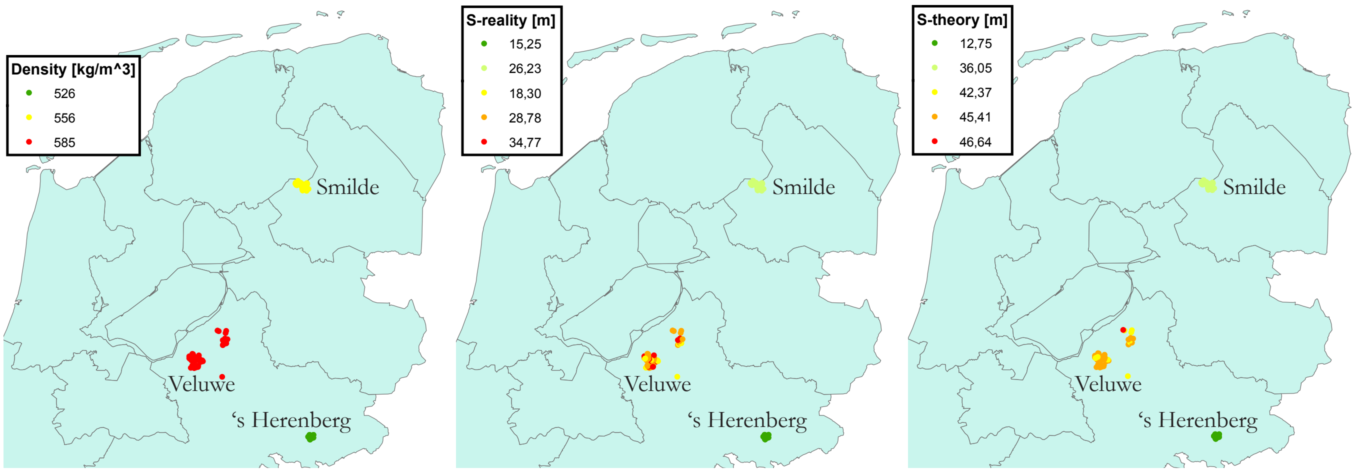

Figure 2.61 density and S-values all series

The exact origin of the CONIFERS series was not known, only that it came from somewhere in the "Veluwe". In this area, only three different S-values appear in plots owned by "Staatsbosbeheer". For the density, the average value for the whole series is taken. As was shown in chapter 2.2, the relation between the theoretical and real value for the Site-index is very weak. But the distribution of values is similar: low values for 's Herenberg, medium values for Smilde and the highest values in the area of the Veluwe. The density values for these plots show the same distribution. This implies a certain relation between the S-value for a certain plot and the density of a larch tree on this plot. In further experiments, with larch trees from other plots in The Netherlands, this relation can be investigated in further detail.

As a grading parameter, the density itself is not suitable for determining the strength of larch round wood. Together with the knot size or knot ratio, a selection criterion can be made for strenght classes C40 and C24 (figure 2.62).

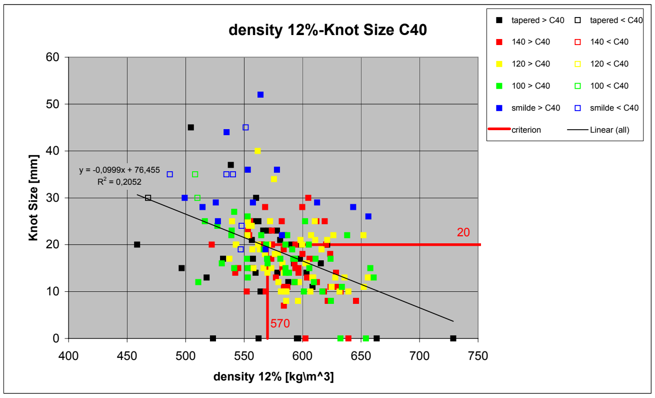

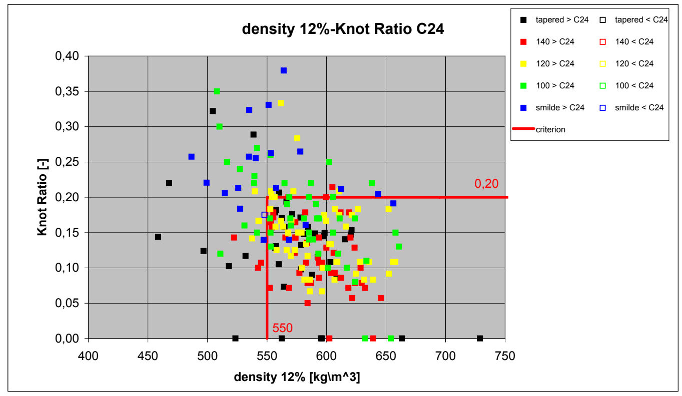

Figure 2.62 selection criteria limits C40 and C24

For strength class C40, all specimen from Smilde would fall outside the selection criterion. This complies with the lower density and S-values for this series compared to the CONIFERS series. This first study suggests that the strength of the CONIFERS series was exceptionally high and is probably not representative for homegrown larch.

Also, the relations between strength and stiffness parameters appear to be slightly different from the relations known and set by EN338 for sawn timber. More study on this subject could lead to a separate classification system for round wood and improve the use of round wood in constructions.

When the relation between the S-values and density is known after more tests have been done, the desired strength of larch round wood from The Netherlands can be obtained by simply ordering from a certain plot and checking for maximum knot size.

3 Viewing Platform

From the strength analysis it showed that the Modulus of Elasticity of the "Smilde"-series was much lower than that of all the other series from the CONIFERS-project. Also, the visual grading limits that were determined for these series (with the average year ring width and knot ratio as characterisation parameters) were used for the strength grading of the timber used for the viewing platform that was designed as a result of the CONIFERS project (figures 3.1 to 3.3). From this report, it can be suggested, that some of the timber used for this viewing platform is therefore much less stiff than expected.
In this chapter an analysis is made to determine wether this can have negative effects on the vibration and dispacements of the viewing platform. The analysis is done in the finite element structural analysis program GSA. It must be noted that the model used in this analysis is a simplification of the real situation and no quantitative conclusions can be drawn from its results. It is only intended to give insight in the force flows and variations in vibration and deformation from the reference situation.

Figure 3.1 viewing platform

Figure 3.2 beam element detail

Figure 3.3 connection detail

In the GSA program, the viewing platform is modelled in such detail as needed to give insight in the force flows and deformations (figure 3.4).

Table 3.1 shows some dimensions of the chosen model [De Vries,2000a].

Table 3.1 viewing platform dimensions

H	n	k/n	R	S	levels	height between levels [m]					
[m]	#	[-]	[m]	[-]	#	1	2	3	4	5	6
19	12	0.5	3.7	5.1	6	4.0	3.0	2.6	2.6	3.0	4.0

H = height of the structure
n = number of columns
k/n = factor for twist, $\varphi = k/n*\pi$
R = radius of top level
S = slenderness = H/R

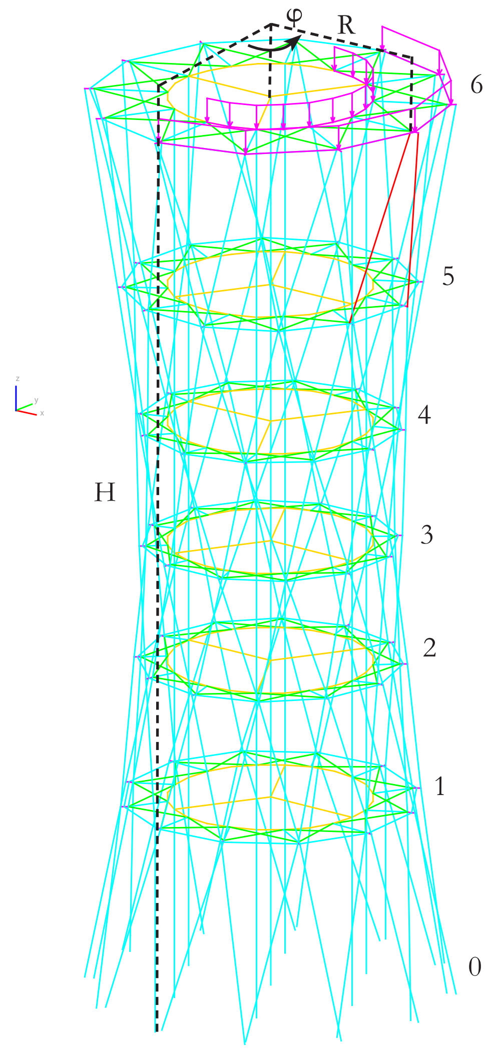

Figure 3.4 viewing platform model

The central staircase is not taken in the model, which does have influence on the stiffness of the structure. Therefore, the found relations are qualitative only and no conclusions can be drawn on the actual deformations of the built viewing platform. The central columns that support the different levels are included.

As in the built viewing platform, each level is stiffened in horizontal direction by steel cables to ensure all columns contribute to the stiffness under horizontal loads.

Also, as can be seen in figure 3.3 and in the model, the connections are excentric, causing extra moments in the joints.

Table 3.2 shows some dimensions of the used elements.

Table 3.2 dimensions of used elements

Element	Material	Dimensions	Unit	Color
columns	round wood	Ø 120	mm	blue\red
A-frames	sawn timber C24	200*100	mm	yellow
steel cables	steel S1180	Ø 10	mm	green
connections	steel S360	10*10*0,2	mm	purple

3.1 Vibration

Because the vibration of a structure is dependent on its stiffness parameters, the presence of less stiff elements could have negative effect on the eigenfrequency of the viewing platform. This could lead to dangerous situations, when the eigenfrequency is in the same range as the vibration induced by a semi-full loaded top platform by persons.
Previous study showed the eigenfrequency is a function of the shear modulus of the top section and the height of the structure [De Vries,2000a]:

$$f_e = \frac{1}{4}\sqrt{\frac{GA}{\mu H^2}}$$

in which μ is the mass per height of the structure and GA is the shear stiffness of the top section.
From this the maximum allowable deformation can be expressed as a function of the maximum acceleration of the top. Previous calculations on the structure showed an eigenfrequency in the range of 1 to 5 Hz. In this range, the maximum allowable accelerations were set to be around 0,5 m/sec^2 [De Vries, 2000a].
So the maximum allowable deformation at the top will be:

$$u_{\max} = \frac{0,5}{(2\pi f_e)^2}$$

In the range of 1 to 5 Hz this value is between 0,5 to 12,7 mm.

fe	umax
1	12,7
2	3,2
3	1,4
4	0,8
5	0,5

3.2 Displacements

To show the influence of the presence of less stiff elements in the viewing platform the situation of a semi-full loaded top platform is analysed (figure 3.4). This is done, because this might lead to dangerous situations in deformation or vibration. The load is set arbitrarily to 2,5 kN/m², which corresponds to roughly 3 persons of 80 kg per square meter.
Two types of round wood columns are used (table 3.3):

Table 3.3 dimensions of used elements

Type	MOE [N/mm²]	MOR [N/mm²]	density [kg/m³]	Fmax [kN]	Mmax [kNm]	Color
strong	10000	24	450	271	4,1	blue
weak	7000	18	350	204	3,1	red

The values for the axial force (F_{max}) and moment (M_{max}) capacity are determined by:
F_{max} = A/MOR
M_{max} = MOR*W_z

The analysis is done for 6 different situations:

- The standard reference situation with all strong elements
- The situation with one weak element at the top on the edge of the load.
- The situation with two weak elements at the top on the edge of the load
- The situation with a line of weak elements from the top to the ground on the edge of the load
- The situation in which an element is completely missing at the top on the edge of the load
- The situation with all weak elements

In the figures, weak elements are shown in red, standard alements in blue.
In the tables, the results for the deformation and the eigenfrequencies are given. Figures 3.5 and 3.6 show the node and element numbers that are given in the results. Only the two elements directly below and on the edge of the loaded area are analysed for practical reasons.

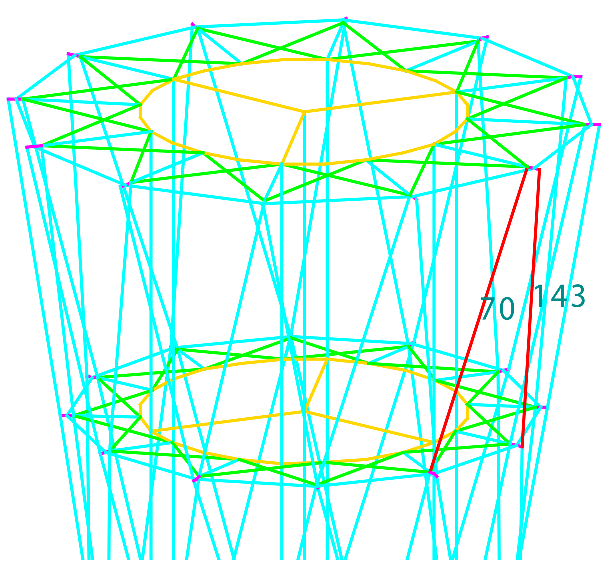

Figure 3.5 element numbers

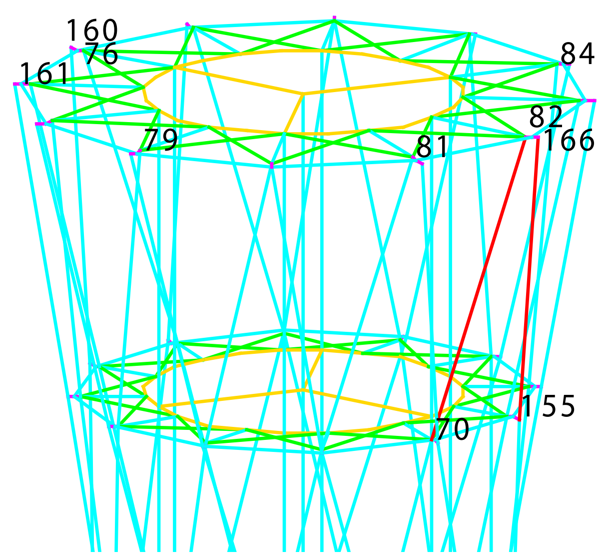

Figure 3.6 node numbers

The eigenfrequencies are given in 5 modes. Mode 1 and 2 are deformations of the top in 2 perpendicular directions (figure 3.7), mode 3 is a torsional deformation (figure 3.8). Modes 4 and 5 are double-curved deformations in two perpendicular diections (figure 3.9). If 2 modes in perpendicular directions are equal, only one is given.
The deformations are expressed in maximum nodal deformations. The percentage values give the variation with the standard reference situation.

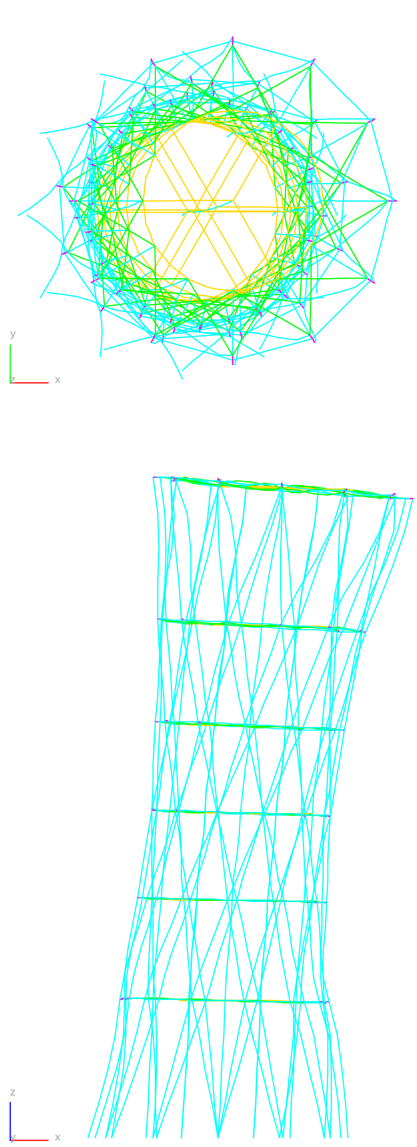

Figure 3.7 vibration mode 1 and 2

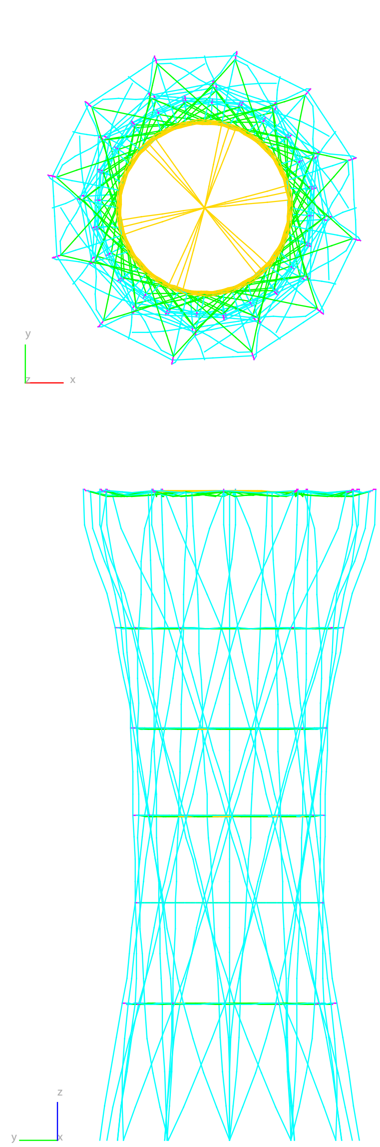

Figure 3.8 vibration mode 3

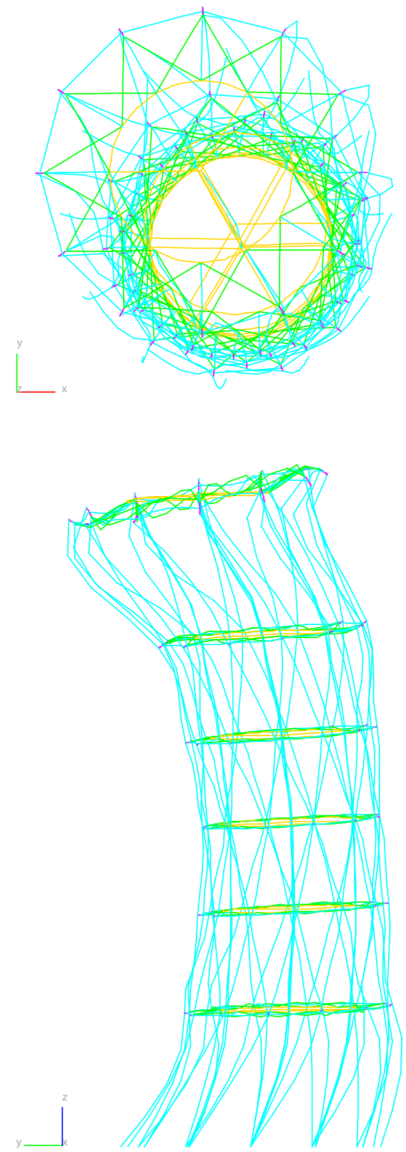

Figure 3.9 vibration mode 4 and 5

3.3 GSA Analysis

3.3.1 Standard reference situation

In this situation no weak elements are present. This situation is analysed as a reference situation to compare the other results with and thus all percentage values are set to 100%.

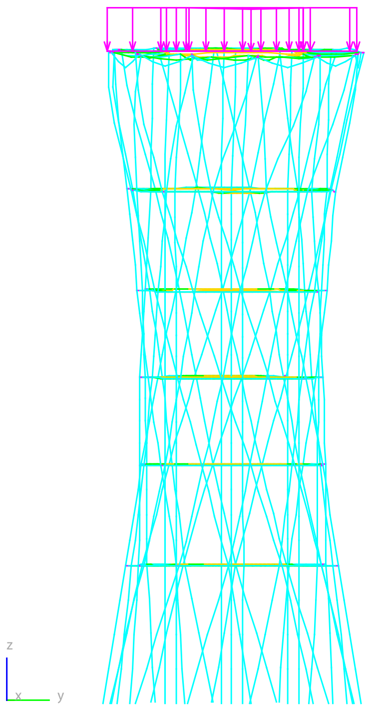

Figure 3.10 front view reference

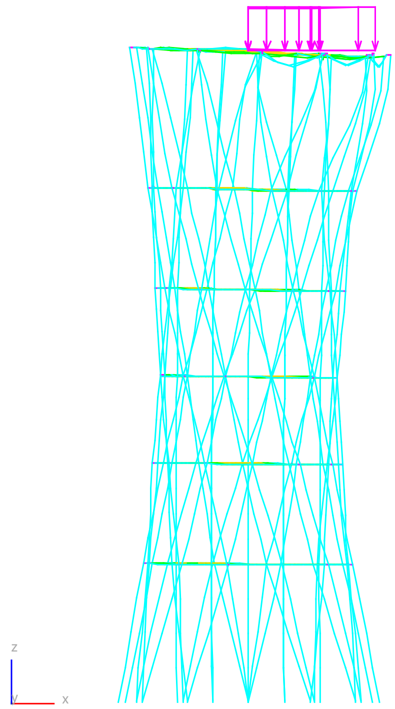

Figure 3.11 side view reference

Table 3.4 eiegnfrequencies reference

Mode	Frequency [Hz]	Period [s]	%
1	0,192	5,203	100%
3	0,301	3,314	100%
4	0,373	2,675	100%

Table 3.5 axial forces reference

Elem	Pos	Fx [kN]	%
70	70	-1,169	100%
	82	-1,169	100%
143	155	-2,601	100%
	166	-2,601	100%

Eigenfrequencies (table 3.4):
The lowest eigenfrequency is caused by mode 1. The period of this mode is 5,2 sec, which is too high to be caused by humans on the top level. But again, this value is for reference only.

Axial Forces (table 3.5):
The axial forces are twice as high in element nr 143 than in element nr 70. The reason for this is not clear at first sight, but is probably caused by the excentricity and stiffness of the connections and the deformation curve of the structure. Anyway, the axial forces are much lower than the capacity of the elements (around 0,5% to 1,0%, table 3.3)

Stresses (table 3.6):
As was already shown by the axial forces, the axial end bending stresses are very low. The shown percentage values are for the bending stresses.

Table 3.6 stresses reference

Elem	Pos	$\sigma_{c,0}$ [N/mm²]	σ_m [N/mm²]	%
70	70	-0,103	0,332	100%
	82	-0,103	-0,601	100%
143	155	-0,229	0,211	100%
	166	-0,229	-0,584	100%

Displacements (tables 3.7 to 3.8):
The maximum displacements are found at the top level, as would be expected. It can be seen that the other side of the top level, the displacement is upwards (node 161, figure 3.6), while the maximum displacement in x-direction is at node 79. This is because at this side, bending of the columns is perpendicular to the platform deformation direction. At node 82, for example, the column bends backwards, reducing the displacement in

Table 3.7 nodal displacements reference

Node	Ux	Uy	Uz	|U|	%
Maxima	[mm]	[mm]	[mm]	[mm]	
79	1,952	0,404	-0,291	2,015	100%
82	1,642	0,742	-0,903	2,016	100%
161	1,794	0,122	0,367	1,835	100%
81	1,803	0,683	-0,848	2,107	100%

x-direction (see also figure 3.12).
The displacement and deformation of the two element directly below the edge of the load area (nr 70 and 143, figure 3.5) is given in table 3.8. In figure 3.12, the deformation line with the node numbers is drawn. It can be seen, that some bending occurs in the columns. This is caused by the excentricity of the connections and is highly dependent on the dimensions of this connection element (figure 3.3).

Table 3.8 element displacements reference

Elem	Pos	Ux	Uy	Uz	|U|	%
		[mm]	[mm]	[mm]	[mm]	
70	70	0,562	-0,183	-0,416	0,723	100%
	25,00%	1,213	-0,079	-0,585	1,349	100%
	50,00%	1,921	0,204	-0,809	2,095	100%
	75,00%	2,22	0,526	-0,958	2,475	100%
	82	1,642	0,742	-0,903	2,016	100%
143	155	0,601	-0,189	-0,505	0,807	100%
	25,00%	1,225	-0,001	-0,618	1,372	100%
	50,00%	1,941	0,270	-0,736	2,094	100%
	75,00%	2,248	0,542	-0,778	2,44	100%
	166	1,642	0,731	-0,661	1,916	100%

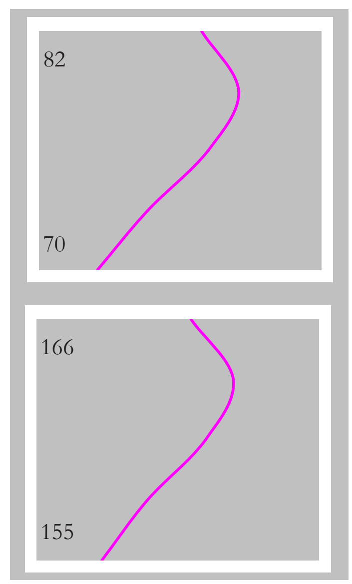

Figure 3.12 element deformation reference

3.3.2 One weak element

In this situation one weak element (nr 143) is present.

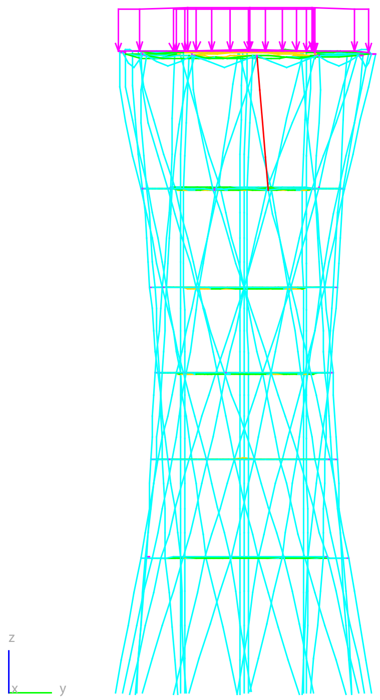

Figure 3.13 front view one weak element

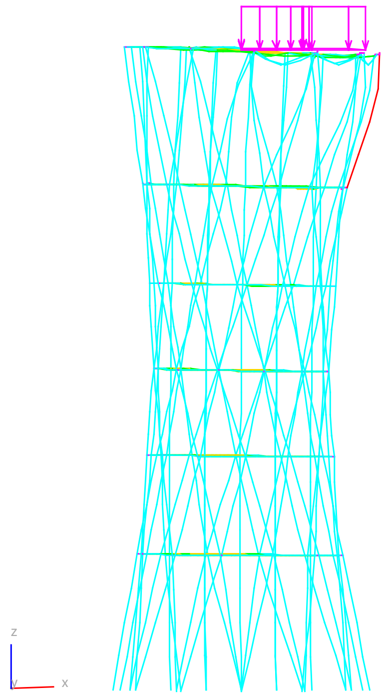

Figure 3.14 side view one weak element

Table 3.9 eigenfrequencies one weak element

Mode	Frequency [Hz]	Period [s]	%
1	0,192	5,204	100%
3	0,302	3,31	100%
4	0,373	2,68	100%

Table 3.10 axial forces one weak element

Elem	Pos	Fx [kN]	%
70	70	-1,337	114%
	82	-1,337	114%
143	155	-2,431	93%
	166	-2,431	93%

Eigenfrequencies (table 3.9):
The modes show no variation compared to the reference situation. From this it can be concluded, that the presence of one weak element does not influence the eigenfrequency of the viewing platform.

Axial forces (table 3.10):
It can be seen, that the stronger element takes up the force from the weaker element. Because the stiffness of the weaker element is lower, this element will deform more, causing the stronger element to be heavier loaded (redistribution of forces).

Stresses (table 3.11):
The axial and bending stresses are still very small, and the bending stress for the weak element nr 143 even reduces to 71% at the bottom node. The increase in bending stress for element 70 is limited.

Table 3.11 stresses one weak element

Elem	Pos	$\sigma_{c,0}$ [N/mm²]	σ_m [N/mm²]	%
70	70	-0,118	0,343	103%
	82	-0,118	-0,615	102%
143	155	-0,215	0,157	75%
	166	-0,215	-0,415	71%

Displacements (table 3.12 to 3.13):
The maximum displacements are almost identical to the reference situation. Also, the maximum values occur at the same nodes, so it can be concluded that this situation has no influence on the maximum displacements of the viewing platform.

Table 3.12 nodal displacements one weak element

Node	Ux	Uy	Uz	|U|	%
Maxima	[mm]	[mm]	[mm]	[mm]	
79	1,968	0,430	-0,289	2,035	101%
82	1,647	0,782	-0,926	2,045	101%
161	1,804	0,135	0,371	1,846	101%
81	1,813	0,718	-0,853	2,129	101%

In figure 3.15, the reference deformation line is drawn in pink, the deformation line of the current situation is drawn in purple. The displacements and deformations of elements 70 and 143 are again almost identical to the reference situation.

Table 3.13 element displacements one weak element

Elem	Pos	Ux	Uy	Uz	|U|	%
		[mm]	[mm]	[mm]	[mm]	
70	70	0,561	-0,182	-0,422	0,726	100%
	25,00%	1,21	-0,069	-0,594	1,35	100%
	50,00%	1,924	0,229	-0,824	2,106	101%
	75,00%	2,228	0,563	-0,979	2,498	101%
	82	1,647	0,781	-0,926	2,045	101%
143	155	0,598	-0,189	-0,496	0,800	99%
	25,00%	1,206	0,002	-0,614	1,353	99%
	50,00%	1,933	0,288	-0,740	2,09	100%
	75,00%	2,255	0,575	-0,791	2,458	101%
	166	1,647	0,768	-0,682	1,942	101%

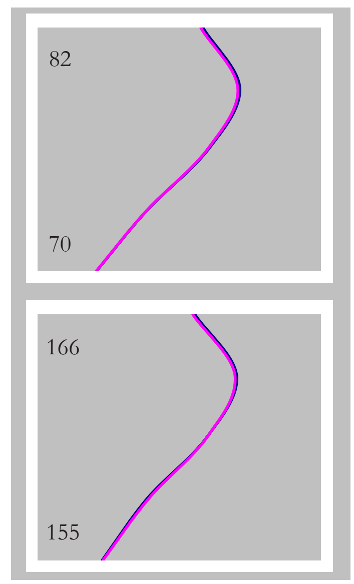

Figure 3.15 element deformation one weak element

This analysis shows, that the occurrence of one weak element directly below the edge of the load area does not lead to extra deformations of the structure. The forces are redistributed away from the weak element. Because the stresses in the elements are still well below the capacity values, this does not lead to dangerous situations.

3.3.3 Two weak elements

In this situation two weak elements (nr 70 and 143) are present.

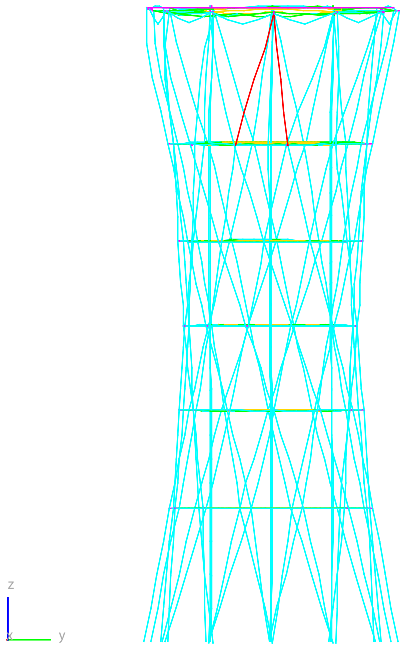

Figure 3.16 front view two weak elements

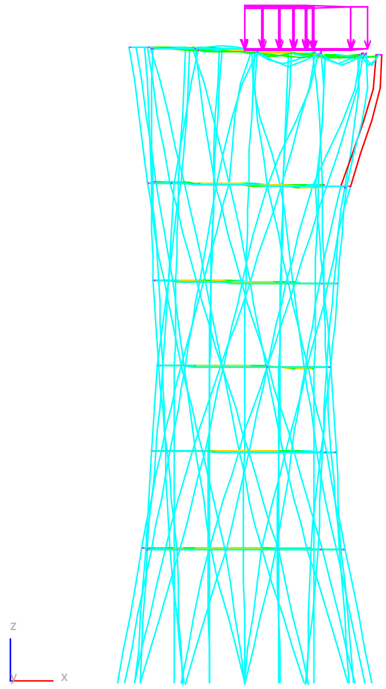

Figure 3.17 side view two weak elements

Table 3.14 eigenfrequencies two weak elements

Mode	Frequency [Hz]	Period [s]	%
1	0,192	5,204	100%
3	0,302	3,308	100%
4	0,372	2,686	100%

Table 3.15 axial forces two weak elements

Elem	Pos	Fx [kN]	%
70	70	-1,321	113%
	82	-1,321	113%
143	155	-2,427	93%
	166	-2,427	93%

Eigenfrequencies (table 3.14):
Also in this situation, there is no difference compared to the reference situation.

Axial forces (table 3.15):
Here it looks as if element nr 70 is the stronger element, as in the situation with only one weak element, because this element takes up more axial force, while element 143 takes less. From the model, it would be expected that both elements would take up less force and higher forces would be redistributed to the surrounding columns.

Stresses (table 3.16):
The bending stresses in both the elements have decreased to around 80%, which supports the idea that the forces have redistributed to the stronger surrounding elements.
Apparently, when one of two elements that meet at the top is weaker, the forces are redistibuted to the inner column, even when this element is also weak. This indicates that the connection has a very low stiffness and cannot reditribute forces to the outer column when needed.

Table 3.16 stresses two weak elements

Elem	Pos	$\sigma_{c,0}$ [N/mm²]	σ_m [N/mm²]	%
70	70	-0,116	0,268	81%
	82	-0,116	-0,473	79%
143	155	-0,214	0,172	81%
	166	-0,214	-0,444	76%

Displacements (table 3.17 to 3.18):
In this situation, the maximum nodal displacements have increased slightly compared to the reference situation. Still, the increase is very limited and occur at the same nodes.

Table 3.17 nodal displacements two weak elements

Node Maxima	Ux [mm]	Uy [mm]	Uz [mm]	|U| [mm]	%
79	1,970	0,430	-0,288	2,037	101%
82	1,648	0,782	-0,948	2,056	102%
161	1,805	0,135	0,370	1,847	101%
81	1,814	0,720	-0,853	2,131	101%

The displacements and deformations of elements 70 and 143 now show some extra bending halfway of the columns, but almost no variations in deformation at the ends.

Table 3.18 element displacements two weak elements

Elem	Pos	Ux [mm]	Uy [mm]	Uz [mm]	|U| [mm]	%
70	70	0,560	-0,182	-0,422	0,725	100%
	25,00%	1,223	-0,073	-0,601	1,365	101%
	50,00%	1,975	0,234	-0,846	2,161	103%
	75,00%	2,291	0,575	-1,011	2,57	104%
	82	1,648	0,782	-0,948	2,056	102%
143	155	0,598	-0,189	-0,496	0,8	99%
	25,00%	1,228	0,009	-0,617	1,375	100%
	50,00%	1,99	0,303	-0,749	2,148	103%
	75,00%	2,318	0,591	-0,800	2,523	103%
	166	1,648	0,772	-0,681	1,944	101%

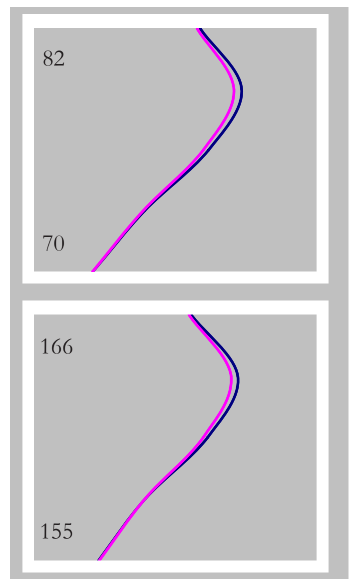

Figure 3.18 element deformation one weak element

When looked at the vertical displacements of nodes 82 and 166, the low stiffness of the connection element is shown (figure 3.19). The vertical displacement of node 82 is 0,948 mm (table 3.16), while for node 166 this is only 0,681 (table 3.18). Since this is quite a large difference over a very small length, the beam that joins this element with the A-frame is relatively straight and this difference must be caused by bending or rotoation of the connection element.
From this situation, it can be concluded that the structure, when one or two weaker elements are present, redistributes its forces to the inner column. This is caused by the low stiffness of the connection element. The dimensions of this element have therefore a much higher influence on the stiffness of the structure as a whole compared to the strength and stiffness parameters of the round wood columns.

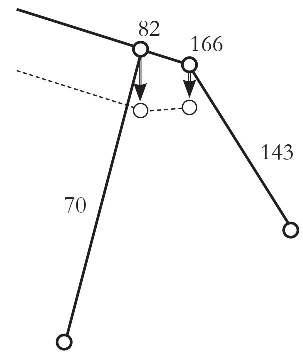

Figure 3.19 deformation connection element

3.3.4 Line of weak elements

In this situation a line of weak elements, starting at element nr 143, from top to bottom is present.

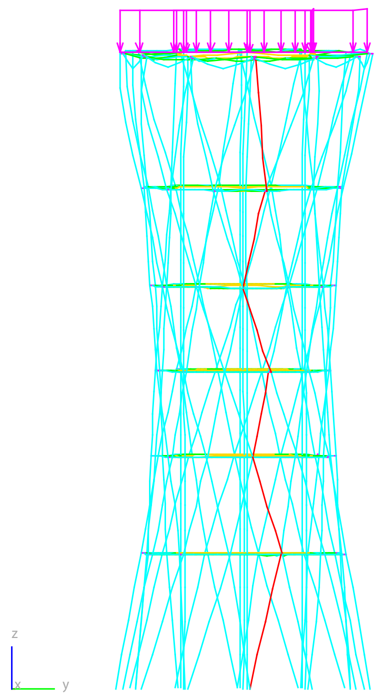

Figure 3.20 front view line weak elements

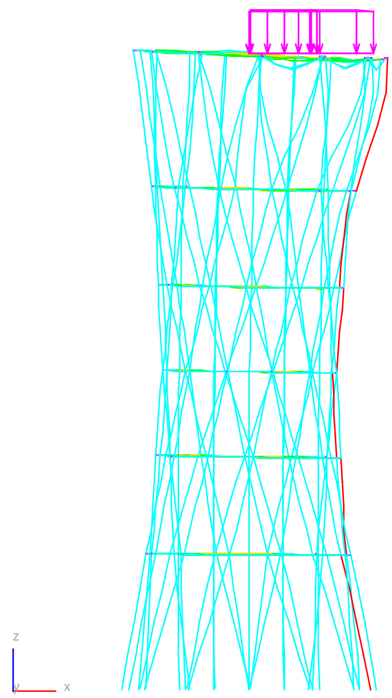

Figure 3.21 side view line weak elements

Table 3.19 eigenfrequencies line weak elements

Mode	Frequency [Hz]	Period [s]	%
1	0,190	5,239	99%
3	0,300	3,332	99%
4	0,370	2,702	99%

Table 3.20 axial forces line weak elements

Elem	Pos	Fx [kN]	%
70	70	-1,391	119%
	82	-1,391	119%
143	155	-2,382	92%
	166	-2,382	92%

Eigenfrequencies (table 3.19):
Also in this situation the weak elements have almost no influence on the eigenfrequencies of the structure as a whole.

Axial forces (table 3.20):
The same happens here as in the previous situations. Element nr 70 takes up more force than the weaker element 143, but as noticed in the situation with two weak elements, this has to be contributed to the low stiffness of the connection element. Because in this situation there are more weak elements and the strucure deforms more, the redistribution is larger due to second order effects.

Stresses (table 3.21):
The stress distributions are equal to the situation with one weak element. Again it can be seen that the weaker element is relieved of stresses.

Table 3.21 stresses line weak elements

Elem	Pos	$\sigma_{c,0}$ [N/mm²]	σ_m [N/mm²]	%
70	70	-0,123	0,334	101%
	82	-0,123	-0,601	100%
143	155	-0,210	0,160	76%
	166	-0,210	-0,410	70%

Displacements (table 3.22):
The displacements get a little bit higher, but are still well within the maximum deformation limits (at frequencies below 1Hz these are more than 12mm, chapter 3.1)

Table 3.22 nodal displacements line weak elements

Node	Ux	Uy	Uz	|U|	%
Maxima	[mm]	[mm]	[mm]	[mm]	
79	1,998	0,423	-0,291	2,064	102%
82	1,687	0,766	-0,943	2,079	103%
161	1,837	0,136	0,376	1,880	102%
81	1,848	0,704	-0,865	2,159	102%

From the element deformation curve (figure 3.22) it can be seen, that the weak element nr 143 gets less bent. The ends of the element have larger displacements, while the middle part stays in the same position. This is in analogy with the smaller bending moments in element nr 143 (table 3.21).
The stronger element nr 70 shows almost the same deformation curve as in the reference situation.
Also here, node 82 has a larger vertical displacement than node 166, indicating a low stiffness of the connection element.

Table 3.23 element displacements line weak elements

Elem	Pos	Ux	Uy	Uz	|U|	%
		[mm]	[mm]	[mm]	[mm]	
70	70	0,585	-0,197	-0,433	0,754	104%
	25,00%	1,243	-0,090	-0,607	1,387	103%
	50,00%	1,95	0,208	-0,836	2,132	102%
	75,00%	2,25	0,545	-0,991	2,519	102%
	82	1,687	0,766	-0,943	2,079	103%
143	155	0,624	-0,206	-0,520	0,838	104%
	25,00%	1,218	-0,014	-0,635	1,373	100%
	50,00%	1,94	0,271	-0,759	2,101	100%
	75,00%	2,27	0,558	-0,811	2,475	101%
	166	1,687	0,753	-0,705	1,978	103%

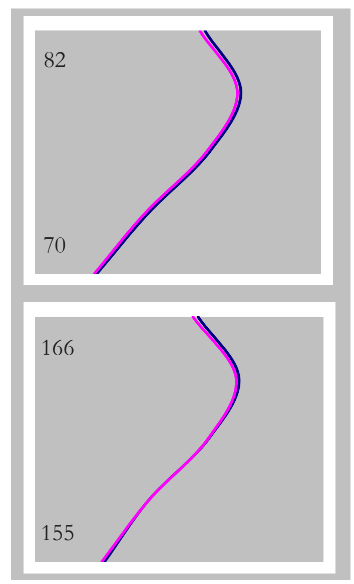

Figure 3.22 element deformation line weak elements

3.3.5 *One element missing*

In this situation one element (nr 143) is missing. This situation could arise when an element is so weakened that it fails and no longer contributes to the load bearing structure of the viewing platform.

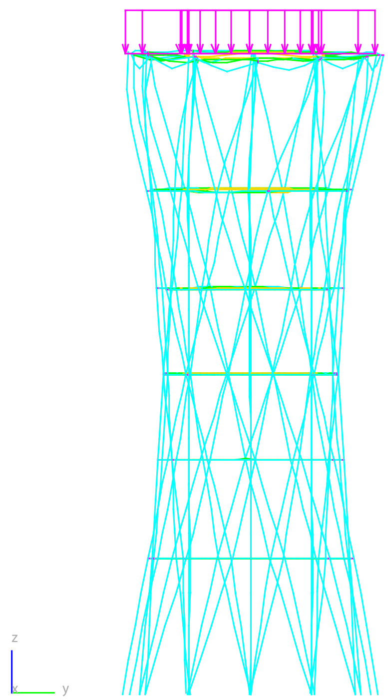

Figure 3.23 front view one missing

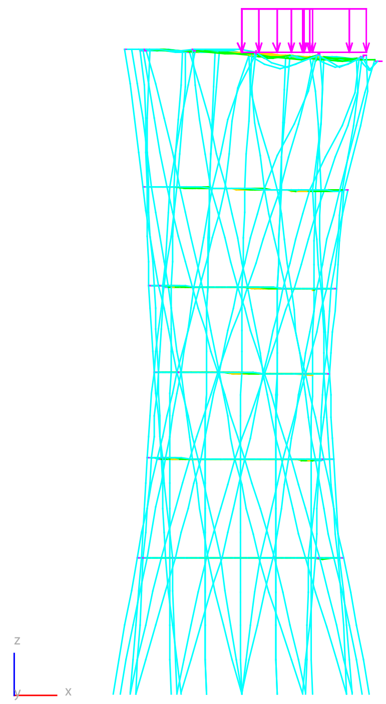

Figure 3.24 side view one missing

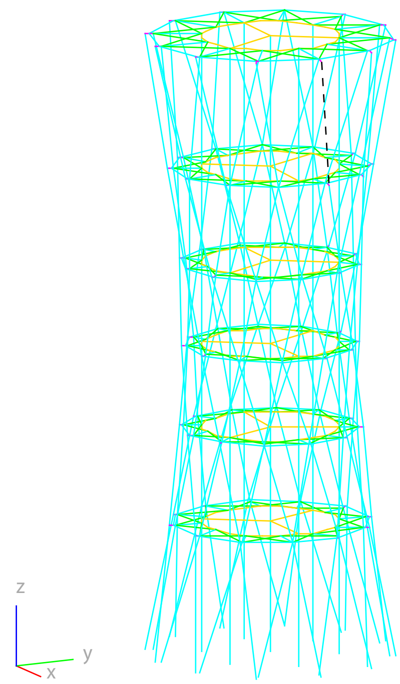

Figure 3.25 3d view one missing

Eigenfrequencies (table 3.24):
No large variations from the reference situation can be found. Only the torsional mode 4 decreases slightly more in frequency, but this mode is unlikely to be induced by persons on the top level.

Axial forces (table 3.25):
The axial force in element 70 has risen to 342% of the reference situation. This is because this element now has to take up all the force from the missing element nr 143. This initial force in the reference situation was 2,6 kN (table 3.4). The original force in element nr 70 was 1,2 kN. This total of 3,6 kN is a rise of 322%. The extra 20% can be explained by the extra deformation and second order effects.

Stresses (table 3.26):
As expected, the axial stresses have increased as much as the axial forces, but the bending stresses have decreased. The reason for this is explained in the discussion of the displacements.

Table 3.24 eigenfrequencies one missing

Mode	Frequency [Hz]	Period [s]	%
1	0,189	5,266	99%
2	0,193	5,177	101%
3	0,301	3,317	100%
4	0,361	2,77	97%
5	0,374	2,667	100%

Table 3.25 axial forces one missing

Elem	Pos	Fx [kN]	%
70	70	-3,994	342%
	82	-3,994	342%

Table 3.26 stresses one missing

Elem	Pos	$\sigma_{c,0}$ [N/mm²]	σ_m [N/mm²]	%
70	70	-0,353	0,211	64%
	82	-0,353	-0,153	26%

Displacements (table 3.27 to 3.28):
The maximum displacements have increased considerably. This shows the fragile balance situation of the structure.

Table 3.27 nodal displacements one missing

Node	Ux	Uy	Uz	|U|	%
Maxima	[mm]	[mm]	[mm]	[mm]	
79	2,19	0,770	-0,247	2,335	116%
82	1,717	1,314	-1,262	2,503	124%
161	1,939	0,303	0,415	2,006	109%
166	1,717	1,311	-1,35	2,547	121%

The element displacement curve shows a more straight element, explaining the lower bending stresses. This is caused by the displacement of node 166. Because there is no element anymore to support this node in vertical direction, the node has a larger vertical deformation than node nr 82, reducing the bending moment at the top of the element (figure 3.26). This also causes the bending moment at the bottom of the element to reduce.

Table 3.28 element displacements one missing

Elem	Pos	Ux	Uy	Uz	|U|	%
		[mm]	[mm]	[mm]	[mm]	
70	70	0,565	-0,191	-0,511	0,785	109%
	25,00%	0,798	0,024	-0,649	1,03	76%
	50,00%	1,043	0,510	-0,854	1,441	69%
	75,00%	1,336	1,022	-1,075	1,996	81%
	82	1,717	1,314	-1,262	2,503	124%

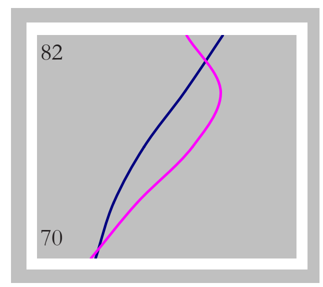

Figure 3.26 element deformation one missing

This situation shows the fragile balance of the viewing platform. to be able to predict the reaction of the structure in case of failure of an element, a more detailed model has to be made.

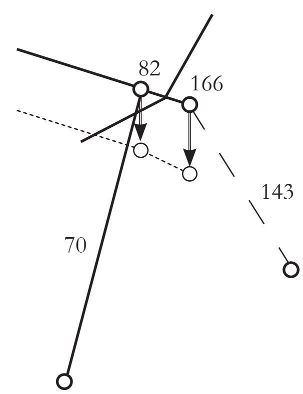

Figure 3.27 deformation connection element

3.3.6 *All weak elements*

This model describes the situation in which all the element are weaker than expected.

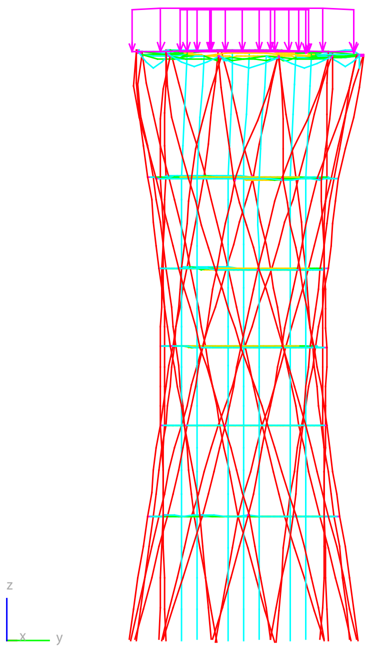

Figure 3.28 front view all weak elements

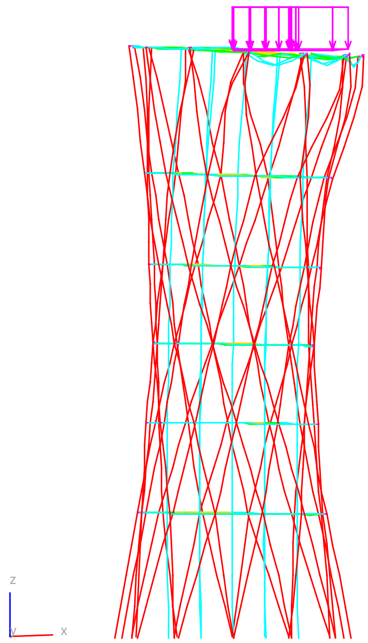

Figure 3.29 side view all weak elements

Table 3.29 eigenfrequencies all weak elements

Mode	Frequency [Hz]	Period [s]	%
1	0,170	5,865	89%
3	0,270	3,7	90%
4	0,337	2,96	90%

Table 3.30 axial forces all weak elements

Elem	Pos	Fx [kN]	%
70	70	-1,177	101%
	82	-1,177	101%
143	155	-2,554	98%
	166	-2,554	98%

Eigenfrequencies (table 3.29):
The eigenfrequencies have dropped considerably. In this model, the critical vibration mode 1 is even further away from the vibrations that can be induced by humans, but as this is a simplified model, these large variations could lead to dangerous situations in a more detailed model.

Axial forces (table 3.30):
The variations of the axial forces are small. No redistribution of forces takes place, because all the elements are weaker. Variations are caused by larger deformations and a low stiffness of the connection element.

Stresses (table 3.31):
The bending stresses have reduced to around 80-85%. This can also bee seen at the deformation curve (figure 3.30), showing more straight elements than in the reference situation. The larger deformations at the top because of the lower stiffness of the structure cause the elements at the top to straighten more, reducing the bending moments.

Table 3.31 stresses all weak elements

Elem	Pos	$\sigma_{c,0}$ [N/mm²]	σ_m [N/mm²]	%
70	70	-0,104	0,282	85%
	82	-0,104	-0,500	83%
143	155	-0,225	0,166	79%
	166	-0,225	-0,462	79%

Displacements (table 3.32 to 3.33):
The maximum displacements have increased considerably, but the variations in increase are small.

Table 3.32 nodal displacements all weak elements

Node	Ux	Uy	Uz	|U|	%
Maxima	[mm]	[mm]	[mm]	[mm]	
79	2,525	0,468	-0,376	2,596	129%
82	2,168	0,855	-1,184	2,614	130%
161	2,345	0,142	0,478	2,398	131%
81	2,354	0,789	-1,11	2,719	129%

As shown in the discussion of the bending stresses, the elements are more straight than in the reference situation.

Table 3.33 element displacements all weak elements

Elem	Pos	Ux	Uy	Uz	|U|	%
		[mm]	[mm]	[mm]	[mm]	
70	70	0,774	-0,229	-0,574	0,991	137%
	25,00%	1,556	-0,110	-0,778	1,744	129%
	50,00%	2,412	0,232	-1,052	2,642	126%
	75,00%	2,798	0,615	-1,238	3,121	126%
	82	2,168	0,855	-1,184	2,614	130%
143	155	0,824	-0,238	-0,684	1,098	136%
	25,00%	1,574	-0,013	-0,825	1,778	130%
	50,00%	2,435	0,315	-0,972	2,641	126%
	75,00%	2,826	0,638	-1,032	3,076	126%
	166	2,168	0,847	-0,912	2,501	131%

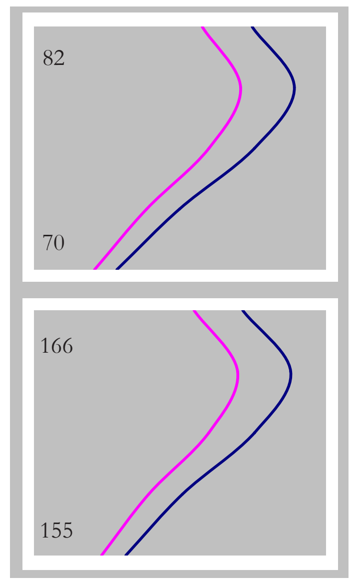

Figure 3.30 element deformation all weak elements

The increase is in the same range as the increase of the maximum nodal deformation.
This model shows that the geneal deformation of the structure is larger, but no fundamental changes in local deformations occur. Although all eigenfrequencies, stresses and defromations are all well within the limits in this model, more attention should be paid to this situation in a more detailed model.

3.4 Conclusion

The analysis of the viewing platform with different locations of weaker elements, showed no critical situations with one or more weak elements directly below and on the edge of the load area.
Only in the situation in which one element is missing due to failure, fundamental changes in deformation and distribution of forces is shown. Also, it was shown that the influence of the connection element is much larger than the stiffness and strength of the columns.
In the unlikely situation in which all elements are weaker than what the viewing platform was designed with, larger deformations and lower eigenfrequencies occur. Although in this model these values are still well within the limits, thsi situation should be analysed in a more detaild model.
The eigenfrequencies in all the other situations are almost identical and thus no larger risks occur than in the reference situation.

4 Connections

For the viewing platform, a new type of shear block joint connection was designed. This connection made use of pretension of the columns with a steel rod, locked between a steel end plate and a steel anchor block (figure 4.1).

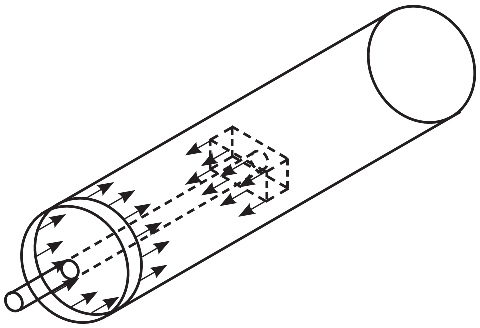

Figure 4.1 connection design

Figure 4.2 built connection

By pretensioning the end part of the timber column, the tightness is ensured, even after relaxation, shrinking and swelling of the timber. The steel rod is threaded and can be screwed into the connection element (figure 4.2).

Because only very low bending moments occur in the design of the viewing platform, this developed connection has only been tested for axial capacity. To determine its use in other constructions with higher bending moments, its moment capacity needs to be determined.
To test this capacity, the following experiment is set up (figure 4.3 to 4.4).
A round wood pole is fitted with the connection. The threaded steel rod is screwed into a steel beam, the other side is loaded perpendicular to its direction. The vertical deformation on the loaded end is measured. From this, the rotation of the connection can be determined.
By this experiment, the timber is loaded axially by the pretension and in bending by the point load.

Before the tests are performed, a model is made to describe the failure mechanisms of the connection and to predict the moment capacity. This model is later verified with the test results.

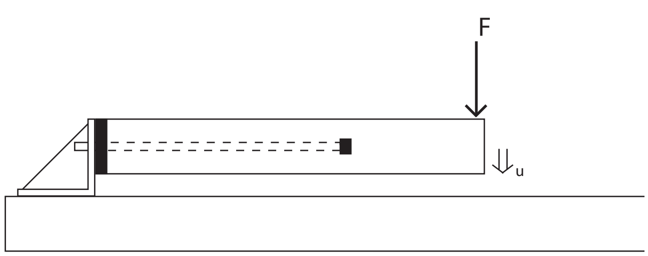

Figure 4.3 connection test model

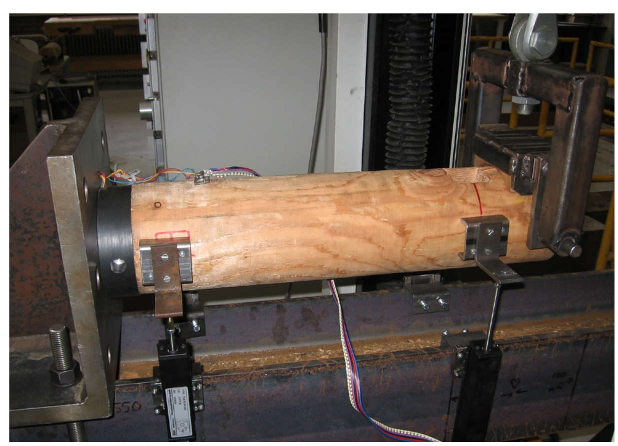

Figure 4.4 connection test setup

4.1 Failure model

To predict the capacity of the connections, first the possible failure mechanisms need to be described. There are 8 different mechanisms that can occur which will cause failure of the connection:

1 Yielding of the steel rod.
This will occur when the axial stress in the steel rod caused by the pretension and rotation of the connection exceeds the yield stress. The maximum steel force is thus determined by:

$$\sigma_{t,d} = \frac{F_p}{A_s} \leq f_{t,d}$$

2 Compression stress failure of the timber behind the steel anchor. This compression stress is limited by:

$$\sigma_{c,o,d} = \frac{F_p}{bh - \frac{\pi}{4} D_{hole}^2} \leq f_{c,o,d}$$

3 Bending stress failure of the steel anchor. This occurs when the bending stress exceeds the yield stress of the steel anchor:

$$\sigma_{y,d} = \frac{3F_p \left(b + D_{sr}\right)}{4d^2 \left(h - D_{sr}\right)} \leq f_{y,d}$$

4 Tension stress failure of the timber at the location of the steel anchor. This tension stress is limited by:

$$\sigma_{t,o,d} = \frac{F\left(a - l_{end}\right)}{W}$$

5 Shear stress failure of the timber around the steel rod. This shear stress is limited by:

$$\sigma_{v,d} = \frac{F_p}{\frac{3}{2} l_{end} \left(b + h\right)} \leq f_{v,d}$$

6 Friction force at the end plate. The friction force developed by the pretension and friction constant between the timber and steel should be greater than the vertical load:

$$F_f = F_p \mu \geq F$$

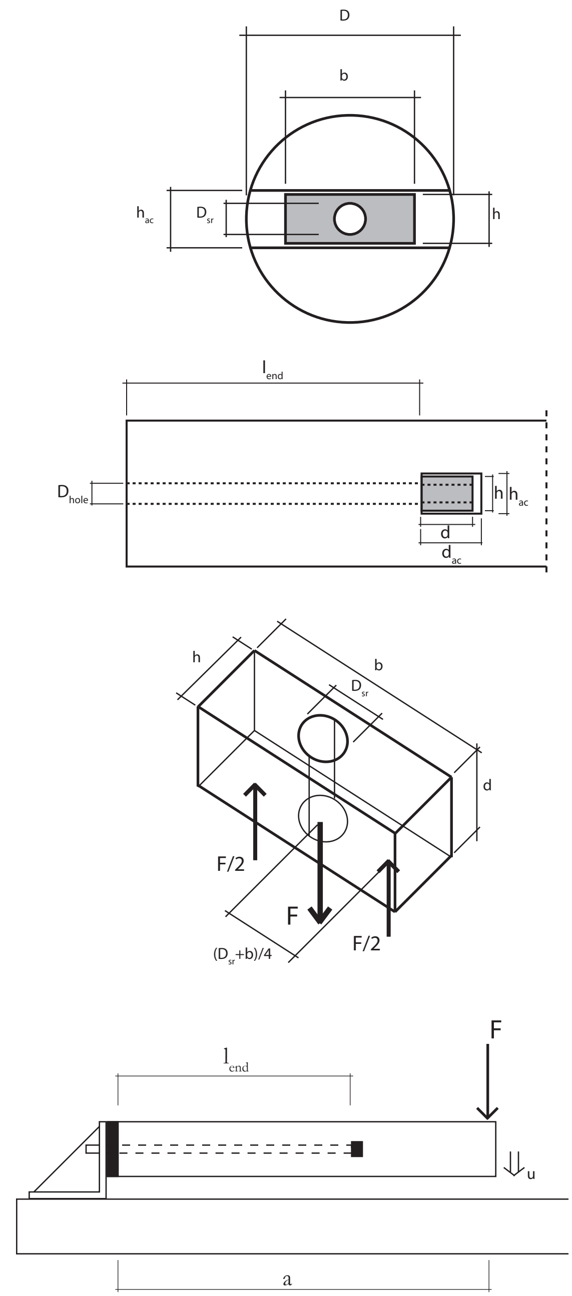

Figure 4.5 connection dimensions

7 Compression stress failure of the timber at the end plate. This compression stress is limited by:

$$\sigma_{c,o,d} = \frac{M\left(\frac{D}{2} - nc\right)}{I_{zz}} + \frac{F_p}{A} \leq f_{c,o,d}$$

8 Shear stress failure of the timber at the end plate. This shear stress is limited by:

$$\sigma_{v,d} = \frac{\frac{3}{2}F}{\frac{1}{4}\pi\left(D^2 - D_{hole}^2\right)} \leq f_{v,d}$$

All stresses are expressed in external loads and section properties. To determine these values, three different situations of the stresses at the end plate need to be looked at.

- compression stresses in the entire cross section
- reduction of the cross section because of "tensile" stresses
- plastic deformation of the compressed timber

4.1.1 Compression stresses

At low loads, the stresses induced by the bending moment are smaller than the compression stresses by the pretension. So in this case, only compression stresses occur in the cross section.

The following relations apply:

$$F_{c,r} = F_p$$

$$\sigma_m = \frac{\frac{1}{2}MD}{I_{zz}}, \sigma_p = \frac{F_p}{A}$$

$$I_{zz} = \frac{1}{64}\pi D^4, A = \frac{1}{4}\pi D^2$$

$$e = \frac{M}{F_c}$$

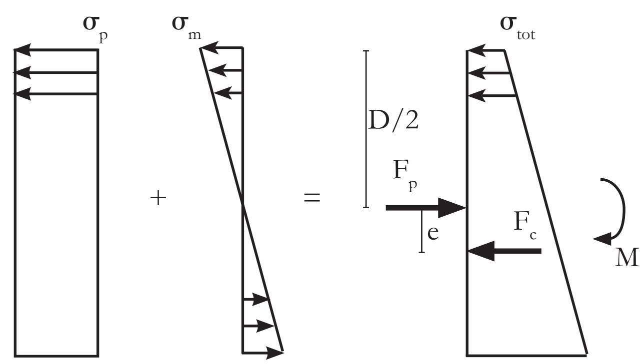

Figure 4.6 compression stress distribution

The connection will rotate around the point at distance e from the steel rod. This causes extra stresses in the steel rod:

$$\varepsilon = \frac{\sigma}{E}, \kappa = \frac{\varepsilon_b - \varepsilon_t}{D}$$

$$\Delta\varepsilon_s = \kappa\varepsilon \Rightarrow \Delta\sigma_p = \kappa\varepsilon E_s \Rightarrow \Delta F_p = \Delta\sigma_p A_s$$

$$F_{p,tot} = F_{pw} + \Delta F_p$$

4.1.2 *Reduction cross section*

At a certain point, the bending stresses at the top are equal to the compression stresses. When the load increases even further, the cross section gets smaller, because tension stresses can not be transferred from the timber to the end plate.

In this situation, the following relations apply:

$$F_{c,r} = F_p, \sigma_p = \frac{F_p}{A}$$

$$\sigma_{m,top} = \frac{M\left(\frac{1}{2}D - x + nc\right)}{I_{zz}}$$

$$\sigma_{m,bottom} = \frac{M\left(\frac{1}{2}D - nc\right)}{I_{zz}}$$

$$\sigma_{m,top} = \sigma_p \Rightarrow x = \frac{1}{2}D + nc - \frac{F_p I_{zz}}{MA}$$

$$\kappa = \frac{\varepsilon_o}{D-x}, e = \frac{M}{F_c}, \Delta\sigma_p = \kappa e E_s$$

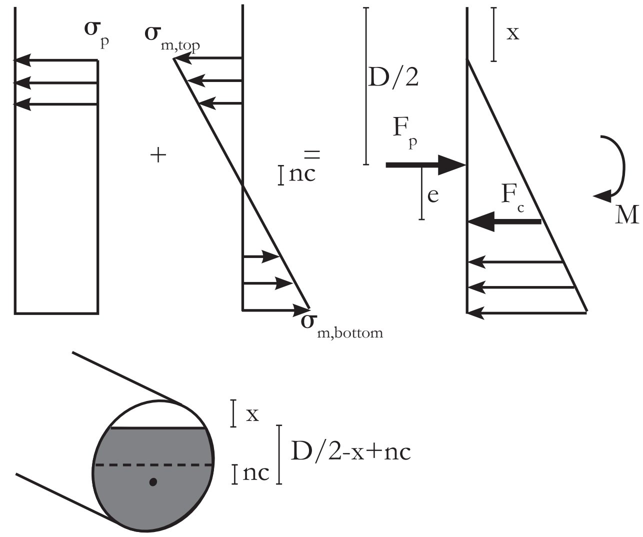

Figure 4.7 reduced stress distribution

Because the cross section gets smaller, also the cross sectional parameters decrease. To calculate these values, the value of x is expressed in angles from the origin. Then, the cross sectional values can be calculated by (Appendix A4):

$$I_{zz} = \frac{1}{4}R^2\left(\pi - \alpha + \frac{1}{4}\sin 4\alpha\right)$$

$$A = \frac{1}{16}R^2\left(\pi - \alpha - \frac{1}{2}\sin\left(-\pi + 2\alpha\right)\right)$$

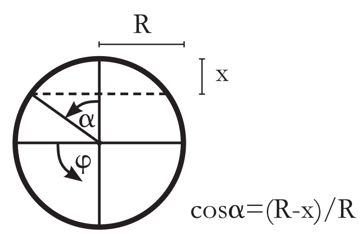

Figure 4.8 reduced cross section

4.1.3 *Plastic deformation*

When the compression stresses at the bottom of the cross section reach the maximum timber compression stress, local buckling will occur, inducing plastic deformation of part of the cross section. The same relations apply, only the value of the total compression force is no longer linear. The distance between the steel rod and the plastic deformation zone is calculated by:

$$z = \left(\frac{\sigma_{bottom} - \sigma_{c,o,d}}{\sigma_{bottom}}\left(D - x\right)\right) + \frac{D}{2}$$

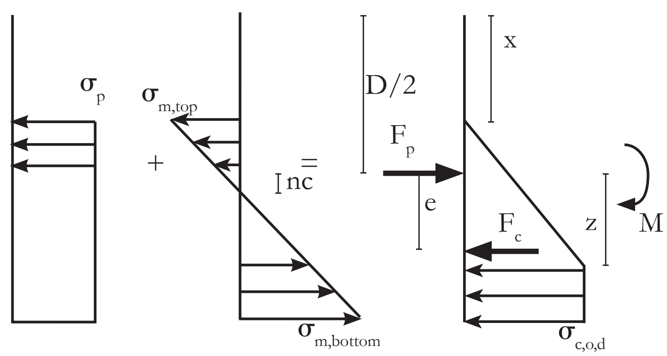

Figure 4.9 plastic stress distribution

Now that all the relations are known, its values can be calculated in Excel. This is done by changing the position of the normal forces center nc so that the compression force F_c equals the tension force F_p. The total compression force F_c can be calculated by integrating the compression stresses over the effective cross section (Appendix A4):

$$F_c = \int_{-\frac{\pi}{2}+\alpha}^{\beta} \sigma\, dA + \int_{\beta}^{\pi/2} \sigma_{c,o,d}\, dA$$

$$dA = b(z)dz = 2R\cos\varphi dz$$

$$z = R\sin\varphi$$

$$dA = 2R\cos\varphi R\cos\varphi d\varphi$$

$$dA = 2R^2\cos^2\varphi d\varphi$$

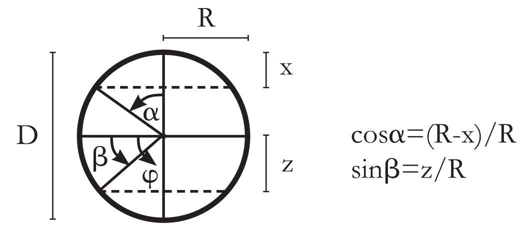

Figure 4.10 cross sectional parameters

When all values are known and calculated, the rotation angle of the connection can be calculated from the slope of the strain diagram:

$$\kappa = \frac{\varepsilon_{bottom} - \varepsilon_{top}}{D - x}$$

$$\phi = \kappa a$$

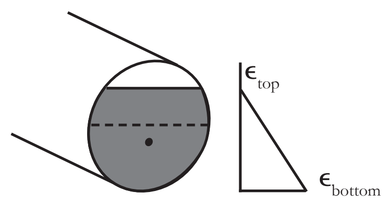

Figure 4.11 rotation angle

4.1.4 Calculation

To get an idea of the influence of the level of prestress on the connection rotation capacity, the calculation is done for three different initial prestress values of 1, 5 and 10 kN.
The graphs show the first parts of the M-φ-diagram and of the stress values of the steel rod.

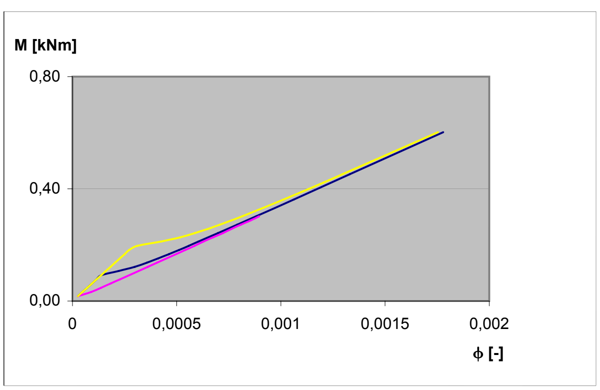

Figure 4.12 model M-ϕ relation

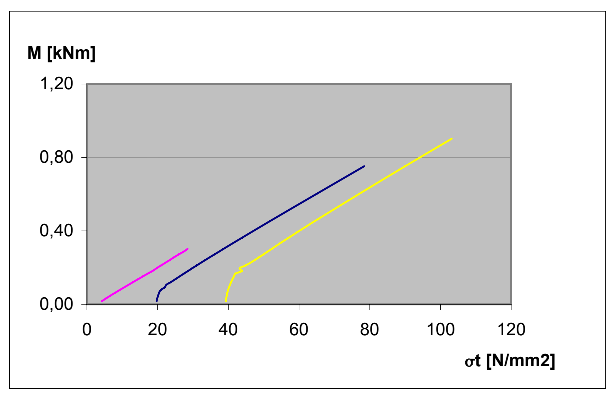

Figure 4.13 model M-σ_t relation

It can be seen, that with higher prestress values, the linear first fase continues for higher values of M. But eventually, all lines converge to the same values. From the stresses in the steel rod in can be seen that these stresses do not increase much untill the point is reached where the cross section decreases and rotation of the connection becomes much higher. After this, the slopes of the lines are all equal.
Also, from the excel data (Appendix A5) it can be shown that the connection fails at equal values of M, irrespective of the initial prestress value.

4.2 Experiment

4.2.1 Test Setup

In the experiments, the data from the model will be checked.
The connection's principle is based on a pretension that prevents the elements to loosen by shrinking and swelling of the wood. This can be caused by variations in relative humidity or in axial forces. Also, in this experiment, the pretension prevents the timber to slip away from its steel end plate.

First, the tested specimen is fitted with the connection on both sides, with the end plates touching the faces of the round wood pole. One end is attached with the steel rod screwed to a steel frame. The other end is attached to a jack. The specimen is supported by the same supports as used in the bending tests, to allow for horizontal deformations of the specimen during pretensioning.

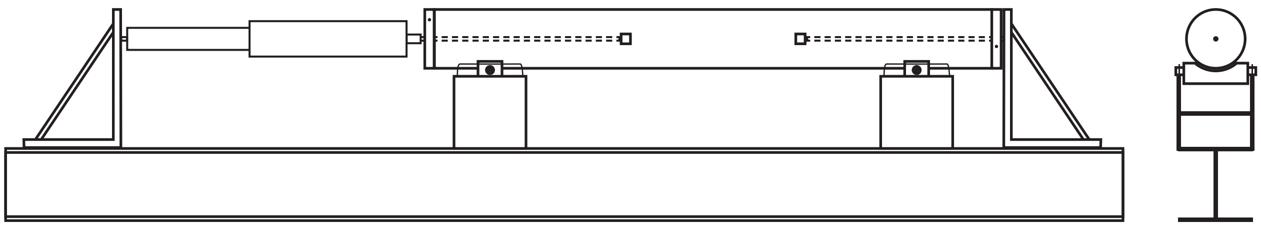

Figure 4.14 pretension step 1

Next, the jack is tightened to apply the desired pretension. This is measured by a pressure box attached between the jack and the steel rod. Also, electrical strain strips will be glued onto the steel rod to measure the steel stress over time. Because of the elongation of the steel rods, the end plates will move away from the timber faces.

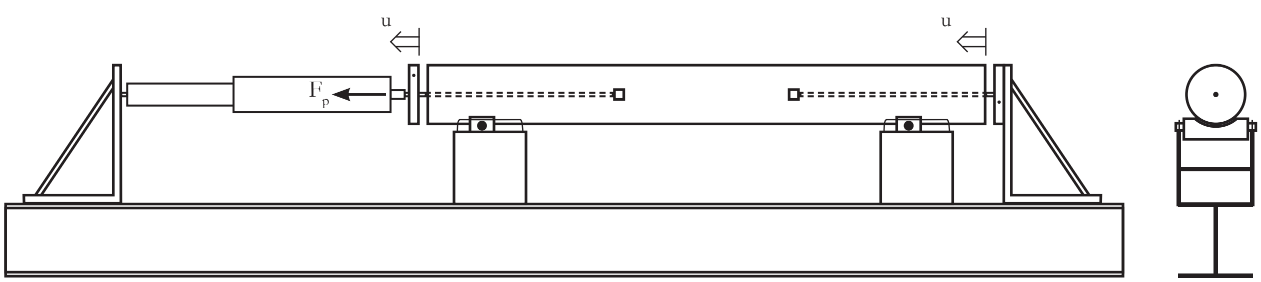

Figure 4.15 pretension step 2

By tightening the end plates back onto the timber faces, the pretension is locked in the timber between the steel anchor and the end plates and the jack can be detached from the steel rod.

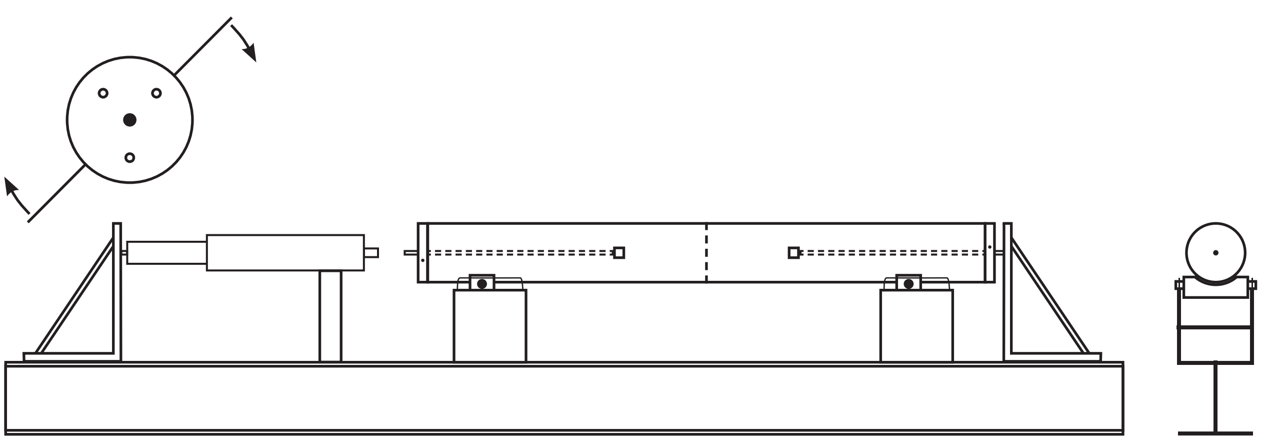

Figure 4.16 pretension step 3

Figure 4.17 shows the pretensioned specimen with the jack as it is used for the tests. The cables from the specimen are from strain gauges that are glued to the steel rod to be able to record the steel stress during pretensioning and testing. From these strain gauges the prestress in monitored and the jack is tightened untill the desired prestress is reached.

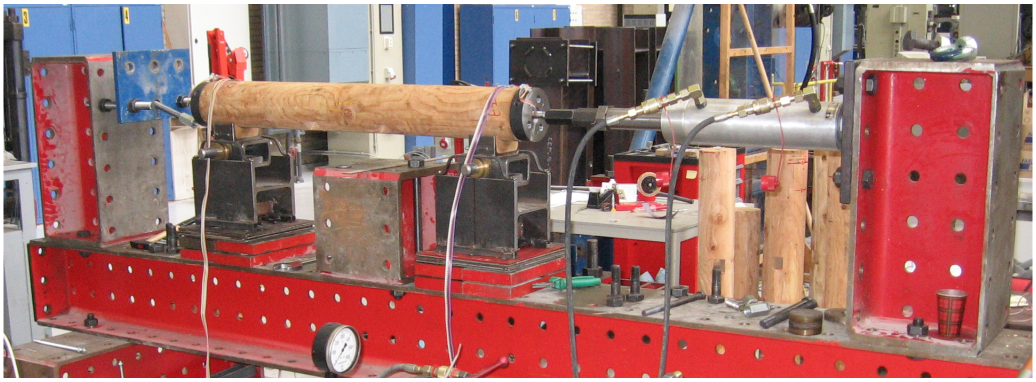

Figure 4.17 pretensioning setup

These strain gauges are glued at 120^0 angles onto a cleaned part of the steel rod close to the steel anchor (figure 4.18). From these three strain gauges the average strain and, after calibration, the average steel stress can be calculated. The principle of this calibration is explained more in detail in Appendix A4.

Figure 4.18 steel rod with strain gauges

Finally, the test specimen is sawn in two halves. Each part is tested for rotational capacity by screwing the steel rod in a similar steel frame that is mounted on the same load bench that was used for the bending tests. The rotation can be determined by measuring the vertical displacement of the free end (figure 4.19). This measurement is done with LVDT's on two sides of the specimen to correct for rotation as was done with the bending tests.

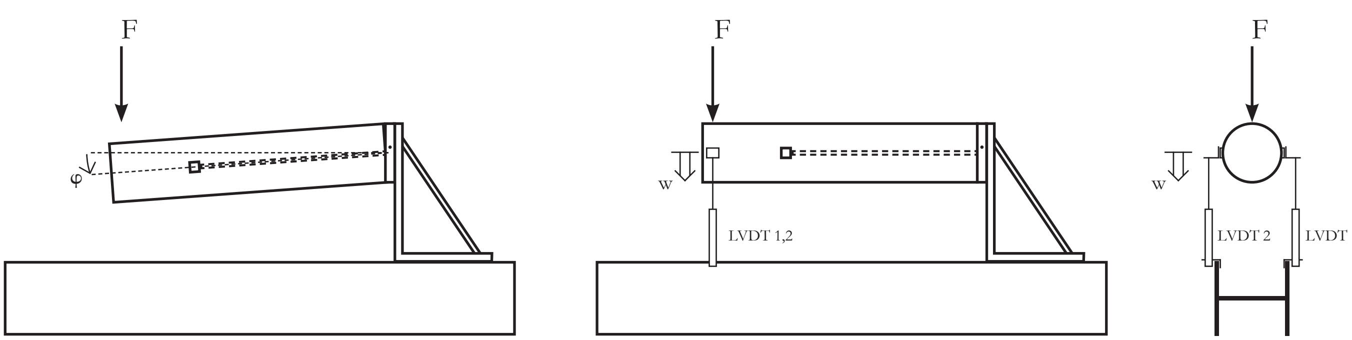

Figure 4.19 connection testing and displacement recording

As the vertical load increases, the timber face might slip away from the end plate. To correct for this displacement and to see when the connection fails for friction between the timber face and the steel end plate, a two more LVDT's are placed just after the end plate (figure 4.20).

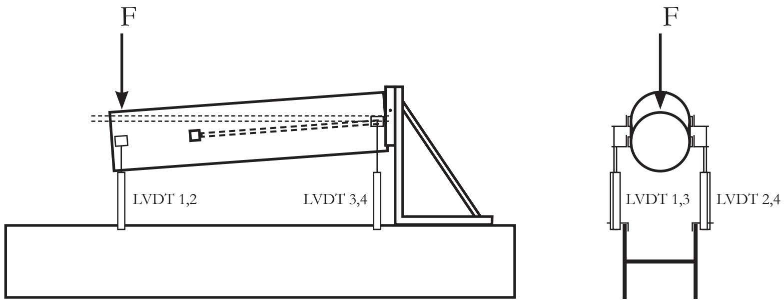

Figure 4.20 connection testing with extra LVDT's

To increase the capacity of the connection in vertical direction at the end plate, some specimen will be fitted with three dowels through the end plate in the timber face (figure 4.21).

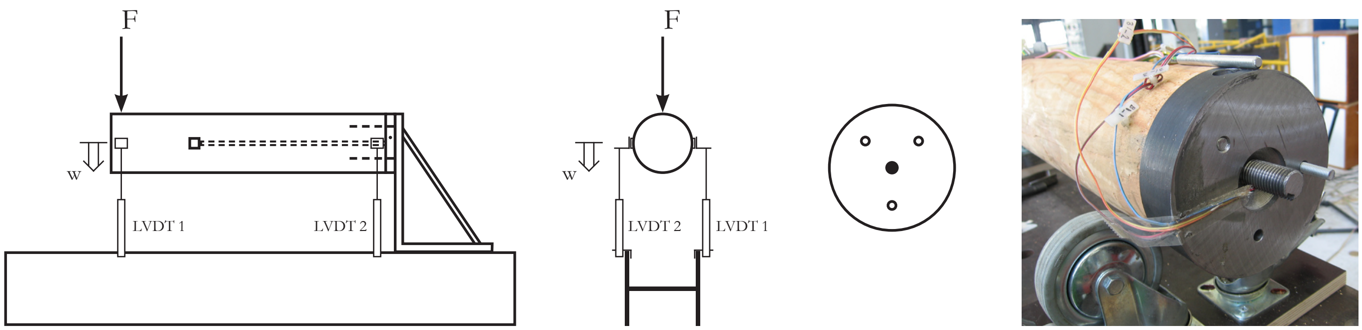

Figure 4.21 connection testing with dowels

Table 4.1 gives some values for the used dimensions, figure 4.22 shows the connection as it is loaded.

Table 4.1 connection dimensions

D	136	mm	**b**	70	mm
$\mathbf{D}_{sr}$	20	mm	**h**	40	mm
$\mathbf{D}_{hole}$	22	mm	$\mathbf{h}_{ac}$	45	mm
l	550	mm	**d**	40	mm
$\mathbf{l}_{end}$	400	mm	$\mathbf{d}_{ac}$	45	mm

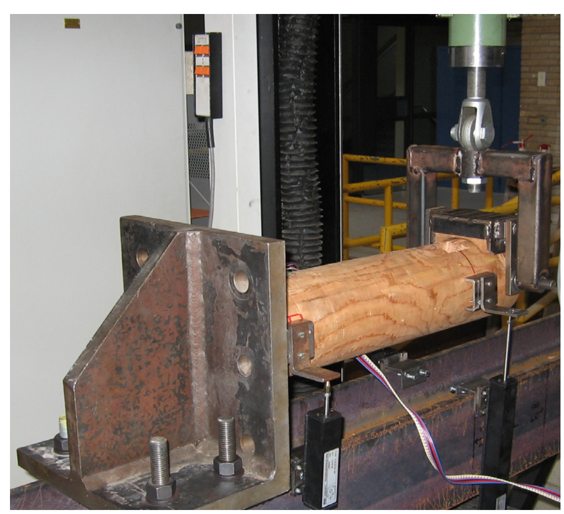

Figure 4.22 connection testing

4.2.2 *Results*

For the connection tests, a selection was made from the round wood columns that were used for the bending tests. Only those specimen of which more than 110 cm, the length required to make two connections from one column, was uncracked in the bending process were used. Of these, a selection was made of 6 specimen with an as wide range of strength parameters as possible to see the effect on the capacity of the connection. Table 4.2 gives the strength parameters of the selected specimen.

Table 4.2 connection specimen characteristics

Nr	MOE	density (12%)	fm	fc0
[-]	[N/mm2]	[kg/m3]	[N/mm2]	[N/mm2]
E1	7,40	550	37,36	28,91
E9	9,80	684	64,41	38,80
E11	8,47	638	43,72	32,29
E12	8,77	571	47,45	32,56
E14	8,23	523	31,58	29,39
E18	8,80	555	54,42	29,33

For each specimen, the strength characterisctics are put in the failure model and a calculation is made to predict the capacity of the connection. In the following chapters, the results of these calculations are compared with the test results.

To get an idea of the relaxation of the connection, the first specimen E1 is pretensioned to 10 kN and left to relax over the weekend. The result is presented in figure 4.23. In the figure, as in all the other figures in the next chapters, B1 and B2 stands for the two sides of the connection. The graph shows a decrease over time of the relaxation speed and a sensitivity to what seems to be temperature differences. Every top of the sinusoide occurs around 12:00 hours, every dip around 05:00 hours. This could be caused by shrinking and swelling of the timber due to temperature variations, but could also be caused by shrinking and swelling of the highly sensitive strain gauges itself. The big dip at the end is caused by the opening of a large door in

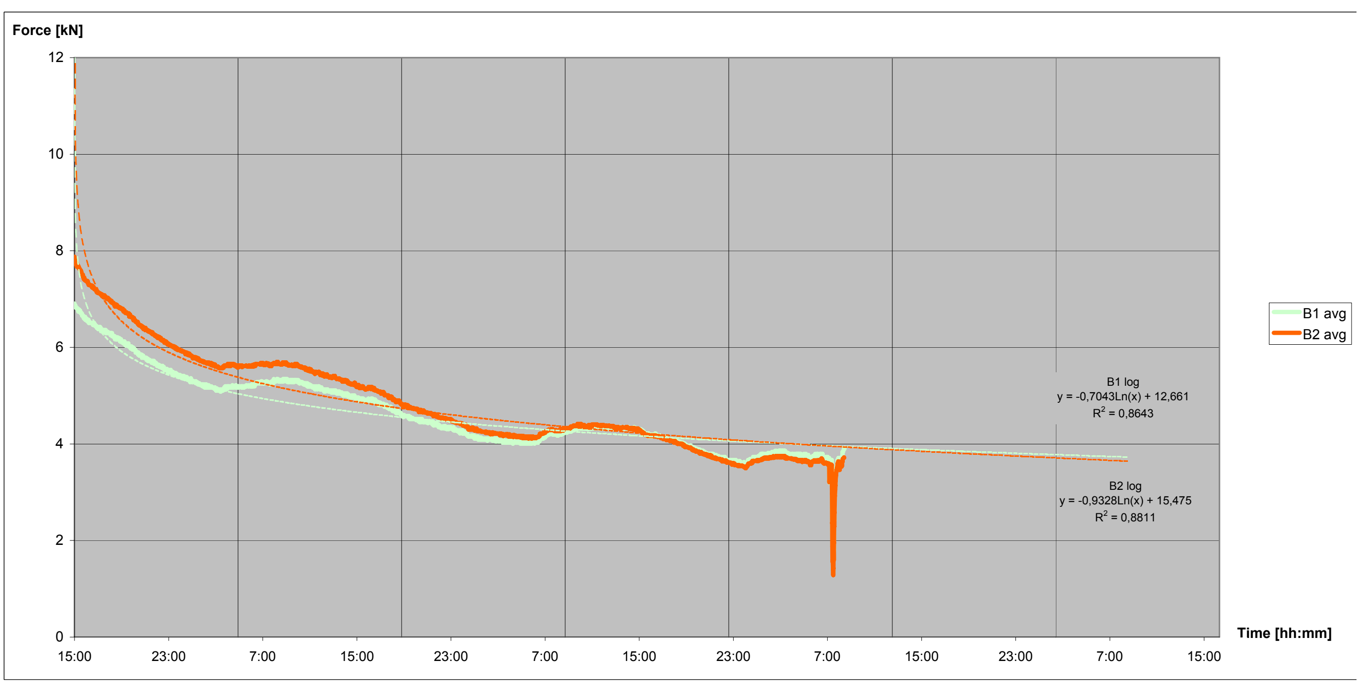

Figure 4.23 relaxation specimen E1

the test area at Monday morning 08:00 hours. In the figure, a logarithmic trendline is drawn for each side to predict the relaxation over time. For this, the last big dip is ignored. According to both logarithmic functions, the prestress would have reduced to around 3,3 kN in one week and to around 2,5 kN (B1) or 2,0 kN (B2) after three weeks. For side B1, this would mean a relaxation to around 35% and for side B2 to around 25% of the initial value.
Figure 4.24 shows the relaxation on a logarithmic scale. This initially does not, as would be expected, show

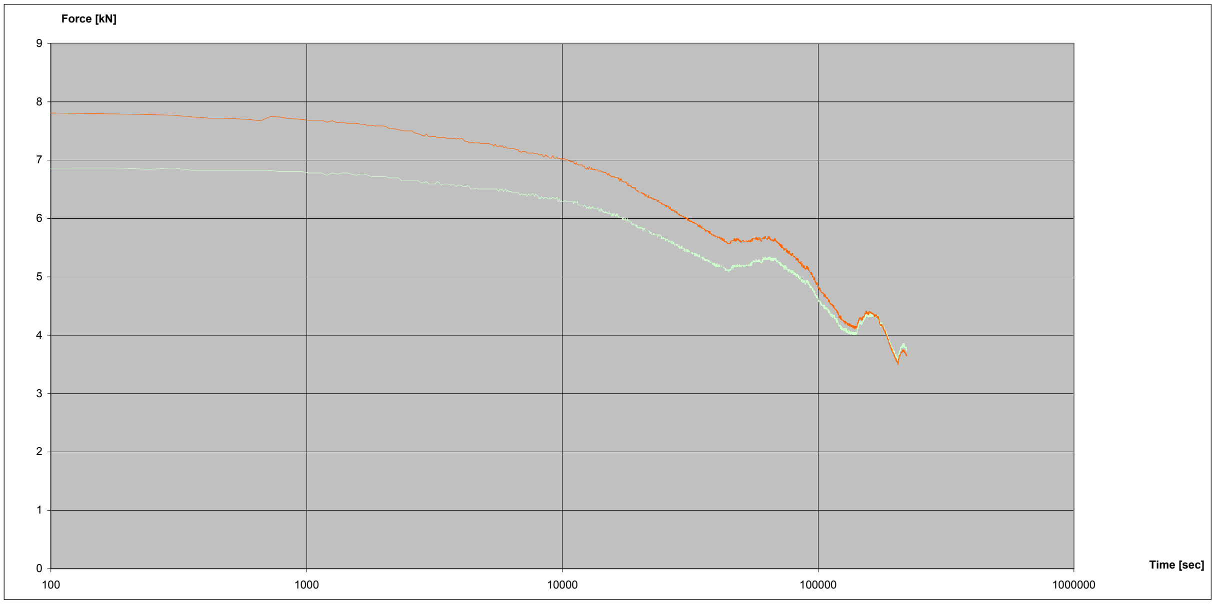

Figure 4.24 logarithmic relaxation specimen E1

a linear decrease of relaxation speed over time. To see if this trend continues over longer time, a second specimen (E12) is pretensioned after all tests have been done and left to relax for around three weeks. For the loading tests, 5 specimen, with 2 connections each, are used with different pretension levels. The results of these tests are presented below.

In the next graphs, the steel stresses are presented in average values only, to be able to compare these stresses with the results from the model. As explained in Appendix A4, the individual values for the three strain gauges sometimes show a relatively large bending moment in one of the steel rods. This is caused by a not perfectly perpendicular thread hole in the steel end plates and misalignment of the steel and timber faces. Because of this, when the steel end plates are tightened to the timber faces after pretensioning, the steel rod is bent, causing bending moments, also at the other end of the steel rod.
The red-green graphs show the results from the tests, the yellow graphs show the results from the calculation model. All specimen are first loaded to around one or two kN, then unloaded to 0,5 kN and loaded back to near failure. The graph σ_σ-time shows the stresses in the steel rod over time, the graph Force-w shows the force of the point load over deformation of the specimen.

Only the results of specimen E1 and E9 are given with some explanation, all the othe results can be found in Appendix A5.

The first specimen E1 was tested after the 65 hour relaxation period. The pretension that was left in the steel rod had reduced to 3,9kN, which corresponds with a steel stress of 18,3 N/mm^2. When the connection is fixed to the steel beam, the end plate is tightened to this beam, increasing the steel stress in the tension rod (figure 4.25).

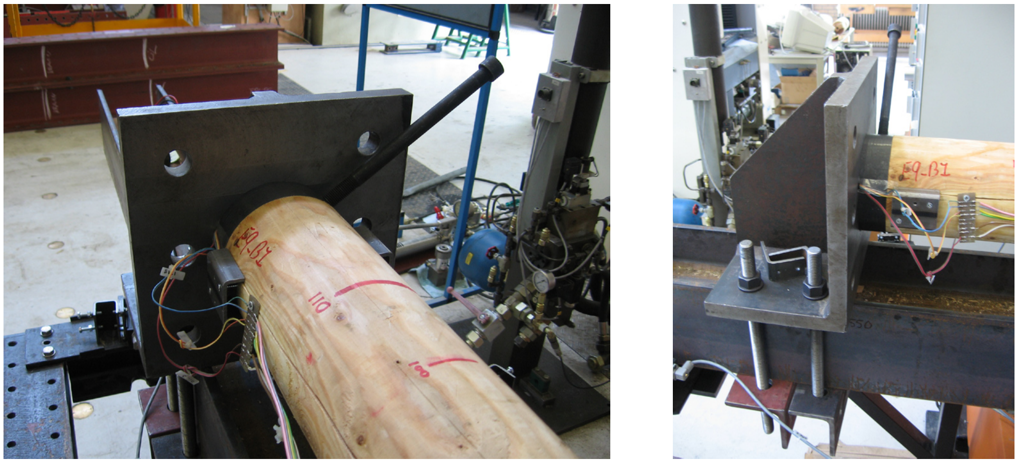

Figure 4.25 connection tightening specimen E1 side B1

After tightening, the steel stress at the start of the loading process for this specimen is 21,9 N/mm^2 or 5kN (figure 4.26). Figure 4.27 shows the deformation over time of the specimen under the point load (W1-2) and near the end plate (W3-4). No extra deformation of the specimen near the end plate compared to the deformation under the point load can be seen. This indicates the friction between the timber face and steel end plate is large enough to carry the vertical load, already at the low pretension of 5 kN.
The model calculation for this specimen predicted a deformation of 15mm at a point load of 5,5 kN. This corresponds very well with the actual average deformation of LVDT 1 and 2 (W1-2) in figure 4.28.

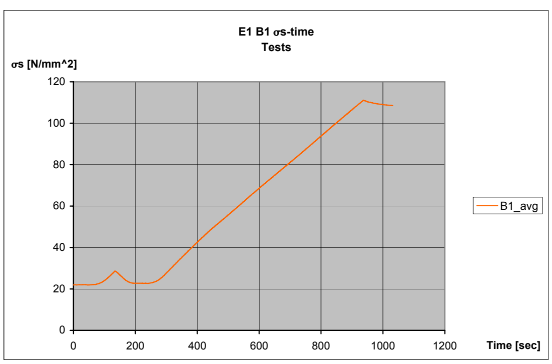

Figure 4.26 σ_t-time specimen E1 side B1

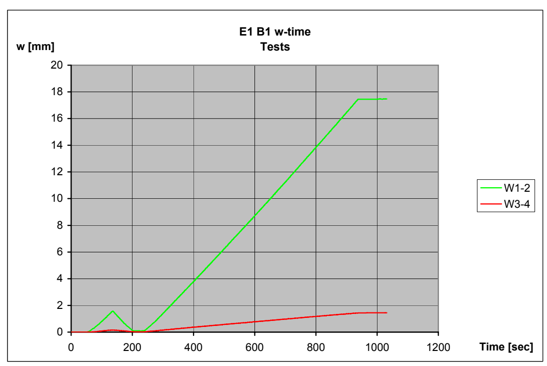

Figure 4.27 w-time specimen E1 side B1

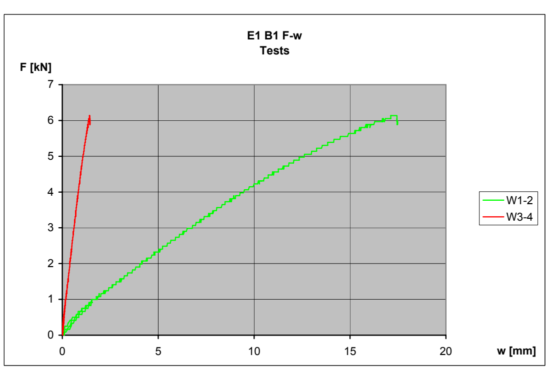

Figure 4.28 F-w specimen E1 side B1 test

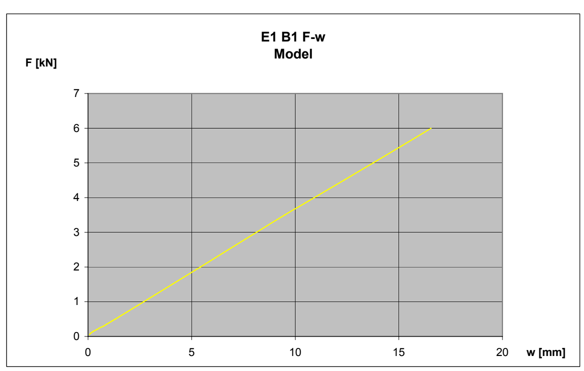

Figure 4.29 F-w specimen E1 side B1 model

Figure 4.30 shows no sudden decrease in slope of the M-ϕ line and thus stiffness of the connection. As can be seen from the graphs of the other specimen, this indicates that the top of the timber face gets disconnected from the steel end plate already in a very early stage of the loading process. The model (figure 4.31) predicts a more stiff rotation curve compared to the test results (C=ΔM/Δϕ=111 kNm/rad for the model and C=70 kNm/rad for the test result). Also, in the model the point where the top of the timber face gets disconnected from the steel end plate occurs at an earlier stage of the loading process than in the test (at 0,067 kNm in the model and at 0,240 kNm in the test). In the graphs, the line to this point is indicated as the full section and the line from this point as the reduced section.

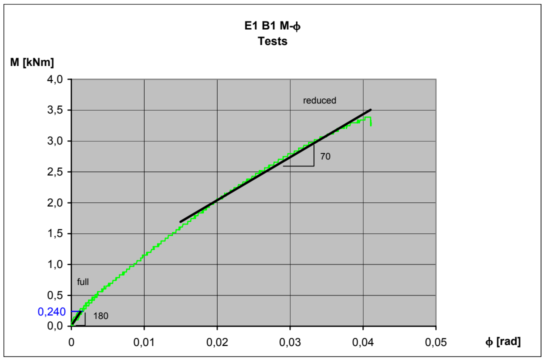

Figure 4.30 M-ϕ specimen E1 side B1 test

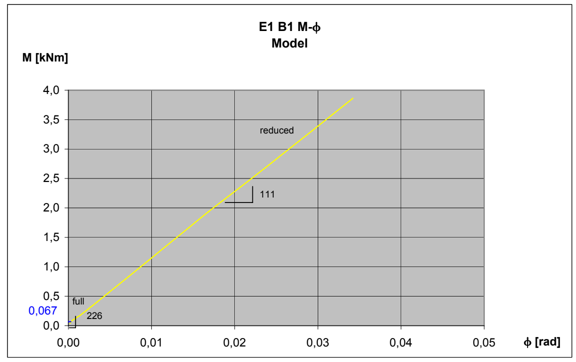

Figure 4.31 M-ϕ specimen E1 side B1 model

Figure 4.32 shows the rotation of the connection at the end of the loading process.

In figure 4.33, the steel stress of the tension rod shows a constant value when the timber face is still fully connected to the steel end plate and the connection rotates around or close to the heart of the tension rod. When the top of the timber face gets disconnected, the timber face starts to rotate around a point below the tension rod and the steel stress increases linearly. In the model however, this steel stress increases at a much higher rate than in the test (figure 4.34). At first sight it is not clear why this happens, because as can be seen from the other tests, the steel stresses from the model mostly correspond much better with those from the tests. Also, one would expect a decrease in stiffness when the steel starts to yield at 2 kNm. This does not show in figure 4.34, indicating that the failure model itself, or the translation to the calculations done in Excel, is incorrect for this mechanism.

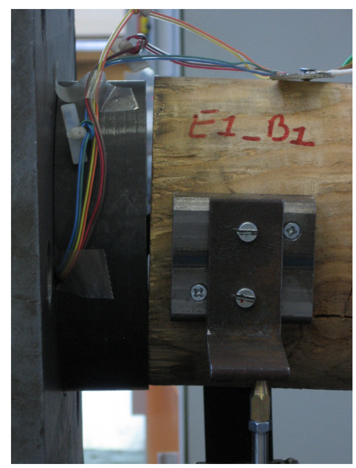

Figure 4.32 rotation specimen E1 side B1

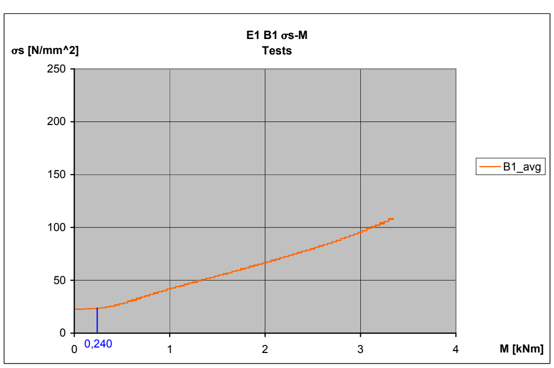

Figure 4.33 σ_s-M specimen E1 side B1 test

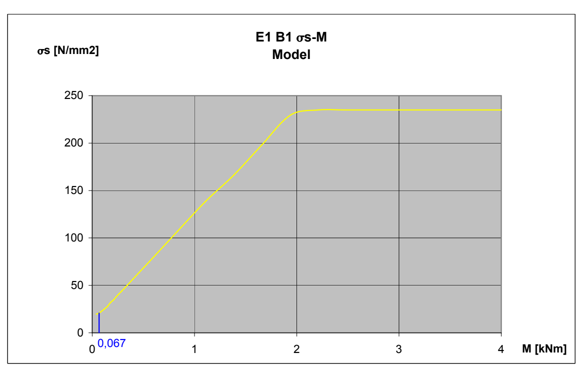

Figure 4.34 σ_s-M specimen E1 side B1 model

The other side of specimen E1 shows the same general results. This side was loaded a bit further, causing the steel rod to yield too much (Figure 4.35). This caused false readings from this rod in following tests, probably by overloading the strain gauges, so this rod was not used any longer but for the pretensioning of the specimen. With this side of the connection, the steel stress from the model corresponds somewhat better with that from the test (figures 4.41 to 4.42). Still, the model predicts a faster increase of steel stress.

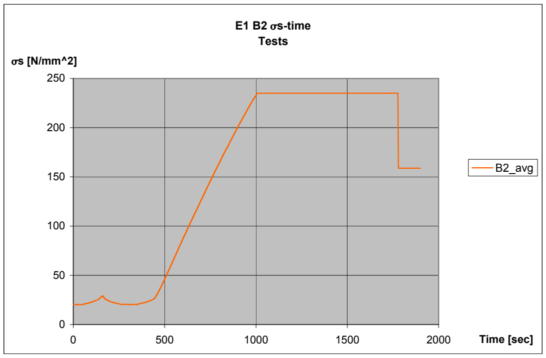

Figure 4.35 σ_t-time specimen E1 side B2

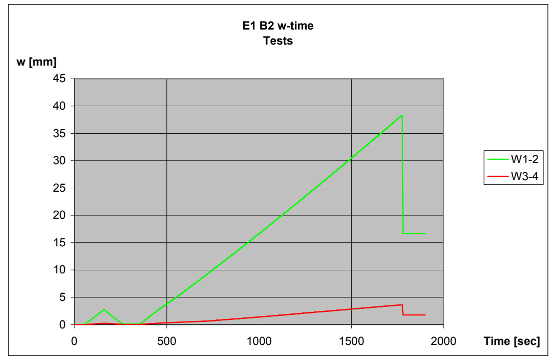

Figure 4.36 w-time specimen E1 side B2

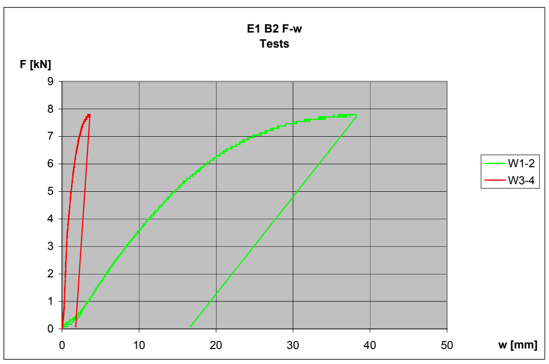

Figure 4.37 F-w specimen E1 side B2 test

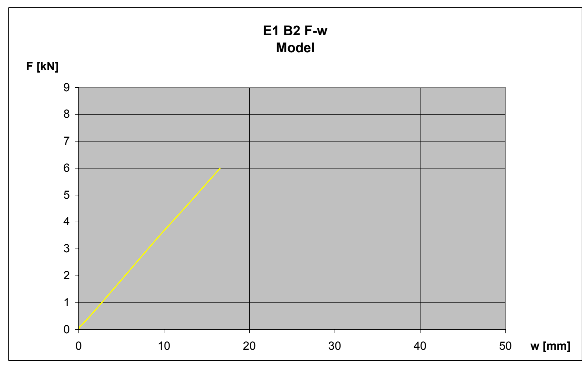

Figure 4.38 F-w specimen E1 side B2 model

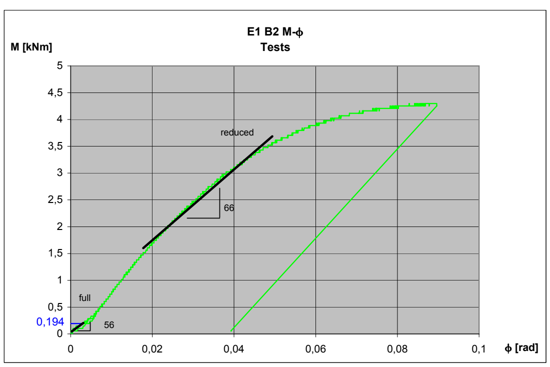

Figure 4.39 M-ϕ specimen E1 side B2 test

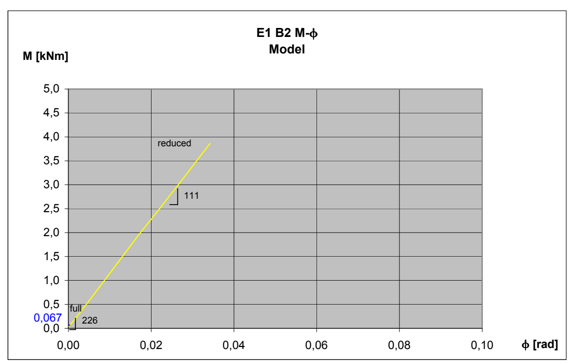

Figure 4.40 M-ϕ specimen E1 side B2 model

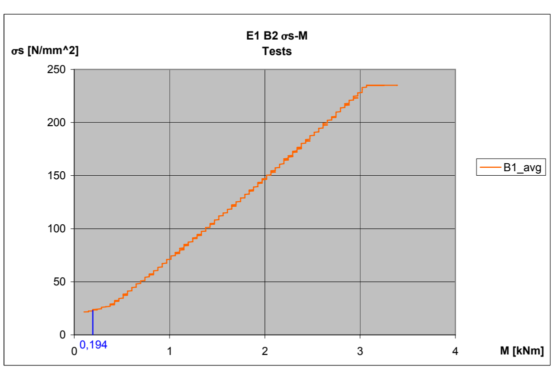

Figure 4.41 σ_s-M specimen E1 side B2 test

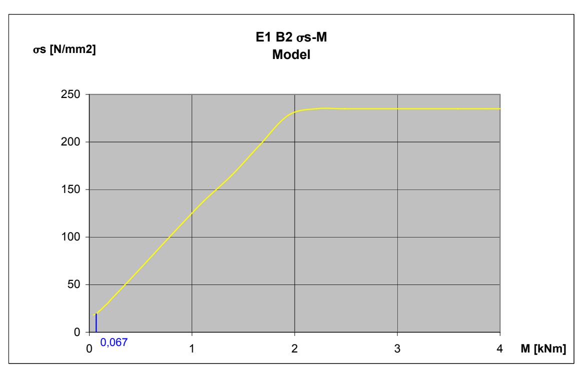

Figure 4.42 σ_s-M specimen E1 side B2 model

Side B1 of specimen E9 shows a sudden decrease in stiffness at a bending moment of 0,93 kNm. This side is pretensioned to 18,8 kN or 88 N/mm^2 (figure 4.43), causing the timber to be in full compression over a longer period of time and loading. Also, no friction failure occurs. The model shows the same general results as the tests. Only again the decrease in stiffness occurs earlier in the model and the stiffness in the model is higher than in the test (148 kNm/rad to 100 kNm/rad). The model does predict a higher value for the bending moment at which the timber gets disconnected from the end plate than for specimen E1.

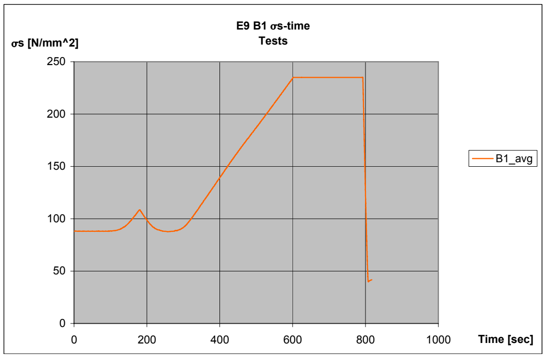

Figure 4.43 σ_t-time specimen E9 side B1

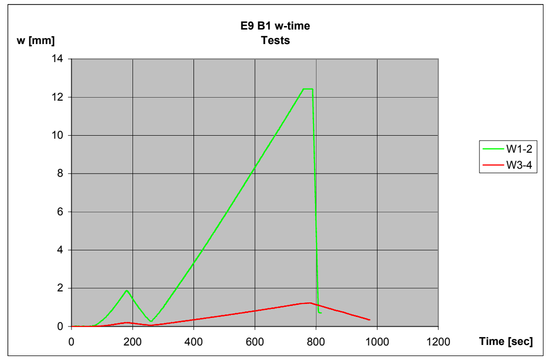

Figure 4.44 w-time specimen E9 side B1

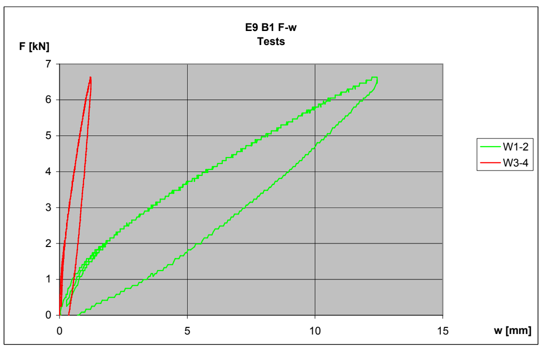

Figure 4.45 F-w specimen E9 side B1 test

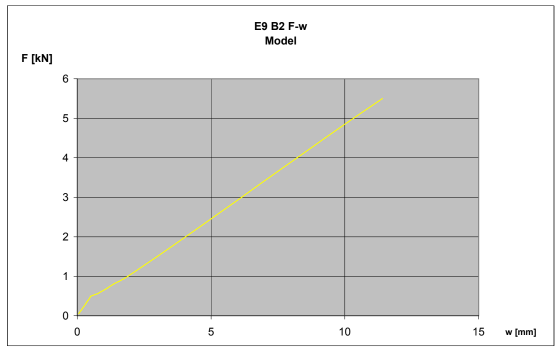

Figure 4.46 F-w specimen E9 side B1 model

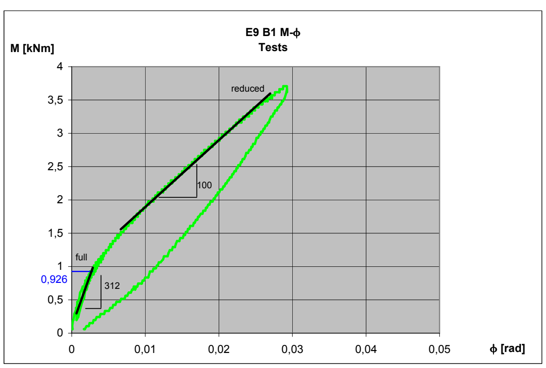

Figure 4.47 M-ϕ specimen E9 side B1 test

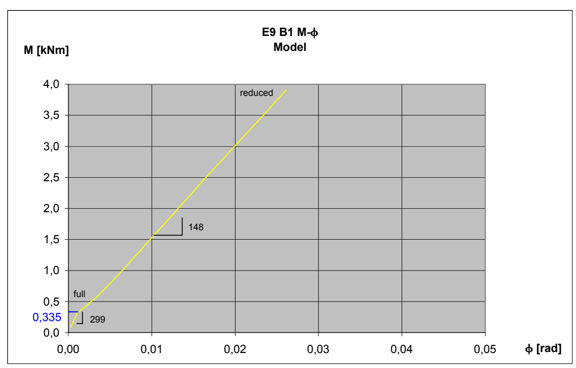

Figure 4.48 M-ϕ specimen E9 side B1 model

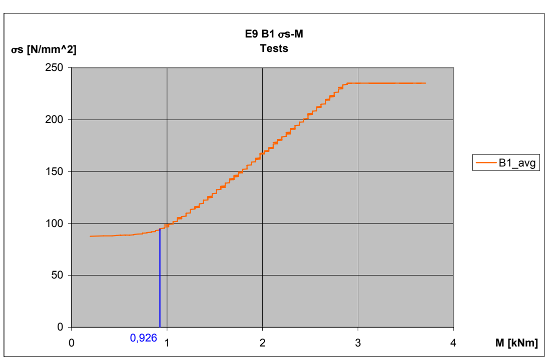

Figure 4.49 σ_s-M specimen E9 side B1 test

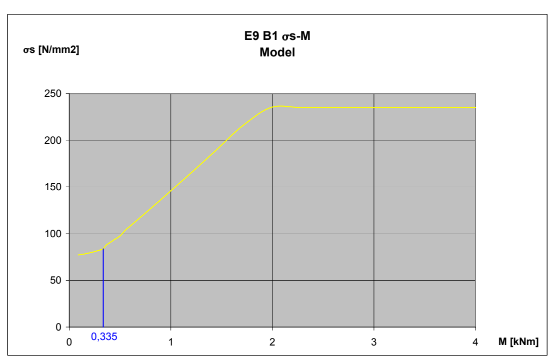

Figure 4.50 σ_s-M specimen E9 side B1 model

To see if dowels have any influence on the stiffness or friction capacity of the connection, side B2 is fitted with three dowels through the end plate. At first sight, no big influence can be detected. Here, the decrease in stiffness occurs at the same level of bending moment as with the specimen with no dowels inserted.

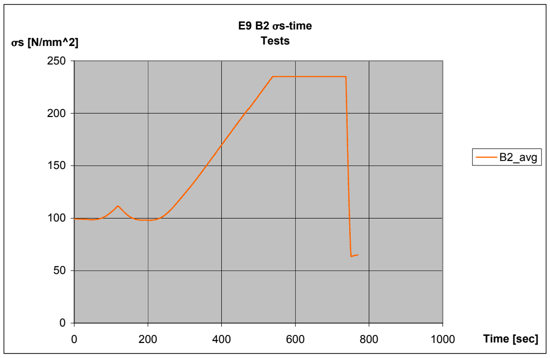

Figure 4.51 σ_t-time specimen E9 side B2

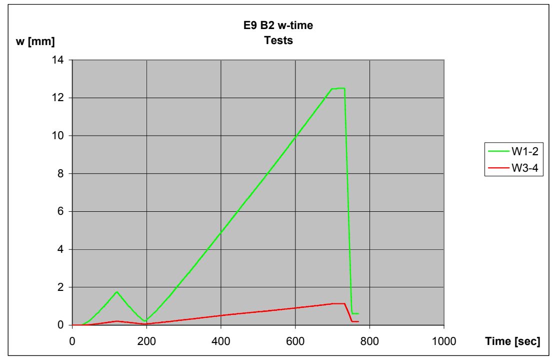

Figure 4.52 w-time specimen E9 side B2

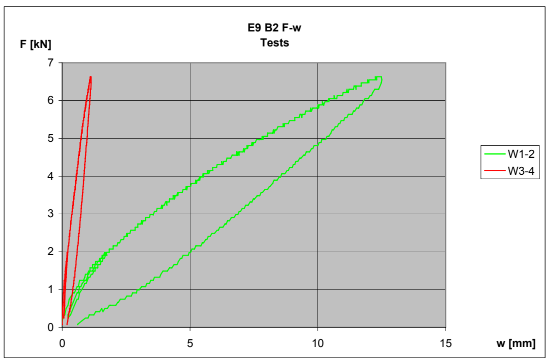

Figure 4.53 F-w specimen E9 side B2 test

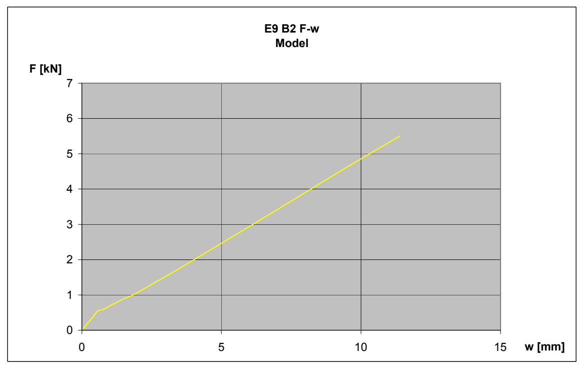

Figure 4.54 F-w specimen E9 side B2 model

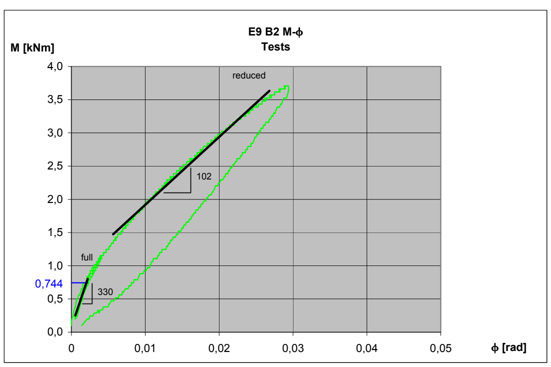

Figure 4.55 M-ϕ specimen E9 side B2 test

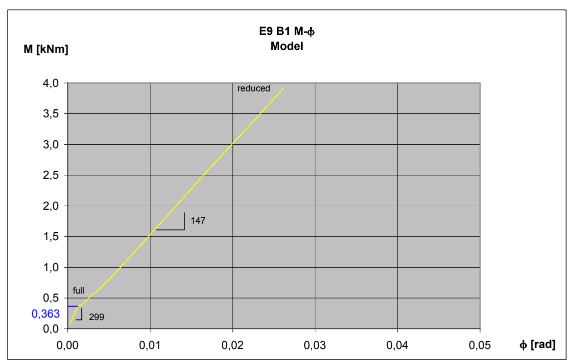

Figure 4.56 M-ϕ specimen E9 side B2 model

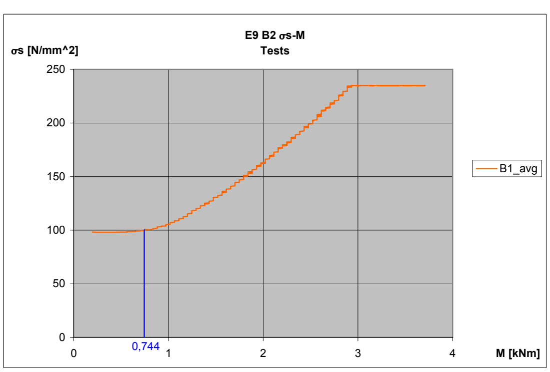

Figure 4.57 σ_s-M specimen E9 side B2 test

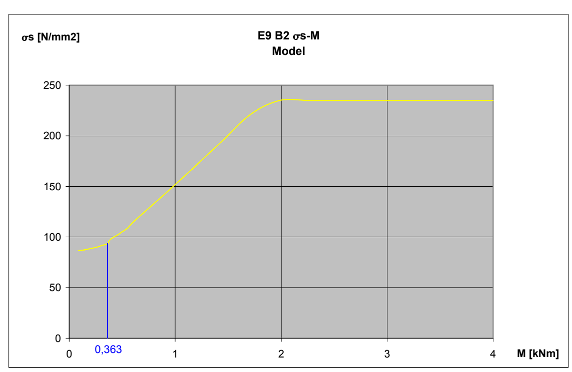

Figure 4.58 σ_s-M specimen E9 side B2 model

A selection of the recorded data, together with some characteristics of the tested specimen is presented in table 4.3.

Table 4.3 results connection tests

		Tests			Model					
		C full [kNm/rad]	C reduced [kNm/rad]	M [kNm]	C full [kNm/rad]	C reduced [kNm/rad]	M [kNm]	Fpw [kN]	MOR [N/mm²]	density [kg/m³]
E1	**B1**	180	70	0,240	226	111	0,067	4,7	37,36	550
	B2	56	66	0,194	226	111	0,067	4,3		
E9	**B1**	312	100	0,926	299	148	0,335	18,8	64,41	684
	B2	330	102	0,744	299	147	0,363	21,2		
E11	**B1**	340	84	0,512	258	127	0,249	13,9	43,72	638
	B2	414	101	0,558	258	127	0,304	16,6		
E14	**B1**	180	68	0,320	251	124	0,073	4,5	31,58	523
	B2	302	93	0,502	251	124	0,266	15,0		
E18	**B1**	333	84	0,459	268	132	0,269	14,7	54,42	555
	B2	375	76	0,733	268	132	0,269	15,3		

In the table, the C-values are presented for the test results and for the model. Also, the moment at which the timber face gets disconnected, which is the transition from the full to the reduced cross section, is given. In the last three columns, the working prestress force after tightening (F_{pw}), the modulus of rupture (MOR) and the density of the specimen are given.

This table shows a generally higher C-value for the reduced section from the model than from the tests. But the moment at which this reduced section occurs is generally lowel from the model than from the tests. The C full values are lower from the model. For low prestress values, this value is hard to determine from the tests results, as the number of data points before this occurs is limited.
Generally, the model does predict higher moment values at higher prestress values, which also occurs in the tests.

In all tests and model calculations, yielding of the steel rod occurs at 2 kNm for the model and at 3 kNm for the tests. This corresponds with the assumption that was made at the beginning of this chapter that the level of prestress does not have any influence on the capacity of the connection, but only on the level at which the timber face gets disconnected.
Also, in all tests and model calculations, the steel yields before failure of the timber under compression. From this is can be concluded, that the moment capacity of the connection can be improved by increasing the steel dimensions and/or strength. In figure 4.59, the results of a calculation for side B1 of specimen E9 with a steel yield strength of 360 N/mm² are given.

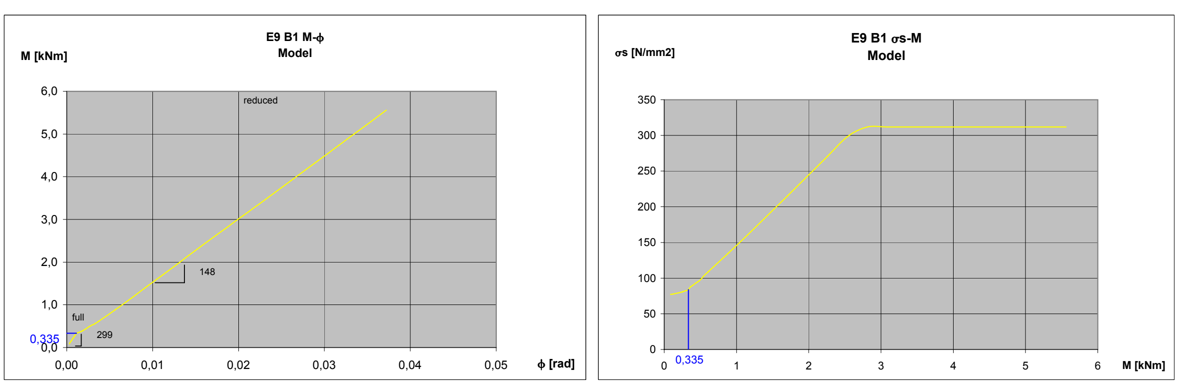

Figure 4.59 calculation E9 B1, S360

These graphs show no variations in M-ϕ relations. Only the steel yields at a higher bending moment of 2,5 kNm instead of 2kNm for the original calculation. With this steel strength, the timber fails under compression before yielding of the steel (table 4.4).

Fable 4.4 calculation results E9 B1, S360

F [kN]	M [kNm]	ϕ [rad]	σt [N/mm²]	σcod [N/mm²]
1	0,610	0,004	108,948	6,278
2	1,160	0,008	161,186	11,542
3	1,710	0,011	215,547	16,672
4	2,260	0,015	270,658	21,789
5	2,810	0,019	311,735	26,631
6	3,360	0,022	311,735	30,593
7	3,910	0,026	311,735	34,455
8	4,460	0,030	311,735	38,265
8,5	4,735	0,032	311,735	40,161

Also it can be seen, that the steel stress does not reach its yielding stress. At a certain point, the steel stress stays constant. Because the modulus of elasticity of timber is much lower than that for steel, the deformation of the timber under compression gets higher than that for steel after a certain stress value. This causes the timber to compress rather than the steel to extend. Although one would expect that when this happens, the C value for the connection would decrease again, this does not show in the M-ϕ graph (figure 4.59)

Because increasing the steel dimensions decreases the timber surface area, this can only be done when this does not result in failure of the timber under normal compression or tension forces.

Figure 4.60 shows the part of the timber face of specimen E9 (the indication E19 on the picture is wrong) that was under compression after the test was done. No compression failure mechanisms can be found, even under close inspection. The compression line can only be found by touch: the compressed section (left of the line) is flattened more and feels softer than the disconnected section.

figure 4.60 compression zone specimen E9 B1

A minimum value for the coefficient of friction (μ) between the timber and steel at the steel and plate can be found by evaluating the load curve of side B1 of specimen E1. This side showed the lowest steel stress values and thus friction force values and did not fail by shear force capacity. The maximum value for μ is found at a steel stress of 87,7 N/mm², which corresponds with a friction force of 18,7 kN, under a point load of 4,9 kN. The value for μ at this combination is 4,9/18,7 = 0,26. Probably the actual value is much higher, but this can only be determined when a connection fails at this mechanism.

4.3 Conclusion

To determine the moment capacity of the shear block joint connection that was originally designed for the viewing platform for the CONIFERS-project, a failure model was developed and checked with tests done on 5 specimen with 2 connections each.

From the relaxation curve of a pretensioned connection it was shown that 65% to 75% of the original prestress would have disappeared due to relaxation of the timber after three weeks. This prestress level prescribes the initial stiffness of the connection before the timber face gets disconnected from the steel end plate under bending.

All the connections that were tested showed failure by yielding of the steel tension rod. This occured at 3 kNm in the tests and at 2 kNm in the failure model. This capacity can be increased by using higher strength steel or increased steel dimensions. When this is done however, the timber section area decreases, reducing the timber strength capacity under normal compression and/or tension forces.

New calculations with an increased steel yield strength from 235 to 360 N/mm^2 showed an increase in bending moment capacity from 2,0 to 2,5 kNm. At this moment, the connection fails by compression stress failure of the timber at the steel end plate.

The failure model calculations showed some unexpected (or wrong) values for stiffness of the connection after yielding of the steel tension rod. Since time is limited for this project, this needs to be anaysed further when this model is used for predicting the moment capacity of the shear block joint connection in future projects.

For the applied combination of moment and shear force, the connection proved not to be sensitive for shear force failure at the contact area of the timber face with the steel end plate, even with low prestress values. When the connection is loaded in bending, the steel stress in the tension rod increases, which also increases the shear force capacity. A minimum value for the coefficient of friction was found at $\mu = 0,26$

5 Conclusions and Recommendations

For this project, three topics have been analysed:

- Are the results from the CONIFERS project concerning strength of larch round wood representative for all the larch forests in The Netherlands?
- What are the consequences of the timber strength variations for the round wood viewing platform?
- What is the moment capacity of the round wood connection developed for this viewing platform?

The results and some recommendations for each topic are presented below.

Quality Investigation

Conclusions

The GIS analysis showed a certain relationship between the values for the Site index of a plot and the density of the trees from this plot.

Together with knot size or knot ratio, the density can be used as a grading parameter for strength class C40 and C24. In general, the density has a positive correlation with the strength of homegrown larch.

Because the trees used in the CONIFERS project are from an area with a very high S-value, it can be presumed that the result from this project are not representative for all the larch forests in The Netherlands.

It was shown that some specimen from the Smilde series which complied with the selection criterion set in the CONIFERS project, had much lower stiffness values than predicted by this criterion. This implies that some of the columns used in the viewing platform are of much lower stiffness than designed with.

Recommendations

The relations between strength and stiffness parameters of round wood appear to be slightly different from the relations known and set by EN338 for sawn timber. More study on this subject could lead to a separate classification system for round wood and improve the use of round wood in constructions.

The relationship between the S-value and the density is hopeful. When the relation can be set after more information has come available, a tool can be made that predicts the strength of homegrown larch by specification of its location of origin and minimum knot size or knot ratio.

Viewing Platform

Conclusions

It was shown that the influence of the connection element is much larger than the stiffness and strength of the columns.

Only when one element is missing due to failure caused by the lower stiffness, some fundamental changes occur, but in the model this does not lead to dangerous situation.

When all elements are weaker than expected, some increase in deformation and decrease in eigenfrequency is found. Again, in the model this does not lead to dangerous situations.

Recommendations
Because the used model is a simplification of the real situation, the occurence of failure of one element and low stiffness for all elements should be analysed in a more detailed model.

Connection

Conclusions
From the relaxation curve of a pretensioned connection it was shown that 65% to 75% of the original prestress would have disappeared due to relaxation of the timber after three weeks. This prestress level prescribes the initial stiffness of the connection before the timber face gets disconnected from the steel end plate under bending.

All the connections that were tested showed failure by yielding of the steel tension rod. This occured at 3 kNm in the tests and at 2 kNm in the failure model.

The capacity can be increased by using higher strength steel or increased steel dimensions. When this is done however, the timber section area decreases, reducing the timber strength capacity under normal compression and/or tension forces.

For the applied combination of moment and shear force, the connection proved not to be sensitive for shear force failure at the contact area of the timber face with the steel end plate, even with low prestress values. A minimum value for the coefficient of friction was found at $\mu = 0,26$

Recommendations
The failure model calculations showed some unexpected (or wrong) values for stiffness of the connection after yielding of the steel tension rod. This needs to be anaysed further when this model is used for predicting the moment capacity of the shear block joint connection in future projects.

6 Appendices

A1 List Of Terms

An explanation on different soil types can be found in the "Bodemkaart van Nederland" (in Dutch), STIBOKA

crown projection	= That part of a plot, in percentage of the total area, that is covered by the projection of bushes and shrubs.
dominant height	= The average height of the thickest tree per are
kaalkap (Dutch)	= Complete removal of a forest
leegkapbos (Dutch)	= Standing forest, at which renewal is done by "kaalkap". The area of "kaalkap"is at least 20 are. The plots are mostly more or less of uniform age and consist of 1 tree species.
opperhoogte (Dutch)	= The average height of the highest tree per are
plot	= Section of a forest
Site-index, S value	= The height of a tree with an infinite age
standing forest	= Forest with a crown projection of 60% or more.
thinning	= Removal of part of the forest to stimulate growth
topwood	= Wood from the top part of a tree

A2 Literature

Blass, H.J...[et al.] 1995 Timber engineering; STEP 1 : Basis of design, material properties, structural components and joints, Almere : Centrum Hout.

De Vries, P.A. 2000a Zicht op dunningshout, deel 'Uitzicht' (in Dutch). Master Theses, Delft.

2000b Zich op dunningshout, deel 'Inzicht' (in Dutch). Master Theses, Delft.

Ranto-Maunus,A. 1999 Round small-diameter timber for construction, Final report of projec FAIR CT 95-0091, Technical Research Center Of Finland, Espoo.

Van den Burg, J. 1997 Groei en groeiplaats van Japanse lariks, Abies grandis en Tsuga heterophylla in Nederland (in Dutch). Report 'Instituut voor Bos- en Natuuronderzoek', Wageningen.

Anonymous 1966 Bodemkaart van Nederland (in Dutch), Stichting voor Bodemkartering.

1984 Vierde Nederlandse Bosstatistiek Deel 1: De Oppervlakte Bos 1980-1983 (in Dutch).

1996 Opbrengst Tabellen voot belangrijke boomsoorten in Nederland (OPTAB, in Dutch).

1997a NEN-EN 1310, Rondhout en gezaagd hout- Methode voor het meten van onvolkomendheden, Nederlands Normalisatie Instituut (in Dutch).

1997b NS-INSTA 142, Nordic visual strength grading rules for timber, Norges Standardiseringsforbund (NSF).

1999 NEN 5461\5466, Kwaliteitseisen voor hout (KVH 2000) - Gezaagd hout en rondhout - Algemeen gedeelte\Houtsoorten Europees vuren, Europees grenen en Europees lariks, Nederlands Normalisatie Instituut (in Dutch).

2003a DIN 4074-1, Sortierung von Holz nach der Tragfahigkeit, Teil 1: Nadelschnittholz, Deutsches Institut fur Normung (in German).

2003b EN 14251, Structural round timber - Test methods, European Committee for Standardisation (CEN).

2003c EN 408, Timber Structures - Structural timber and glued laminated timber - Determination of some physical and mechanical properties, European Committee for Standardisation (CEN).

2004 EN 384, Structural timber - Determination of characteristic values of mechanical properties and density, European Committee for Standardisation (CEN)

2005 Digital Soilmap East-Netherlands, copyright 2005 Alterra, obtained from "Kaartenkamer", faculty of Architecture, Technical University of Delft.